Dissertation in Astronomy

submitted to the

Combined Faculties of the Natural Sciences and Mathematics

of the Ruperto-Carola-University of Heidelberg, Germany

for the degree of

Doctor of Natural Sciences

put forward by

Anahí Caldú Primo, M.Sc.

born in Mexico City, Mexico

Oral examination: July 10, 2015

Molecular Gas Velocity Dispersions
in Nearby Galaxies

Anahí Caldú Primo
Max-Planck-Institut für Astronomie

Referees: **Prof. Dr. Henrik Beuther**
Prof. Dr. Hans – Walter Rix

Abstract

Despite the fact that molecular gas in galaxies is the most essential ingredient for the star formation process, its thorough characterization has not yet been accomplished. A common assumption is that molecular gas emission (mostly traced by CO) arises from molecular clouds with observed velocity dispersions of $2-5\,\mathrm{km\ s^{-1}}$. In this thesis, I present the results obtained from investigating the velocity dispersions measured in the molecular gas disks of nearby galaxies. On 0.5 kpc scales (the average spatial resolution), the measured CO velocity dispersions have a mean value of $\sim 12\,\mathrm{km\ s^{-1}}$ (1σ dispersion of $3.9\,\mathrm{km\ s^{-1}}$). These values are higher than previously expected, and are comparable to those measured for neutral atomic gas. To investigate the origin of these large dispersions, a comparison between interferometric and single-dish line width measurements for NGC 4736 and NGC 5055 (at ~ 0.5 kpc resolution) and for the neighboring Andromeda galaxy, M 31, (at ~ 100 pc resolution) is presented. Despite the different scales studied, the single-dish line widths are ~50% greater than the corresponding interferometric ones. Additionally, the interferometer recovers only a fraction ($50-90\%$) of the flux that is measured by the single-dish. After stacking the high-sensitivity M 31 data, an analysis of the resulting spectral profiles from the two distinct instruments is performed in detail. The results are that single-dish spectra are better described by two components, one narrow ($\mathrm{FWHM_N} \sim 7.5 \pm 0.4\,\mathrm{km\ s^{-1}}$) and one broad ($\mathrm{FWHM_B} \sim 14.4 \pm 1.5\,\mathrm{km\ s^{-1}}$); while for the interferometric data, one component suffices ($\mathrm{FWHM} \sim 7.1 \pm 0.4\,\mathrm{km\ s^{-1}}$). The overall implication is that molecular gas is present in two distinct phases: one that is clumpy and organized as molecular clouds, and another one that is more diffuse and has larger velocity dispersions.

Zusammenfassung

Obwohl molekulares Gas in Galaxien die wichtigste Zutat im Sternentstehungsprozess darstellt, ist dessen vollständige Charakterisierung bislang noch nicht gelungen. Üblicherweise geht man davon aus, dass die Emission molekularen Gases (gemessen durch CO als Indikator) von molekularen Wolken ausgeht, welche Geschwindigkeitsdispersionen zwischen $2-5\,\mathrm{km\,s^{-1}}$aufweisen. In dieser Dissertation präsentiere ich Ergebnisse, die aus der Analyse von gemessenen Geschwindigkeitsdispersionen der molekularen Gasscheiben in benachbarten Galaxien hervorgehen. Auf Skalen von 0.5 kpc (durchschnittliche räumliche Auflösung) hat die mittlere Geschwindigkeitsdispersion von CO einen Wert von $\sim 12\,\mathrm{km\,s^{-1}}$ (1σ Streuung von $3.9\,\mathrm{km\,s^{-1}}$). Dieser Wert ist größer als bislang angenommen und vergleichbar mit dem von neutralem, atomarem Gas. Um den Ursprung dieser großen Geschwindigkeitsdispersion zu erkunden, werden Messungen der interferometrischen und der single-dish Linienbreite für NGC 4736 und NGC 5055 (bei einer Auflösung von $\sim 0.5\,\mathrm{kpc}$), sowie der benachbarten Andromedagalaxie, M 31, (Auflösung $\sim 100\,\mathrm{pc}$) verglichen. Trotz der unterschiedlichen räumlichen Skalen sind die single-dish Linienbreiten ~50% größer als die entsprechenden interferometrischen. Zusätzlich sammelt der Interferometer nur $50-90\%$ der Flussdichte, die der single-dish misst. Nach dem Stacking der hochempfindlichen M 31 Daten wird eine detaillierte Analyse der resultierenden Spektralprofile für die beiden unterschiedlichen Instrumente durchgeführt. Zusammenfassend ist festzustellen, dass die single-dish Spektren optimal durch zwei Komponenten beschrieben werden können: eine schmale ($\mathrm{FWHM_N} \sim 7.5 \pm 0.4\,\mathrm{km\,s^{-1}}$) und eine breite ($\mathrm{FWHM_B} \sim 14.4 \pm 1.5\,\mathrm{km\,s^{-1}}$). Für interferometrische Daten hingegegen genügt eine Komponente ($\mathrm{FWHM} \sim 7.1 \pm 0.4\,\mathrm{km\,s^{-1}}$). Die allgemeine Schlussfolgerung dieser Ergebnisse ist, dass molekulares Gas zwei unterschiedliche Phasen hat: eine klumpige, sich als Molekularwolken anordnende und eine, die eher diffus ist und größerere Geschwindigkeitsdispersionen aufweist.

"La utopía está en el horizonte.
Camino dos pasos, ella se aleja dos pasos.
Camino diez pasos, y el horizonte se corre diez pasos más allá.
Por mucho que camine, nunca la alcanzaré.
¿Entonces para que sirve la utopía?
Para eso, sirve para caminar."

F. Birri/E. Galeano

Para los caminantes

Contents

CHAPTER 1

INTRODUCTION

Molecular gas constitutes the building block of star formation. In spite of playing such an important role in one of the key processes taking place in the Universe, many questions around it still remain open. It was not until the 60's that radio observations of interstellar molecules started taking place. Since then, constant improvements in instrumentation have enabled us to probe this elusive interstellar medium phase in greater detail. Gaining insight into the physical properties of molecular gas translates to achieving a better understanding of star formation. Star formation is, in turn, a pivotal process in galaxy evolution models. Therefore, an appropriate description of the present day Universe necessarily requires a complete characterization of molecular gas. The aim of this thesis is to observationally study the velocity dispersions of molecular gas in nearby galaxies. The results presented here provide evidence of higher structural complexity of molecular gas, as compared to what has been typically accounted for.

1.1 Multiphase Interstellar Medium

The space between stars is sparsely populated, but not devoid of baryonic matter. It is filled with gas and dust at lower densities than what can be created artificially on Earth[1]. The interstellar medium (ISM) is tenuous material that exists in a number of different phases, which result from complex radiative, thermal, and kinematic processes. Material and energy flow between the ISM phases in complex patterns, making their modeling to remain a theoretical challenge. Given the complexity of the ISM, there are several schemes aimed to describe its constituent phases. I will focus on the classification scheme introduced by Mihalas & Binney (1981), who divide the ISM in five distinct phases: hot and warm ionized phases, warm and cold neutral atomic phases, and a molecular phase. These phases have characteristic temperatures, densities, and ionization fractions which are set through the balance between heating and cooling mechanisms. In the following sections I will give a brief description of the different components of the ISM: dust and the five gaseous phases, putting particular emphasis on molecular gas.

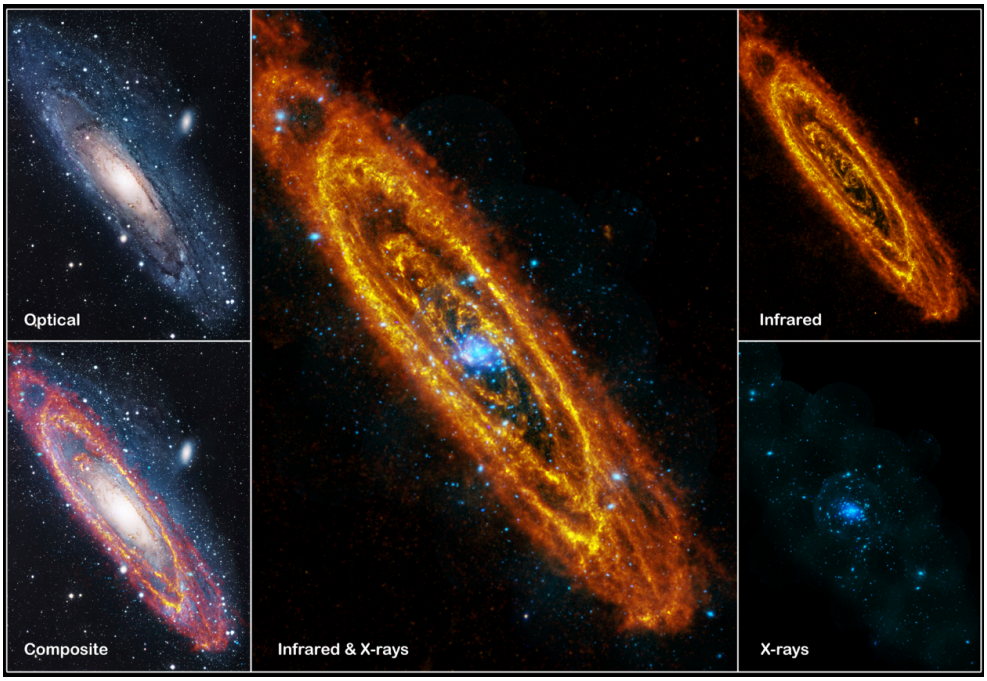

Figure 1.1 **Multiphase Interstellar Medium** This figure, taken from the European Space Agency (ESA) webpage, shows multi-wavelength observations of Andromeda. Different wavelengths trace different components of the galaxy. The individual images are, infrared: ESA/Herschel/PACS/SPIRE/J. Fritz, U. Gent; X-ray: ESA/XMM-Newton/EPIC/W. Pietsch, MPE; optical: R. Gendler.

[1]The highest vacuums achieved in the laboratory are of the order of a few hundred particles per cm^3.

1.1.1 Neutral Atomic Gas

Neutral atomic gas (H I) is usually the most radially extended component of the ISM in galaxies. Observations of H I are possible through the hyperfine 21 cm (1420 MHz) line transition of the atom's ground state. This transition originates when the electron's spin flips from being parallel to being antiparallel with respect to the nuclear spin. The discovery of this emission line in the middle of the past century was a breakthrough in Astronomy, as it provided us with an invaluable method of probing the structure and dynamics of galaxies (including the Milky Way).

H I heating is dominated by UV starlight, which produces photoelectric emission from dust grains (Watson 1972), and by cosmic rays. Line emission of forbidden lines (e.g. [CII] 158 μm and [OI] 63 μm) dominates the cooling (Wolfire et al. 2003). Theory predicts that by balancing the heating and cooling processes of H I in presence of thermal pressure equilibrium, two stable phases result: a clumpy cold neutral medium (CNM) embedded in a more diffuse warm neutral medium (WNM) (Field et al. 1969; Wolfire et al. 1995, 2003). These two phases coexist only for a narrow range of pressures. As an example, Fig. 1.2 taken from Draine (2011, Figure 30.2 (b)) shows the solutions for temperature and pressure resulting from the balance of heating and cooling processes. This simple two-phase picture appears to be insufficient when considering non-thermal pressure contributions (e.g. magnetic fields, turbulence). In fact, observations in the Solar Neighborhood suggest that 48% of the WNM might be in the thermally unstable regime ($500 < T < 5\,000$ K, Heiles & Troland 2003).

WNM is easily detected in emission, making it an excellent probe of neutral gas in galaxies. It has temperatures below 10^4 K and densities that range between $n \sim 0.1 - 0.3\,\mathrm{cm}^{-3}$. Its volume filling factor[2] is $\sim 60\%$ (Heiles & Troland 2003). *CNM* is not easily observed in emission, as the emission lines are dominated by WNM. Therefore, it is predominantly observed in absorption against background continuum radio sources (e.g. bremsstrahlung radiation in H II regions, Heiles & Troland 2003) or in self-absorption against bright background H I emission (Braun et al. 2009). Observational constraints place this phase at characteristic temperatures of $T \gtrsim 300$ K and at densities of $n \sim 20\,\mathrm{cm}^{-3}$. It is suggested that this phase is distributed in rather dense filaments or sheets, and is associated with molecular gas. It has a volume filling factor of only $\sim 2 - 4\%$ of the total volume of the ISM (Tielens 2005).

[2] Volume filling factors are very controversial, so I include them just for illustrative purposes.

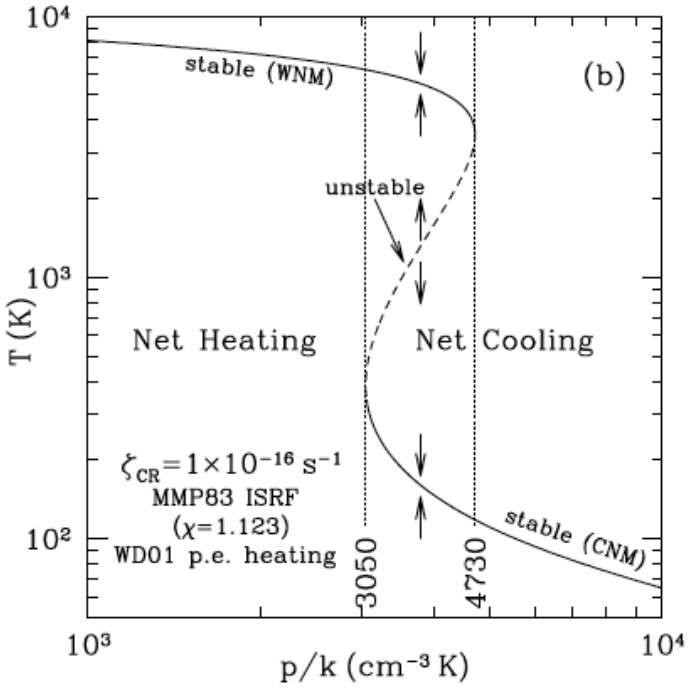

Figure 1.2 **Two-phase model for neutral atomic medium.** This figure, taken from Draine (2011, Figure 30.2 (b)), shows the steady state temperature T as a function of thermal pressure p. There are three distinct regions for $3200 \lesssim p/k \lesssim 4400\,\mathrm{cm^{-3}\,K}$: a high temperature warm neutral medium (WNM) solution, a low temperature cold neutral medium (CNM) solution, and an intermediate temperature equilibrium that is thermally unstable.

1.1.2 Molecular Gas

Molecular gas (H_2) is the principal component by mass of the ISM in the central regions of most spiral galaxies (Young & Scoville 1991). Efficient H_2 formation happens in dense regions where UV radiation cannot penetrate. It is facilitated by the presence of dust grains, which act both as a shield against UV photons, and as catalysts for the reactions that create the H_2 molecule. H_2 regions have very low temperatures, as molecules enable effective ways of cooling due to the number of rotational energetic levels available. At low densities cooling is dominated by the CO molecule, whereas in denser or warmer regions other molecules , like O_2 or H_2O, take over. Cosmic rays are the dominant heat source for molecular gas; other heat sources like UV radiation and free electrons (at least inside molecular clouds), are negligible.

Observing molecular gas is not as easy as observing neutral atomic gas. Even though H_2 is the most abundant molecule in the ISM, direct observations of it are difficult. Its electronic transitions lie in the ultraviolet, and have been observed in absorption against nearby early type

stars (Spitzer et al. 1974; Rachford et al. 2002). However, the need for background sources limits the number of sight lines where H_2 can be detected, thus UV observations are not ideal for studying bulk molecular gas. The rotational and vibrational transitions of the ground state of this low mass, symmetric molecule are quadrupolar, making them relatively faint. Being low energy transitions, they lie on the infrared part of the spectrum and can be observed by means of ground-based and air borne facilities. Particularly, the lowest vibrational H_2 transition at $2\,\mu$m has been observed towards Galactic shocks and photodissociation regions (Shull & Beckwith 1982). These infrared transitions can only be observed in warm environments, where they get excited to temperatures $T \gtrsim 100$ K. The bulk of H_2 is cold, though, remaining invisible.

In order to probe cold molecular gas, other tracers are necessarily needed. The most widely used is ^{12}CO, as it is the second most abundant molecule in the Universe ($\sim 10^{-4}$ with respect to H_2). This molecule has a ground rotational transition with an energy $h\nu_{10}$ of 5.5 K and a thermalization critical density $n_{crit} = 5{\times}10^2\,\mathrm{cm}^{-3}$, so it is easily excited in cold environments. Low energy ^{12}CO transitions, however, become optically thick very fast, and consequently are not very useful to quantify column densities in dense environments. In the local ISM, this line becomes heavily saturated. Other less abundant, optically thin isotopes are preferred; for example, ^{13}CO with relative abundance $^{12}\mathrm{CO}/^{13}\mathrm{CO} \approx 69$ at the solar vicinity (Bolatto et al. 2013), and $C^{18}O$, approximately five times less abundant than ^{13}CO (Kruegel 2003). To study even denser environments, like clumps or cores (see Sec. 1.2), other molecular species, like CS or HCN, are used. The critical densities for the lowest transitions of these molecules are $4.6\times10^4\,\mathrm{cm}^{-3}$ and $2.6\times10^6\,\mathrm{cm}^{-3}$, respectively. Sensitivity limits extragalactic studies almost exclusively to ^{12}CO. Since my thesis uses solely ^{12}CO observations, from now on I will simply refer to it as CO.

As H_2 cannot be detected directly, a "CO-to-H_2" conversion factor (X_{CO}) is required to extrapolate observed integrated CO intensities (I_{CO}) to the actual H_2 column densities (N_{H_2}):

$$N_{H_2} = X_{\mathrm{CO}} I_{\mathrm{CO}} \tag{1.1}$$

A characteristic value of $X_{\mathrm{CO}} = 2 \times 10^{20}\,\mathrm{cm}^{-2}\,(\mathrm{K\,km\,s}^{-1})^{-1}$ was established for the local Galactic environment in different observational studies (e.g. Solomon et al. 1987; Strong & Mattox 1996). In principle, X_{CO} is the sum of a number of factors including metallicity, excitation, and cloud structure on large areas. Nevertheless, both in the Galactic disk and in the disks of "normal galaxies" with metallicities similar to solar, the values obtained for X_{CO} agree with the canonical value within a factor of two (Bolatto et al. 2013).

In more "extreme" environments, observations have shown that X_{CO} departs from this value. For example, in low metallicity regions ($Z < 0.5\,Z_\odot$, Bolatto et al. 2013), X_{CO} is higher. In these regions, dust abundance, which is important for CO shielding, is also low. The resulting decrease of CO shielding pushes the CO-emitting region further inside the H_2 cloud. In this way, even

though the total amount of H_2 is unchanged (as it self-shields), lower intensities of CO are observed, and the conversion factor consequently increases. Recent observational studies have found larger X_{CO} factors in metal poor environments: SMC (Mizuno et al. 2001), LMC (Fukui et al. 2008), and Local Group Galaxies[3] (Leroy et al. 2011).

Another case of departure from the Galactic value has been observed in the centers of some spiral galaxies (including the Milky Way) and in starburst galaxies (especially in ultra-luminous infrared galaxies, or ULIRGs). In these environments, molecular gas has particular characteristics: 1) Gas is mostly molecular and a significant fraction of CO emission will originate from a warm extended phase, 2) temperatures are higher, implying higher CO emission for the same amount of H_2, and 3) velocity dispersions are larger either due to merger activity or to the stellar gravitational potential. The combination of these factors give rise to lower X_{CO} factors in these environments (Downes & Solomon 1998; Sandstrom et al. 2013). Determining X_{CO} is far from being a closed topic and a lot of effort is being put into understanding it. Getting a good handle on H_2 mass estimates is of great importance, since it is an essential ingredient for star formation, even in environments where large amounts of atomic gas are available (Schruba et al. 2011).

1.1.3 Ionized Gas

Ionized gas comprises the highest temperature component of the ISM ($T \sim 10^4 - 10^7$ K). In the Milky Way, the ionized phase accounts for $\sim 23\%$ of the gas mass and fills most of its volume (Draine 2011). Within the ionized gas, two distinct components may be defined.

The *hot ionized medium* (HIM) is shock-heated by fast stellar winds and blast waves from supernovae explosions. It has characteristic temperatures of $T \sim 10^6$ K, and is very diffuse, with $n \sim 10^{-3}$ cm^{-3} (Tielens 2005). It is mostly observable through highly ionized species resulting from collisional ionization (e.g. OVI, NV, and CIV), which are detected in absorption towards bright UV continuum sources (usually hot stars). In the Milky Way it might fill $\sim 50\%$ of the total volume, but makes up only $\sim 1\%$ of its mass (Tielens 2005).

The *warm ionized medium* (WIM) is observed through optical and UV ionic absorption lines against background sources, or through recombination lines in emission, in particular the hydrogen's Balmer lines. It has temperatures of $T \sim 10^4$ K (characteristic of photo-ionized regions) and densities $n \sim 0.3$ cm^{-3}. Heating is dominated by photoionization of hydrogen. The importance of different cooling mechanisms present in ionized gas changes as a function of temperature. At low temperatures ($T < 15\,000$ K), the dominant process is metal-line collisional cooling. At temperatures between 20 000 and 40 000 K collisional excitation followed by line emission gains

[3] In this study the SMC and LMC are included as well

importance. At the highest temperatures, above $10^6 - 10^7$ K, bremsstrahlung dominates the cooling. WIM's local volume filling factor is $\sim 25\%$ (Tielens 2005). Although it is mainly associated with H II regions, observations have shown that a considerable fraction of the ISM and extra-planar gas is filled with "diffuse ionized gas" (Reynolds 1984).

1.1.4 Dust

In the Milky Way, 1% of the ISM's mass is in solid form (silicates and carbonaceous material), known as dust (Draine 2003). This number might appear insignificant; however, dust has a big impact on the appearance of galaxies. Dust absorbs $\sim 50\%$ of the starlight in the Universe, reprocesses it, and reemits it at longer wavelengths (Kennicutt & Evans 2012). Starlight emission reprocessed by dust is responsible for most of the spectral energy distribution of the ISM at wavelengths longer than 912 Å. Apart from reprocessing starlight emission, dust grain surfaces are a key ingredient for the formation of molecules, as they facilitate atom encounters, and catalyze their reactions (as is the case for H_2).

Observations show dust forms as metal-enriched stellar ejecta cool (e.g., in supernova remnants and asymptotic giant branch stars). However, the bulk of dust formation must happen through other channels (Tielens et al. 1994; Draine 2003), as dust destruction timescales (5×10^8 yr, Seab 1987) are so much shorter than star ejecta timescales (2.5×10^9 yr, Tielens et al. 1994). There is evidence for dust grain growth inside molecular clouds (dust grain sizes range from 0.35 nm to 1 μ, Kennicutt & Evans 2012). Dust destruction happens through collisions with high-velocity ions ($v \geq 50\,\mathrm{km\ s^{-1}}$) in dense environments, a process called sputtering. These conditions are typically met in supernovae shocks.

The physical properties (size and chemical composition) of dust are inferred from extinction curves. Extinction curves are built empirically by comparing obscured and unobscured stellar sources. The different regions in these curves give us information about the different dust components. At short infrared wavelengths, $\lambda \sim 5 - 20\,\mu$m, dust emission is dominated by molecular bands from polycyclic aromatic hydrocarbons (PAHs). At longer infrared wavelengths, thermal continuum emission from the main dust population is predominant. Small grains, which are transiently heated by intense radiation fields (star forming regions), emit out to $\sim 60\,\mu$m. Larger dust grains, emitting at steady-state temperatures, contribute to the emission at longer wavelengths (Draine 2003).

1.2 Molecular Clouds' Structure

Knowing how much H_2 there is is not enough, it is also necessary to know how it is structured. So far, molecular gas has been found predominantly in giant molecular clouds (GMCs), mostly distributed near the mid-plane of the galaxy. In normal star-forming galaxies, $\sim 50\%$ of H_2 (Sawada et al. 2012) is organized in distinct cloud complexes with typical masses $M \sim 10^4 - 10^6\,M_\odot$ and sizes of $\sim 20 - 50$ pc (Blitz 1993). The temperatures inside these clouds are of the order of 10 K and densities of $n \geq 10^2\,cm^{-3}$. Their contribution to the overall galactic volume is very low, with a filling factor $f < 1\%$.

More sensitive observations using dense gas tracers show structures within GMCs, like filaments, clumps, and cores (André et al. 2010). Blitz & Williams (1999) defined three typical molecular gas structures (see Figure 1.3):

Clouds are detected in CO. Their typical masses are $M \gtrsim 10^4\,M_\odot$, with mean densities[4] of $n \sim 50 - 500\,cm^{-3}$. They have linear size scales (L) of a few parsecs, and may contain several sites of star formation.

Clumps are defined as coherent regions observed in emission. Their typical densities are $n \sim 10^3 - 10^4\,cm^{-3}$, with linear size scale $L \sim 1$ pc. They are sites of cluster formation.

Cores are gravitationally bound regions. They have typical densities $n \gtrsim 10^4 - 10^5\,cm^{-3}$, and sizes $L \sim 0.1$ pc. They form single stars or multiple systems.

GMCs are surrounded by photodissociation regions (PDRs), which act as borders between the molecular and ionized gas phases. Within a PDR, different atomic and/or molecular species exist, depending on the level of UV photon penetration. Within a PDR, there is a region where hydrogen is mostly molecular and carbon is in its atomic form. Due to the difficulties in observing these regions, van Dishoeck & Black (1988) described it as dark molecular gas. Quantifying the relative abundance of dark molecular gas is important to determine the total amount of H_2.

1.2.1 Scaling Relations of Molecular Clouds

Molecular clouds are the sites of star formation. Studying their properties should shed some light on the star formation process itself. Since the pioneering work of Larson (1981) on local GMCs, many observational efforts have been devoted to characterizing the physical properties of molecular clouds. Three direct properties can be measured for a particular GMC: size, line

[4] In the three cases (clouds, clumps, and cores), mean densities are taken from (Bergin & Tafalla 2007).

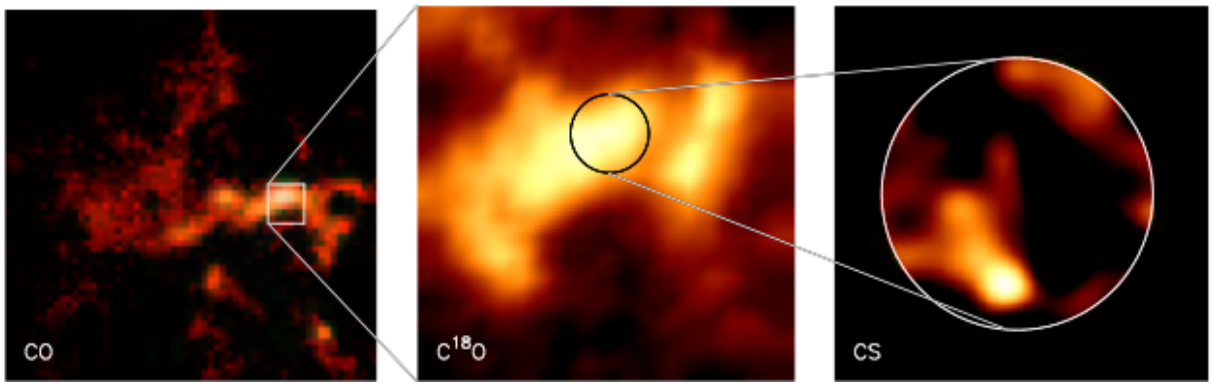

Figure 1.3 **Molecular cloud substructure.** This figure, taken from Blitz & Williams (1999), shows the hierarchical structure present in molecular clouds. On the *left* is the Rosetta molecular cloud as seen through CO emission, which outlines the bulk of the molecular gas cloud. The image in the *center* shows a clump, observed at higher resolution using a dense gas tracer ($C^{18}O$). Finally, on the *right*, using an even higher density tracer (CS), a core pops out. From left to right the observations are from Bell Labs (90″), FCRAO data (50″), and BIMA data (10″).

width, and luminosity. Larson (1981) empirically established the basic scaling relations among these properties, which are commonly known as "Larson's laws".

Size-line width relation: The first scaling law is a power-law relation between the cloud's velocity dispersion (σ) and its size (l) : $\sigma \propto l^{0.38}$. This scaling can be interpreted as a sign of the turbulent nature of the ISM. Larson took the particular exponent's value that he measured, as a signature of Kolmogorov's incompressible turbulence, for which $\sigma \propto l^{1/3}$. More recent observations show that the power-law index might be ~ 0.5 instead (See Fig. 1.4), which is more consistent with compressible supersonic magnetohydrodynamic turbulence (Brunt & Mac Low 2004).

Clouds are in near virial equilibrium: Larson observed a power law relation between the clouds velocity dispersions and their masses. Larson calculated the clouds' virial ratios (the ratio between kinetic and potential energies) using the two empirical power-law relations he measured. He concluded that most of the regions he studied were gravitationally bound and in virial equilibrium (the clouds' gravitational force would be counterbalanced by turbulent support).

Volume density-size relation: A third relation noted by Larson describes an anti-correlation between the cloud's size and its volume density. It is important to note that for clouds in virial equilibrium, only two of the three relations are actually independent. The volume

density-size relation arises as a natural consequence of having clouds in virial equilibrium that follow the size-line width relation. This last relation, assuming virial equilibrium, implies that molecular clouds share a constant mass surface density with value of $\Sigma_{H_2} = 150\,M_\odot\,pc^{-2}$ (Solomon et al. 1987).

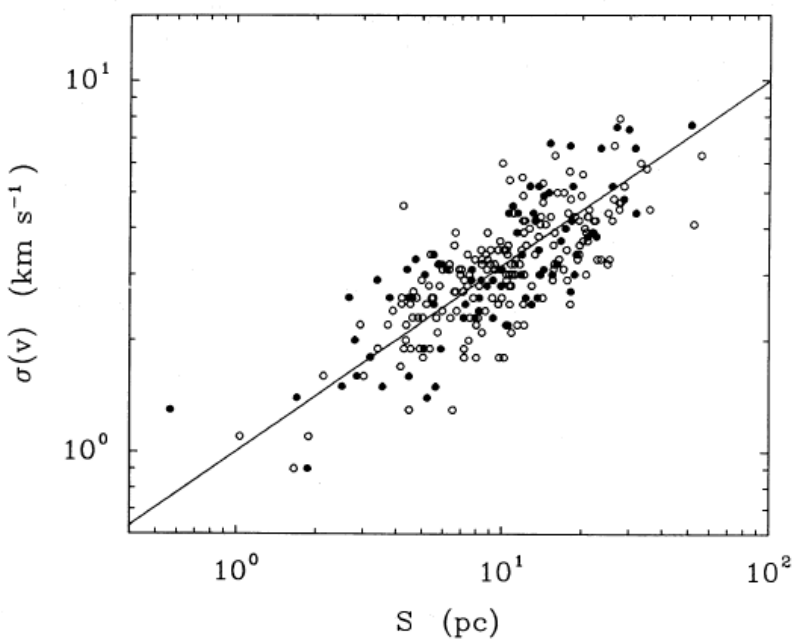

Figure 1.4 **Size-line width relation.** Molecular cloud velocity dispersion σ(v) as function of size (S) measured for 273 clouds in the Milky Way (Figure taken from, Solomon et al. 1987). Black solid circles show clouds with previously known distances. The fitted line is represented by $\sigma(v) = S^{0.5}$ [km s^{-1}].

That was the state of art until recently, when observational capabilities provided enough sensitivity and resolution to study molecular clouds in other Galactic environments and in external galaxies. These studies have shown that, in general, molecular cloud properties depend on environment. For example, Heyer et al. (2009) found that Milky Way GMCs' surface density is not constant when traced with a lower opacity tracer of (^{13}CO). They measure GMCs' surface densities that vary from $\sim 10-200\,M_\odot\,pc^{-2}$. Hughes et al. (2013) made a comparative study of molecular clouds in M 51, M 33, and LMC. They find that GMCs in M 51 are larger, brighter, and have greater line widths than their counterparts in the other two galaxies. Finally, Colombo et al. (2014) compared GMCs in different dynamically motivated regions within M 51, and found that clouds in the spiral arms and in the central regions are brighter and have larger velocity dispersions than comparable clouds in the inter arm regions. On the other hand, Bolatto et al. (2008) carried out a comparative study of the properties of extragalactic GMCs. They conclude that, in general, GMCs in external galaxies with metallicities down to $0.2\,Z_\odot$ follow the same relations

as Galactic GMCs. Hughes et al. (2013) suggest that a main driver in the discrepancies between their and Bolatto et al. (2008) conclusions might be a result of differences in sensitivities and cloud decomposition techniques used on inhomogeneous data sets when analyzing molecular clouds' properties (Fig. 1.5).

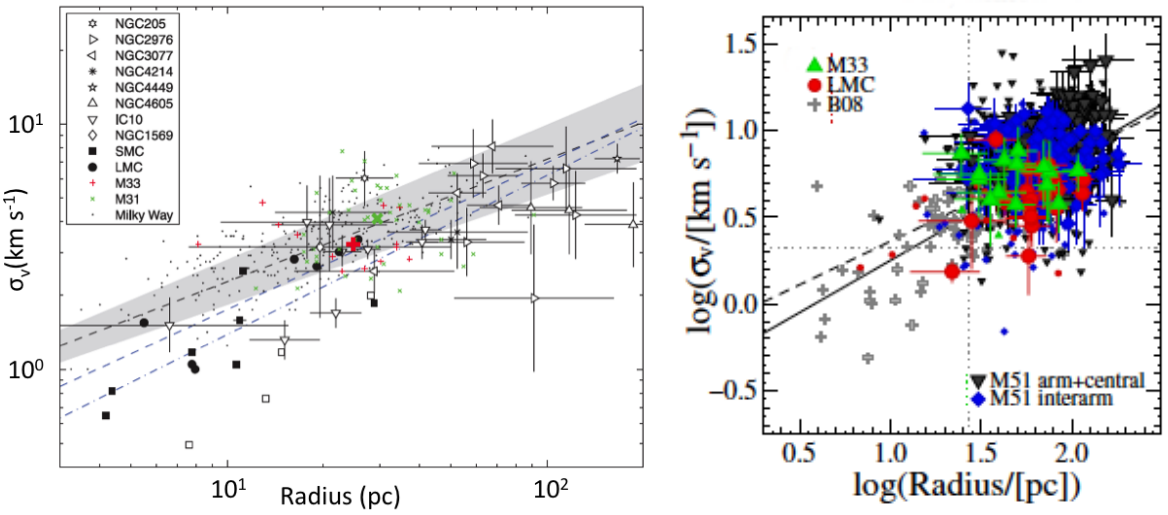

Figure 1.5 **Discrepancy between extragalactic size-line width relation.** *Left*: Plot taken from Bolatto et al. (2008) in which the velocity dispersions of extragalactic GMCs are plotted against their sizes. The black dots are the Milky Way GMCs from Solomon et al. (1987) (same as in Fig. 1.4). The open and filled symbols correspond to measurements based on CO (1 – 0) and CO (2 – 1) observations, respectively. The dashed black line represents the Galactic relation, together with its uncertainty (gray area); while the dashed blue line is a fit to all extragalactic GMCs, and the dashed-dotted one fits for dwarf galaxies only. Even though Bolatto et al. (2008) note that dwarf galaxies slightly deviate from the Galactic relation, their conclusion is that "GMCs identified on the basis of their CO emission are a unique class of object that exhibits a remarkably uniform set of properties from galaxy to galaxy". *Right*: I show a figure from Hughes et al. (2013), where they plot the same size-line width relation for GMCs in M51 (black and blue symbols), M33 (green symbols), and LMC (red symbols), after having placed the three galaxies on the same spatial resolution. As a reference, they over plot Bolatto et al. (2008) measurements with gray crosses. Hughes et al. (2013) conclude that, when studied at matched resolutions, there is no compelling evidence for a size-line width relation among these three galaxies. The correlations observed when looking into inhomogeneous data sets are most likely a consequence of differences in spatial and spectral resolutions among them.

Up to now, mapping molecular clouds in external galaxies has been observationally expensive. However, with new observational capabilities like ALMA (Atacama Large Millimeter/submillimeter Array), larger catalogues of molecular clouds can be consistently assembled. In this way, molecular cloud properties will be better constrained in the near future.

1.3 Star Formation Law

Star formation takes place inside molecular clouds, at scales very difficult to probe outside the Milky Way. Therefore, studying star formation in other galaxies requires a different approach. An important concept, that in principle could link local scales to the extragalactic context, relates the neutral gas content in galaxies to the star formation process itself. It is the so-called star formation law, or Schmidt-Kennicutt law. It is known by this name because first Schmidt (1959) proposed a power-law relation between the total SFR density and the interstellar gas density in the solar neighborhood, and then Kennicutt (1998) presented strong observational evidence supporting this idea for nearby galaxies. This law implies that gas is the main driver of star formation. Even thought Schmidt originally formulated this relation in terms of volumetric SFR and gas densities ($\rho_{\rm SFR}$ and $\rho_{\rm g}$), most of the observations can only measure surface densities. The power-law in terms of SFR and total gas surface densities would then be:

$$\Sigma_{SFR} = A\,\Sigma^{N}_{H_I+H_2} \tag{1.2}$$

Since the formulation of this law, different observational efforts have been carried out to quantify this relation. Kennicutt (1998) observed the first sample large enough to probe a sufficient dynamic range in surface densities that enabled the definition of this relationship empirically. He analyzed the galaxy-averaged values of a large sample of galaxies, which included 61 "normal" galaxies and 36 starburst galaxies. He found a non-linear relation between these two quantities, with an exponent $\mathrm{N} \sim 1.4 \pm 0.1$. This non-linear relation implies that stars form more efficiently in denser environments. In this work, he also noted that at low densities there is often a threshold below which SFRs decline more rapidly.

Many other studies have quantified the spatially-resolved star formation law, to try to understand what the physical processes driving this relation are. The first results came from radially-averaged SFR and gas density profiles measured in samples of galaxies (e.g., Kennicutt 1989; Martin & Kennicutt 2001; Wong & Blitz 2002) and from point-by-point measurements in individual galaxies (Kuno et al. 1995; Zhang et al. 2001; Heyer & Brunt 2004). Most of these studies find results which agree with the Schmidt-Kennicutt law within uncertainties. However, a big limitation in gaining further insight into this relation arises when trying to compare results obtained from different studies, which use different prescriptions to quantify star formation. The advent of large multi-wavelength surveys has been a breakthrough in studying the ISM in external galaxies in a consistent way. In particular, the SINGS survey (Spitzer Infrared Nearby Galaxies Survey, Kennicutt et al. 2003) mapped 75 nearby galaxies in infrared wavelengths. Follow up surveys of nearby galaxies usually include these 75 galaxies. That is the case of *GALEX* NGS (Galaxy Evolution Explorer Nearby Galaxy Survey, Gil de Paz et al. 2007), which obtained UV

maps of ~ 1000 nearby galaxies. Combining these datasets with Hα ground-based observations enabled a robust quantification of the obscured and unobscured star formation for a large sample of galaxies (Calzetti et al. 2005, 2007; Leroy et al. 2008, 2013). In addition to these surveys, the VLA (Very Large Array) large program THINGS (The H I Nearby Galaxy Survey, Walter et al. 2008) mapped 34 galaxies in the 21 cm line, and the large IRAM (Institut de Radioastronomie Millimétrique) program HERACLES (Heterodyne Receiver Array CO Line Extragalactic Survey, Leroy et al. 2009) mapped 48 galaxies in the CO (2 – 1) transition. These high resolution observations of star formation and gas tracers made it possible to perform a sub-kilo-parsec characterization of the star formation law in nearby galaxies (e.g. Leroy et al. 2008, 2013; Bigiel et al. 2008; Schruba et al. 2011).

All these results coincide in finding a strong nonlinear correlation between SFR and total (H I +H $_2$) gas surface density (N ~ 1.4 – 3.1), as well as a shallower correlation when using molecular gas surface density only (N ~ 1.0 – 1.4). The linear relation between Σ_{SFR} and Σ_{H_2} suggests that the main connection between star formation and gas is actually driven by the molecular gas fraction. Figure 1.6, taken from Bigiel et al. (2008), shows the star formation law obtained from their resolved measurements, together with results from other studies. In this plot, at least two regimes can clearly be observed: a low density regime, where Σ_{SFR} is basically uncorrelated to Σ_{gas}; and a higher density regime where a strong linear correlation is observed. The border between these two regimes actually coincides with the atomic-molecular phase transition at $\Sigma_{H_I} \sim 10\,M_\odot\,pc^{-2}$ (or $N(H\,I) \sim 10^{21}\,cm^{-2}$). Therefore, the high density regime is strongly dominated by H $_2$. In the high-density regime, stars form at a fixed efficiency (Leroy et al. 2008; Schruba et al. 2011), whereas in regions dominated by H I, star formation efficiency is proportional to Σ_{gas}. These two density regimes are therefore characterized by different star formation efficiencies (Schruba et al. 2011).

Another interesting point is to look at the starburst regime. Starburst galaxies are forming stars at very high rates (~ 100 $M_\odot$ pc^{-2} to up to 1000 $M_\odot$ pc^{-2} in the most luminous ULIRGS). They have very high contents of molecular gas, as compared to normal spiral galaxies (See Fig.1.6), with typical surface densities of $10^2 - 10^4\,M_\odot\,pc^{-2}$. Such high SFRs would result in the gas reservoir available for star formation to be depleted in ~ 100 Myr (for a normal star forming galaxy, the mean depletion time is of the order of ~ 2 Gyr, Leroy et al. 2013). This short timescale implies that starburst regimes are transient phenomena, and are probably caused by mergers. Recent observations of starburst galaxies at larger redshifts $z \geq 2$ (e.g., Daddi et al. 2010; Genzel et al. 2010) show that the star formation law interpretation depends strongly on X_{CO}. There are two possibilities. The first one is to use the Galactic X_{CO} factor to derive molecular gas surface densities. In this case, starburst galaxies[5] roughly follow the supra-linear Schmidt-Kennicutt law

[5]Actually the relation measured by Kennicutt (1998) included starburst galaxies, which are very important in providing enough dynamic range of Σ_{gas} in those measurements.

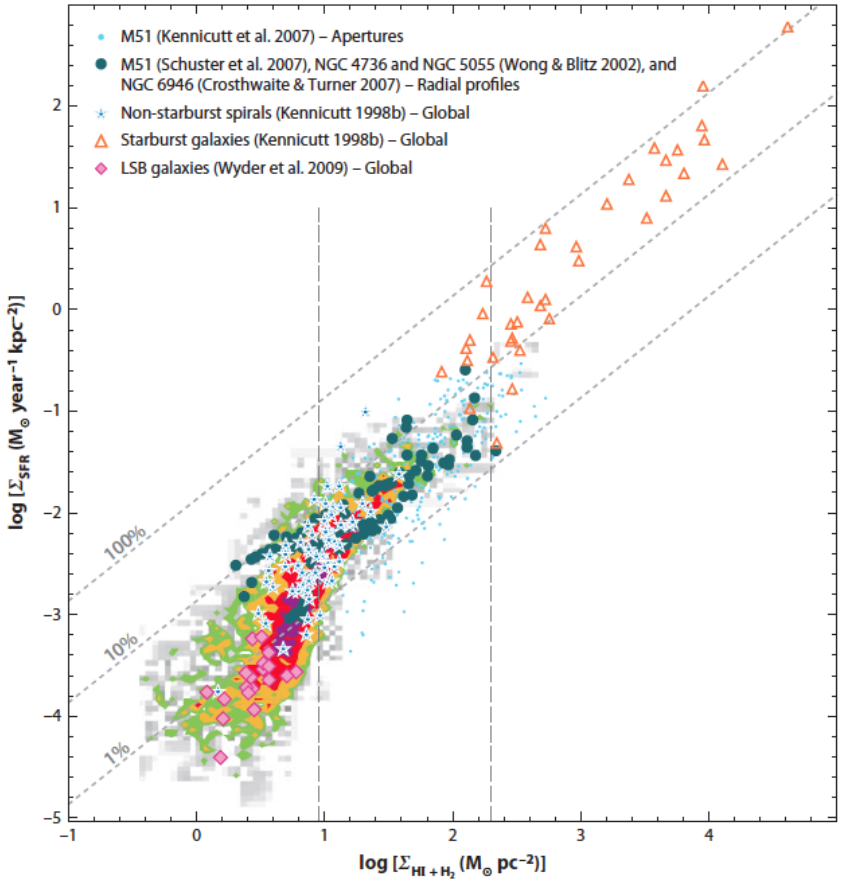

Figure 1.6 **Star formation law.** Figure from Kennicutt & Evans (2012), adapted from Bigiel et al. (2008), that shows the relation between star formation rate and total gas (H I + H_2) surface densities for various sets of measurements: subregions of SINGS galaxies (gray, green, yellow, and red), individual apertures in M51 (light blue dots, Kennicutt et al. 2007), radial profiles (dark blue filled circles) from M51 (Schuster et al. 2007), NGC 4736 and NGC 5055 (Wong & Blitz 2002), and NGC 6946 (Crosthwaite & Turner 2007), disk-averaged measurements (Kennicutt 1998) from 61 normal spiral galaxies (dark blue stars) and 36 starburst galaxies (orange triangles), and global measurements from 20 low-surface-brightness (LSB) galaxies (magenta filled diamonds, Wyder et al. 2009). All calibrations were set equal for all data sets. The three dotted diagonal lines represent three constant global star formation efficiencies. The light gray vertical line on the left shows the turnover point of the SF law for low surface densities ($\Sigma_{\rm H\,I} \sim 10\,{\rm M}_\odot\,{\rm pc}^{-2}$), and the dark gray vertical line on the right marks the change from intermediate to high –density (or starburst) regime ($\Sigma_{gas} > 100-300\,{\rm M}_\odot\,{\rm pc}^{-2}$).

(See Fig. 1.6). The second possibility, as discussed in Sec. 1.1.2, is to use a lower $X_{\rm CO}$ value for this starburst regime. In this case, starburst galaxies move leftward on the plot. They conserve the same slope ($N \approx 1.2-1.4$), but are systematically offset by a factor of 10 to the relation for normal star-forming galaxies, forming a parallel relation. This result suggests there is relation for

normal star-forming galaxies (which defines an equilibrium state), and a relation for the starburst mode, in which star formation efficiency is enhanced by a factor of 10.

Gao & Solomon (2004) studied the star formation relation using HCN, a high-density tracer. They study galaxy-averaged GMCs in infrared and normal spiral galaxies. They find a linear correlation between star formation (measured through the total far-IR luminosity) and total dense molecular gas content (global HCN luminosity). Their conclusion is that global star formation efficiency is driven by the amount of dense gas present in GMCs. Moreover, they find that dense gas measurements in normal galaxies yield the same relation as measuring dense gas in infrared galaxies. A possible explanation for this would be that the apparent bimodal star formation law only reflects different dense gas fractions within the regions studied with a lower density tracer (CO). Other studies that use different tracers to probe molecular gas suggest that the slope in the star formation relation changes continuously when going from low density tracers (CO) to higher density tracers (e.g., HCN and HCO^+, Juneau et al. 2009), pointing out the predominance of dense gas in driving the star formation relation. Furthermore, Lada et al. (2010) analyzed nearby molecular gas clouds by means of infrared extinction maps, and found evidence of "SFR being directly related to the amount of dense gas within a cloud". In a subsequent paper, Lada et al. (2012) explain the scatter present in the galactic and extragalactic power law relations as differences in dense gas fractions within molecular gas. Consequently, since star formation would exclusively take place within high density gas, any diffuse CO emission would overestimate the masses of star forming GMCs.

1.4 Galactic Disk Structure

1.4.1 Scale Height

So far I have focused on the structure of the ISM on small scales. Now I will depict the large scale structure of the neutral gas within spiral star-forming galaxies, with particular focus on their scale heights. Directly measuring neutral gas scale heights is very difficult due to beam smearing, line-of-sight crowding, and optical depth effects, even when considering edge-on galaxies (Banerjee et al. 2011). However, for galaxies with large scale disk morphologies the observed (macroscopic) velocity dispersions can be related to the vertical density profile of the observed tracer. The density profile is set by hydrostatic equilibrium, such that the gravitational weight of the components being considered is balanced by gas pressure, i.e., its velocity dispersion. For the general case of a multi-component stellar and gaseous disk, the vertical density profile of each component needs to balance the combined gravitational field of stars, gas, and dark matter.

Assuming a thin disk (i.e., ignoring the radial dependence) and an axisymmetric potential, the hydrostatic equilibrium equation for a multi-component disk is (Rohlfs 1977):

$$\frac{\langle (v_z)_i^2 \rangle}{\rho_i} \frac{d\rho_i}{dz} = (K_z)_s + (K_z)_{HI} + (K_z)_{H_2} + (K_z)_{DM} \tag{1.3}$$

where $\langle (\mathrm{v}_z)_i^2 \rangle$ is the mean square velocity of the i^{th} disk component[6], ρ_i is the mass density of the i^{th} component, and $(\mathrm{K}_z) = -\delta\psi/\delta z$ is the force per unit mass along the z-axis (ψ being the corresponding potential), with the different subscripts denoting s for stars, H I and H_2 for the two gas components, and DM for the force due to the dark matter halo. Each component has a different vertical velocity dispersion. Therefore, even though all components experience a common gravitational potential, the difference in their velocity dispersions will yield a different density distribution for each of them. The second relevant equation is given by the Poisson equation, which for a thin axisymmetric disk is given by:

$$\frac{d^2\psi_s}{dz^2} + \frac{d^2\psi_{HI}}{dz^2} + \frac{d^2\psi_{H_2}}{dz^2} = 4\pi G \left(\rho_s + \rho_{HI} + \rho_{H_2}\right) \tag{1.4}$$

Solving these equations gives the vertical density distribution of each component. Useful approximations to the full numerical solutions are given by Elmegreen (1989) and Narayan & Jog (2002). A particular result is that an increase in velocity dispersion causes an increase in scale height at a fixed gravitational field (i.e., surface density), while an increase in surface density decreases the scale height at a fixed velocity dispersion. The hydrostatic equilibrium assumption, therefore, let us link the observables for face-on galaxies (i.e., velocity dispersions) and edge-on ones (i.e., scale heights).

Accurately measuring velocity dispersions of gas in galaxies can give us information of their spatial extent in the direction perpendicular to the disk. The observed lines are broadened through different mechanisms. The microscopic processes operate on atomic or molecular scales, whereas the macroscopic ones act on scales larger than the photon's mean free path (which is about 100 AU for typical ISM conditions). The most important microscopic processes are natural and thermal (or Doppler) broadening. *Natural broadening* arises as a consequence of Heisenberg's uncertainty principle ($\Delta \mathrm{E}\, \Delta \mathrm{t} \gtrsim \mathrm{h}/2\pi$). The transitions between two energy levels do not have an exact value, but are spread as ΔE. This spread in energies is reflected as a spread in frequencies of the emitted/absorbed photons. On galactic scales, this broadening mechanism is negligible, as typical FWHM (full width at half maximum) for allowed transitions are of the order of $\sim 10^{-5}$ nm. *Thermal broadening* is more significant. Gas particles move at random velocities that follow a Maxwell-Boltzmann distribution characterized by the kinetic temperature T_k. The mean squared velocity of this distribution is related to T_k by $\langle \mathrm{v}^2 \rangle = 3\mathrm{kT}_k/\mathrm{m}$ (where k

[6]This is usually taken as the velocity dispersion at radius R, and is then treated as isothermal along z.

is Boltzmann's constant and m is the particle's mass). These random velocities Doppler-shift the emitted (or absorbed) photons's frequency with respect to the rest-frame energetic transition. The resulting line's velocity dispersion is given by $\sigma = (kT_k/m)^{1/2}$ (which corresponds to $\mathrm{FWHM} = 2\sqrt{2\ln 2} \approx 2.354\,\sigma$). Typical thermal velocity dispersion values in the neutral ISM are ~ 8 km s^{-1} for H I at 8 000 K, and $\lesssim 1$ km s^{-1} for CO at 10 K. Observational results typically measure values for H I line widths that range from 5 – 15 km s^{-1} (e.g. Petric & Rupen 2007; Tamburro et al. 2009), whereas velocity dispersions measured for molecular clouds range from 2 – 8 km s^{-1} (Bolatto et al. 2008; Heyer et al. 2009). These velocity dispersions clearly exceed the expected thermal values. Additional non-thermal broadening mechanisms are needed to explain this excess.

1.4.2 Turbulence

There has been a long debate regarding the importance and origin of turbulence in the ISM. This debate dates from 1951, when von Weizsäcker (1951) proposed a theory in which hierarchical gaseous structures are formed in the ISM as a result of shock waves from supersonic turbulence, stirred on the largest scales by differential rotation, and dissipated on the smallest scales by atomic viscosity. Since then, different observational and theoretical studies have built on this concept (for a good review see Elmegreen & Scalo 2004). It was not until the results from Larson (1981) came out, that certain consensus on the presence of turbulence in the ISM was reached. The recognition of turbulent processes taking place at larger scales came some years later, when the structural complexity of diffuse gas and molecular clouds was observed (starting with the images obtained from the Infrared Astronomical Satellite (IRAS), Low et al. 1984; Bally et al. 1987). By the end of that decade, one of the most popular cloud-formation mechanisms in the ISM was compression of gas by converging turbulent flows (Elmegreen & Scalo 2004). In spite the large amount of studies that have been carried out to characterize turbulence in the ISM, many questions still remain unanswered. There is no conclusive understanding on the (relative importance of) sources that inject turbulent energy into the ISM, nor on which scales it gets dissipated. Numerical hydrodynamical and MHD (magneto-hydrodynamical) simulations show that turbulence should decay in less than a crossing time (e.g., Mac Low et al. 1998; Avila-Reese & Vázquez-Semadeni 2001). Since non-thermal line widths are clearly measured in molecular clouds, their lifetimes would set the energy injection rate needed in order to maintain steady state turbulence. Traditionally it has been thought that GMC lifetimes are much larger than their free-fall times (Blitz & Shu 1980), but recent results find that they might be comparable, or even smaller, than their crossing times (e.g. Ballesteros-Paredes et al. 1999; Hartmann 2003). This lack of consensus makes it hard to establish the timescales at which turbulence should be injected into the ISM. In any case, different mechanisms have been proposed as drivers of turbulence. Local energy injection could be accounted for by processes related to star

formation: jets and winds from low mass stars, and H II regions and stellar winds from massive stars; and by processes related to the final stages of stars: supernovae explosions and expanding super bubbles. Global energy injection could be accounted for by spiral shocks or shear. Some proposed processes would act at all scales: magneto rotational instabilities and accretion.

1.4.3 Observational Properties of Neutral Gas

Regarding galactic scales, H I disks are the most extended observable radial components in spiral galaxies[7]. However, in the centers of spiral galaxies, depletions in H I gas are common (Combes & Becquaert 1997). Leroy et al. (2008) studied 12 nearby spiral galaxies and found that the atomic gas distribution is roughly constant out to the optical radius[8] (r_{25}) with $\Sigma_{H_I} \sim 6\,M_\odot\,pc^{-2}$. The vertical structure of the H I disk is typically characterized by two Gaussian scale heights (Tielens 2005), one for WNM ($\sim 220-400$ pc) and one for CNM (94 pc). In the outer disks, flaring of the H I layers has been observed (Olling 1996; O'Brien et al. 2010). Since the surface densities of stars and gas decrease exponentially with radius, the flaring originates when the dark matter halo starts dominating the potential.

Observations show that molecular gas in spiral galaxies declines nearly exponentially as a function of radius. Leroy et al. (2009) observed 18 nearby galaxies on CO (2 – 1) and found exponential scale-lengths ranging from 0.8 – 3.2 kpc (or $0.2 \pm 0.05\,r_{25}$). They also find that the ISM is mostly H_2 within $0.5\,r_{25}$. GMCs scale height is traditionally set at ~ 75 pc, which is the value measured for the Milky Way (Sanders et al. 1984). However, some observational results have shown that there might be an additional molecular gas component with a significantly larger scale height. Combes & Becquaert (1997) studied the two nearly-face on galaxies NGC 628 and NGC 3938, and found similar H I and CO vertical velocity dispersions. They interpret this result as evidence for a mixture of both atomic and molecular gas, which would constitute a single kinematical component. The scale height of the edge-on galaxy NGC 891 has been investigated by Garcia-Burillo et al. (1992). They detect molecular emission at ~ 1 kpc above the disk, which they interpret as the presence of a low-density thick disk component (this is confirmed by new large-scale mapping of the galaxy with the IRAM 30 m telescope, Garcia-Burillo, priv. comm.). Recently, Pety et al. (2013) published an in-depth study of M 51, where they convincingly show that this galaxy has a diffuse molecular disk with a velocity dispersion that is much larger than the molecular gas that is associated with GMCs in the star-forming disk. These observational results point to open questions regarding the vertical scale height of molecular gas, which is closely related to the physical properties of this gaseous component.

[7] In many galaxies they are typically 3 times radially more extended than their stellar disk counterparts (Kalberla & Kerp 2009).

[8] Defined as the radius of a galaxy to the 25^{th} magnitude isophote.

1.5 Observing Neutral Gas

The transitions relevant to the study of H I and CO line emission fall in the cm and mm range of the electromagnetic spectrum. They are observed with radio telescopes, either single-dish or interferometers. Radio wavelengths lie in a preferential location regarding the transmission windows of the electromagnetic spectrum through the Earth's atmosphere. The narrow optical window is delimited at the higher frequencies by the UV absorption from the ozone layer, while at the infrared end, water vapor and carbon dioxide effectively block radiation. The radio window, on the other hand, spans a large range of frequencies that are practically free of atmospheric absorption. It is limited at long wavelengths (greater than a few meters) by the ionosphere and at wavelengths shorter than ~ 2 cm by increasing atmospheric absorption. This large range of frequencies is divided in different bands: high frequency (HF, below 30 MHz), very high frequency (VHF, 30 – 300 MHz), ultra high frequency (UHF, 300 – 1000 MHz), microwave (1000 – 30 000 MHz), millimeter-wave, and sub-millimeter-wave. Among the many differences between radio and optical astronomy, I will point out two: the design of the instruments needed to carry out the observations and the resulting data products. Photons at radio wavelengths have much lower energy than optical ones, and cannot be detected in the same way. Optical detectors (i.e., charged coupled devices or CCDs) generate a response proportional to the individual number of photons striking the detector's surface, and the intensity of the source generating the photons can be directly measured. The energy in radio photons is too low to generate such a response, and therefore other detection techniques are used. By measuring the phase and amplitude of the electromagnetic wave, radio receivers detect the wave nature instead of the photon nature of radiation. By means of spectrometers, this information can be divided in frequency bins and the resulting data product is a cube with two spatial dimensions and one frequency (or velocity) dimension.

Single-dish telescopes, especially after the development of multi-beam heterodyne receiver arrays, provide a large instantaneous field of view and good sensitivity, although at limited spatial resolution ($\theta \propto \lambda/\mathrm{D}$, with D being the antenna's aperture[9]). Interferometers, on the other hand, provide higher spatial resolution, with the drawback that not all spatial scales can be recovered. To understand why this happens, let us think first of a two antennae interferometer (See Fig. 1.7 and following Burke & Graham-Smith (2014)). The two antennas are separated by a baseline (**b**), and they are observing a point-source in the direction **s**. The output voltage of the first antenna (V_1) will have a geometric delay with respect to the second antenna (V_2) set by $\tau_g = \mathbf{b} \cdot \mathbf{s} / c$. Considering a quasi-monochromatic interferometer centered on frequency $\nu = \omega/2\pi$, the expressions for the output voltages are:

$$V_1 = a_1 \cos 2\pi\nu(t - \tau_g) \qquad V_2 = a_2 \cos 2\pi\nu t \tag{1.5}$$

[9] As an example, a 30 m antenna observing at 3 mm yields an angular resolution of $\sim 23''$.

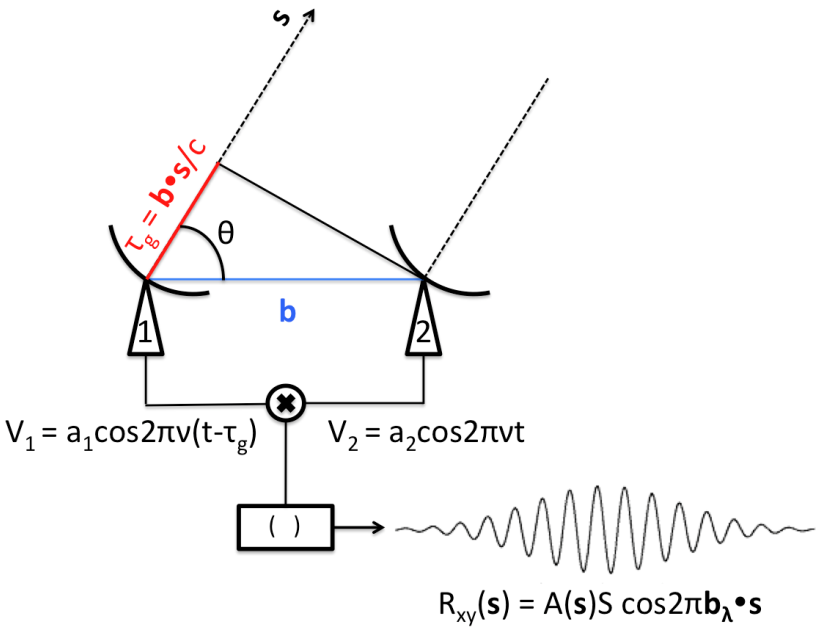

Figure 1.7 **Two antennae interferometer.** The direction to a distant point-source is given by the unit vector **s**. The antennas are separated by a baseline **b** (blue). The output voltage of the fist antenna (V_1) will have a geometric delay with respect to the second antenna (V_2) given by τ_g (red), the projection of the baseline on the direction of the pointing. The output from both antennas is then correlated yielding a response R_{xy} which is proportional to the point-source flux density (S), and whose phase depends on the observed frequency and delay. The sinusoidal output fringe results from the wave interference generated by the geometric delay between the antennas. The fringe period depends on the baseline measured in wavelengths, in such a way that longer baselines yield shorter periods, and vice versa.

These voltages are then multiplied and averaged over time by the correlator. The resulting output has an amplitude proportional to the point-source flux density (S) and the effective antenna area A(**s**), while its phase depends on the observed frequency and the delay between the two antennas:

$$R_{xy}(\tau_g) \;=\; A(\mathbf{s})S\,\cos 2\pi\nu\tau_g \;=\; A(\mathbf{s})S\,\cos 2\pi\nu\mathbf{b}\cdot\mathbf{s}/c \tag{1.6}$$

If the baseline vector (**b**) is measured in units of wavelengths ($\mathbf{b}_\lambda = \mathbf{b}/\lambda$) the expression for the cross-correlation can be written as:

$$R_{xy}(\mathbf{s}) \;=\; A(\mathbf{s})S\,\cos 2\pi\mathbf{b}_\lambda\cdot\mathbf{s} \tag{1.7}$$

The geometric delay between the antennas creates a sinusoidal variation of the output (R_{xy}) which reflects the interference pattern. This sinusoidal behavior appears like fringes. It gives the sky's

sensitivity pattern for each pair of antennas, which is an oscillation between constructive and destructive interference. The fringe phase is given by $\Phi = 2\pi\nu b\cos\theta/c$, and is able to measure source positions very accurately as long as the projected baseline $b\cos\theta$ is many wavelengths long. An example of the fringes produced by two pairs of antennas with different separations is shown in Fig. 1.8.

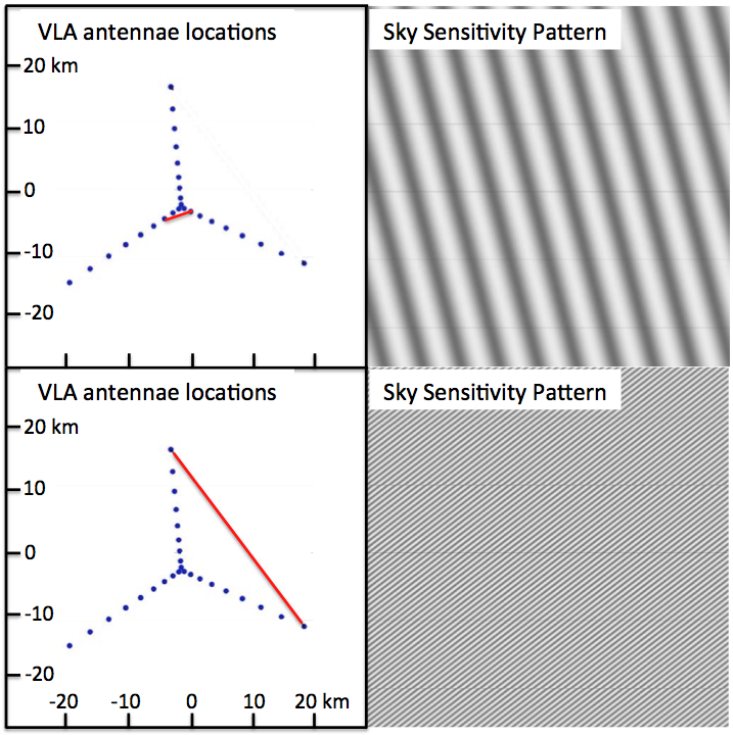

Figure 1.8 **Sky sensitivity pattern (fringes) for a pair of antennas.** As an example, I show on the *left* panel an antennae configuration from the Very Large Array (VLA). In each case, a selected pair of antennas with different baselines is shown: short baseline (top) and long baseline (bottom). On the *right* panels I show the interference patterns (or fringes) resulting from each baseline selection. Short baselines result in broader fringes, and thus are more sensitive to extended structure. The contrary happens to long baselines, which yield narrow fringes, and are sensitive to compact structures. In all cases, the fringes are perpendicular to the baseline direction. Image taken from a presentation by Amy Mioduszewski.

So far these expressions are in terms of the time delay, but an analogous description can be made in the frequency domain as well. The Fourier transform of the cross-correlation R(t) is known as the cross-spectrum power density $S_{xy}(\nu)$ and is used to describe the interferometer's output. A Fourier transform of a time-delayed signal has a phase shift given by $2\pi\nu\tau_g$. In this way the cross-spectrum power density is given by:

$$S_{xy}(\nu) \;=\; A(\mathbf{s})S\,\exp(-\mathrm{i}2\pi\nu\tau_{\mathrm{g}}) \;=\; \mathrm{A}(\mathbf{s})\mathrm{S}\exp(-\mathrm{i}2\pi\nu\mathbf{b}_{\lambda}\cdot\mathbf{s}) \tag{1.8}$$

If the source is no longer a point-source, but is spatially extended, the flux S should be replaced by the specific intensity $\mathrm{I}_{\nu}(\mathbf{s})$. To obtain the cross-spectral density, the extended source is treated as a sum of independent point-sources, i.e., an integration over the entire radio source, after considering that radiation comes from a small element subtending a solid angle $\mathrm{d}^2\Omega$ in the direction of **s**, is performed:

$$S_{xy}(\mathbf{s}) = \int_{4\pi} A(\mathbf{s})I_{\nu}(\mathbf{s})\exp(\mathrm{i}2\pi\mathbf{b}_{\lambda}\cdot\mathbf{s}))\mathrm{d}^2\Omega \tag{1.9}$$

In the case of a multi-antenna interferometer, for each pair of antennas (*i,j*) the corresponding baseline measured in wavelength units is defined as $\mathbf{b}_{ij,\lambda} \equiv \mathbf{b}_{ij}/\lambda$. The complex visibility is finally defined as:

$$V_{ij} = \int A(\mathbf{s})I_{\nu}(\mathbf{s})\exp(\mathrm{i}2\pi\mathbf{b}_{ij,\lambda}\cdot\mathbf{s}))\mathrm{d}^2\Omega \tag{1.10}$$

This equation gives an expression of the main observables in interferometry: amplitude and phase of the complex visibility. The next step is to introduce a new right-handed rectilinear coordinate system (*u,v,w*). The *w*-axis points in the direction of the source, and lying on the perpendicular plane, *u* and *v* will be in the baseline projected directions towards East and North, respectively. This plane is known as the *uv*-plane, where all coordinate distances are expressed in wavelength units. After some approximations the expression for the visibility can be written as:

$$V(u,v) \;\approx\; \int I(x,y)\exp(\mathrm{i}2\pi(\mathrm{ux} + \mathrm{vy}))\mathrm{dxdy} \tag{1.11}$$

where it becomes clear that V(u,v) is the Fourier transform of I(x,y), and vice versa. Each pair of antennas defines a spatial frequency, given by the baseline vector projected in the *uv*-plane. At each spatial frequency (seen as a point in the *uv*-plane) the Fourier transform evaluates the source's brightness distribution. The combination of all antenna pairs define the angular frequencies that are recovered by the interferometer. The fringe spacing resulting for each antenna pair will be sensitive to structures of the size of its spacing. In this way, longer baselines, which have narrower angular fringe spacings, are sensitive to very compact scales, while shorter baselines, which have broader angular fringe spacings, are sensitive to extended structures. Different Fourier components contribute with different scales to the resulting image. Fig. 1.9 illustrates how frequency filtering would affect the output image.

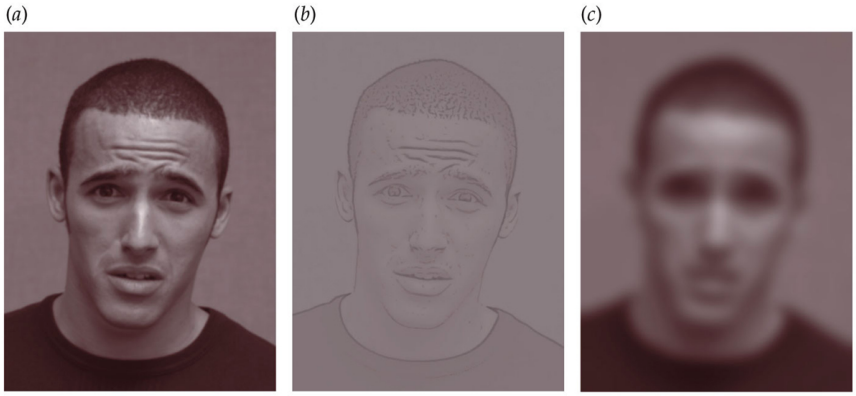

Figure 1.9 **Spatial filtering.** This figure shows in a) the real image, taking into account all frequency contributions. In b) low frequencies are filtered out, which in the case of an interferometer would mean to keep the long baselines, and thus being sensitive to compact structures only. The contrary happens in c), where high frequencies are filtered out. In the interferometer this would be equivalent to keeping short baselines, and therefore be sensitive to extended emission. I took the image from images available at the web page of the University of South Dakota.

At each instant in time, the *uv*-plane is filled by a collection of points, each point corresponding to a pair of antennas. Synthesis observations are achieved by making use of the Earth's rotation, by which the points in the *uv*-plane follow tracks with the shape of arcs. In this way the *uv* coverage improves. Missing spacings in the *uv*-plane imply a loss of the corresponding Fourier components.

The distance between antennas cannot be decreased infinitely, as the minimum separation between two of them is the antenna's diameter. This results in a gap at the center of the *uv*-plane. Missing these *uv* spacings imply that large-scale structures cannot be recovered. Interferometers can only observe structures with angular scales $\theta < \lambda/d_{min}$, where d_{min} is the minimum separation between two antennas. Consequently, the total flux, which is given by the amplitude of the visibility at the origin ($u = v = 0$) cannot be measured. To understand why, we have to go back to the principle behind Fourier transforms. The amplitude of the Fourier transform of the brightness distribution of a point source, which can be thought of as a δ function, will be a constant value extending over all *u,v* values. The transform of a Gaussian, will be a Gaussian. If the input Gaussian is broadened, it eventually becomes a uniform distribution (i.e., its width becomes infinite). In this case, the transform of a uniform distribution will yield a δ function, peaking at $u = v = 0$. In Fig. 1.10, I show the amplitude of the visibilities as a function of *u,v* radius. The gray shaded region shows the "gap" in the *uv*-plane. For a point source (green line), the total flux can be extrapolated from the existing *u* and *v* measurements, since in that case, V as a function of baseline length is constant. However, for an extended source (red line), the extrapolation is not possible, and the total flux remains unconstrained. This is known as the zero-spacing problem, and is im-

portant in the case when the observed source is large compared to λ / d_{min}. As an example, taking 12 m antennas observing at 3 mm, the interferometer would filter out any structure larger than $\sim 60''$. A solution to this problem is to combine single-dish and interferometric observations. In this way, the resolution achieved by the interferometer remains, while the total flux measured by the single-dish is recovered. I use such a combination of data sets for a part of my project.

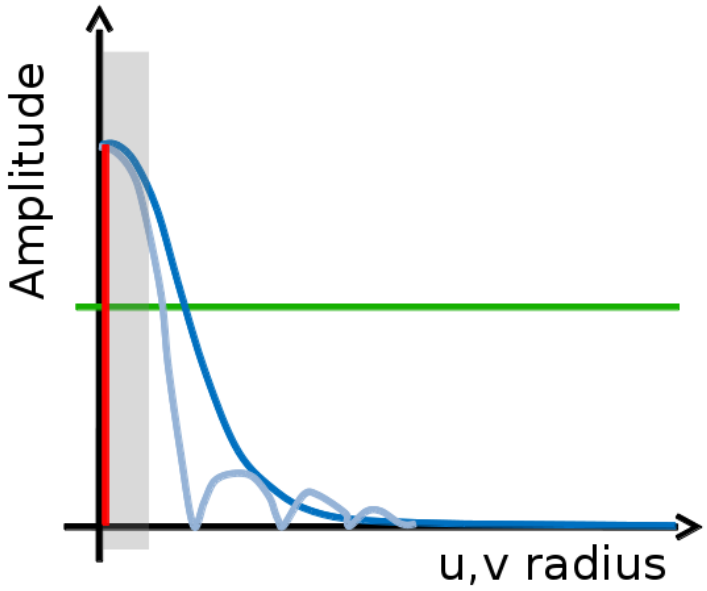

Figure 1.10 **Zero-spacing problem.** This figure shows the amplitude of the visibilities as a function of *uv* radius. The green line illustrates the Fourier transform of a δ function (point source brightness distribution), which yields a constant amplitude value. The dark blue line shows the Fourier transform of a Gaussian brightness distribution, which results also in a Gaussian. The light blue line shows a step function that represents a disk structure brightness distribution. The red line, a δ function peaking at $u = v = 0$, is the Fourier transform of a uniform brightness distribution. The shaded area shows the *u,v* pairs that are missed by the interferometer, as they correspond to baselines smaller than the minimum antenna separation. As a result of the missing spacings, in particular $u = v = 0$, the interferometer cannot measure the total flux.

CHAPTER 2

Atomic vs. Molecular Gas Velocity Dispersions[†]

The neutral atomic phases of the ISM were briefly described in the Introduction, where I also pointed out the importance of quantifying and understanding the processes giving rise to velocity dispersions in the gaseous phases of the ISM. The physical properties of neutral atomic and molecular gas are different; in particular their temperatures, which give rise to thermal velocity dispersions. So far, most extragalactic studies of velocity dispersions concentrated exclusively on studying either H I emission (Tamburro et al. 2009; Warren et al. 2012) or CO emission (Bolatto et al. 2008). The paper on which this chapter is based, presents a comprehensive study of the velocity dispersions of both the atomic and molecular gas phases within 12 nearby spiral galaxies. We use data from the VLA THINGS H I survey (Walter et al. 2008) and from the IRAM HERACLES CO survey (Leroy et al. 2009). Even with the high sensitivity of instruments like the VLA or the IRAM 30 m telescope, stacking is a useful tool to obtain robust velocity dispersion measurements. The stacking technique we apply has been previously used by Schruba et al. (2011) to obtain highly sensitive measurements of *integrated intensities* of the CO line out to large radii. In this chapter we use this method to determine robust measurements of H I and CO *velocity dispersions* within nearby galaxies.

The chapter is structured as follows. In Section 2.1 we describe our galaxy sample and the H I and CO data. In Section 2.2 we describe our stacking technique and method to determine velocity

[†]This chapter is adapted from Caldú-Primo et al. (2013)

dispersions, including a detailed description of our uncertainty determinations. In Section 2.3 we give an interpretation and discuss implications of our results.

2.1 Data

2.1.1 Sample Selection

We study 12 nearby star-forming spiral galaxies. These galaxies are drawn from a larger sample of galaxies targeted by various multi-wavelength surveys. The wavelengths we are interested in for the purpose of this study are H I (THINGS, Walter et al. 2008), CO (HERACLES, Leroy et al. 2009), FUV (GALEX NGS, Gil de Paz et al. 2007), and 24 μm (SINGS, Kennicutt et al. 2003). Our sample is chosen such that all galaxies are detected in these 4 data sets. Given this restriction, we have a selection effect as we only study spiral galaxies with a clear detection in CO, our least sensitive tracer, in at least the inner parts of the galaxies. The THINGS survey also includes irregular galaxies, which we leave out from our analysis. For the analysis we convolve all data sets to the limiting 13″ angular resolution of the HERACLES CO data. Galaxies for which this angular resolution corresponds to a linear resolution larger than 700 pc (corresponding to a distance of ∼11 Mpc) are also left out. The last cut to obtain our working sample is based on a signal-to-noise (S / N) cut of the stacked spectra (this will be explained in detail in Section 2.2). Based on this we drop out the galaxies NGC 3521 and NGC 3627. The galaxies included in this work are listed in Table 2.1, together with their adopted properties: distance, inclination, position angle, optical radius (R_{25}), and linear resolution (at 13″ angular resolution), where the latter values are taken from Walter et al. (2008).

2.1.2 Atomic Gas Data

The H I data come from the THINGS survey (Walter et al. 2008). This survey encompasses 34 nearby galaxies at distances of 2−15 Mpc. The observations have high spectral (2.6 or 5.2 km s^{-1}) and spatial (∼11″ for natural weighting) resolutions. We use the so-called "rescaled" data cubes. This flux "rescaling" is important for computing correct fluxes, but also for obtaining accurate spectral shapes. More details can be found in Walter et al. (2008, Section 3.5 and references therein). Mass surface densities are derived from integrated line emission, i.e., zeroth moment, via

$$\Sigma_{\rm HI} = 0.02\ {\rm I}_{\rm HI}\ \cos i \tag{2.1}$$

Table 2.1. Properties of the galaxies used in this study

Galaxy	D Mpc	Incl °	PA °	R_{25} kpc	Res kpc
NGC 628	7.37.3	7	20	10.4	0.46
NGC 925	9.2	66	287	14.2	0.58
NGC 2403	3.2	63	124	7.3	0.20
NGC 2903	8.9	65	204	15.3	0.56
NGC 2976	3.6	65	335	3.8	0.23
NGC 3184	11.1	16	179	11.9	0.70
NGC 3351	10.1	41	192	10.6	0.64
NGC 4736	4.7	41	296	5.3	0.30
NGC 5055	10.1	59	102	17.4	0.64
NGC 5194	8.0	20	172	9.0	0.50
NGC 5457	7.4	18	39	25.8	0.47
NGC 6946	5.9	33	243	9.8	0.37

where Σ_{HI} has units of $M_\odot$ pc^{-2} and includes a factor of 1.36 to account for heavy elements, and I_{HI} is measured in K km s^{-1}.

2.1.3 Molecular Gas Data

We obtain the CO (2 – 1) line emission from the cubes of the HERACLES survey (Leroy et al. 2009). The angular resolution of this survey is of 13″ and it has a spectral resolution of 2.6 km s^{-1}. The H_2 surface density is derived from the CO (2 – 1) line intensity by

$$\Sigma_{H2} = 6.25\, I_{CO}\, \cos i \tag{2.2}$$

where Σ_{H2} has units of $M_\odot$ pc^{-2} again including heavy elements and I_{CO} is measured in K km s^{-1}. This conversion assumes a CO line ratio of $I_{CO\,(2-1)} / I_{CO\,(1-0)} = 0.7$ and a CO (1 – 0)-to-H_2 conversion factor $X_{CO} = 2.0 \times 10^{20}$ cm^{-2} (see Leroy et al. 2009 and references therein). We note that measurements of velocity dispersions are not affected by the particular choice of the conversion factor.

2.1.4 Star Formation Tracer

In order to determine the spatial distribution of recent star formation, we use two tracers. The unobscured recent star formation is derived from the FUV emission. FUV traces O and B stars with typical ages of 20 – 30 Myr, reaching sensitivities of up to ~100 Myr (Salim et al. 2007). The embedded star formation can be accounted for using the mid-infrared 24 μm emission, which mainly comes from young stars' photons reprocessed by dust. The FUV images come from GALEX NGS (Gil de Paz et al. 2007). We make use of only the FUV band, which covers 1350 – 1750 Å at an angular resolution of $\sim 4.5''$. The photometry at 24 μm was obtained from the *Spitzer* legacy survey SINGS (Kennicutt et al. 2003). The images have a native resolution of $\sim 6''$. Using this pair of tracers we determine the star formation rate surface density ($\Sigma_{\rm SFR}$) following Leroy et al. (2012) as:

$$\Sigma_{\rm SFR} = (8.1 \times 10^{-2}\, {\rm I}_{\rm FUV} + 4.2 \times 10^{-3} {\rm I}_{24\mu{\rm m}}) \cos i \tag{2.3}$$

where $\Sigma_{\rm SFR}$ has units of $M_\odot$ yr^{-1} kpc^{-2}, and FUV and 24 μm are measured in MJy sr^{-1}.

2.2 Methodology

2.2.1 Stacking the Spectra

Our aim is to obtain robust measurements of velocity dispersions. This requires both high S / N line profiles and a robust method to measure velocity dispersions. To attain this requisite, we average many spectra over significant sub-regions inside the galaxies. Individual spectra peak at different velocities in the galaxy due to rotation and large scale gas motions. Schruba et al. (2011) used the first moment of the H I emission to shift the spectra to a common velocity so that the shifted spectra could be coherently stacked. Following that work, we shift the spectra using the first H I moment of intensity for NGC 628, NGC 925, NGC 3184, NGC 3351, NGC 4736, NGC 5194, NGC 5457, and NGC 6946. For NGC 2403, NGC 2903, NGC 2976, and NGC 5055 we have high-quality Hermite h_3 velocity maps (de Blok et al. 2008) available and we use those instead to perform the shifting. The latter velocity fields are superior to the first moment maps in constraining the 'peak' of the emission (see for details de Blok et al. 2008), and indeed stacking yields velocity dispersions that are of the order of 1.5 km s^{-1} lower than when using the first moment maps.

The procedure is then as follows: For each line of sight we take either the H I or CO spectrum and shift it by its Hermite h_3 or its first moment map H I velocity value. As shown in Schruba

et al. (2011), the H I mean velocity is an excellent proxy for the CO mean velocity (we have also tested this using the CO velocity field for the shifting, see discussion Section 2.2.3.1). Once all of the spectra are shifted to a common velocity, they are ready for coherent stacking over larger regions.

We stack the spectra based on different physical properties characterizing individual lines of sight: galactocentric radius, and star formation rate, atomic hydrogen, molecular hydrogen, and total gas (atomic + molecular) surface densities. For each parameter we define bins that cover the complete range of parameter values measured in the galaxies and stack the shifted spectra inside these bins.

Stacking by Galactocentric Radius Many galactic properties vary with radius. It is therefore interesting to investigate possible trends in velocity dispersion as a function of this parameter. We use bins 15″ wide, i.e., somewhat larger than our angular resolution. These bins have linear sizes that range from 260 to 800 pc in our selected galaxies. We are investigating bins up to R_{25} (for the equivalence in kpc see Table 2.1) which gives 8 – 22 bins per galaxy.

Stacking by SFR Surface Density It is suggested that the local rate of star formation is closely linked to the velocity dispersion in the gas (e.g., Tamburro et al. 2009). To search for such a correlation, we select regions of different levels of recent star formation rate density as traced by a combination of FUV and 24 μm intensities. We define logarithmic bins of size of 0.1 dex between 10^{-3} and 10^{-1} $M_\odot$ yr^{-1} kpc^{-2}. The number of bins per galaxy vary between 8 and 20.

Stacking by H I Surface Density We also separate the lines of sight by different H I mass surface densities. We define bins of 3 $M_\odot$ pc^{-2} within a range of 0 – 30 $M_\odot$ pc^{-2} providing 3 – 9 bins per galaxy.

Stacking by H_2 Surface Density In this case we divide the lines of sight by H_2 mass surface density using bins 5 $M_\odot$ pc^{-2} wide and ranging over 0 – 50 $M_\odot$ pc^{-2}. The number of bins per galaxy varies between 2 and 10.

Stacking by Total Gas Surface Density For the total gas surface density, defined as $\Sigma_{HI+H2} = \Sigma_{HI} + \Sigma_{H2}$, we again use bins 5 $M_\odot$ pc^{-2} wide covering a range of 0 – 50 $M_\odot$ pc^{-2} giving us 3 – 10 bins per galaxy.

2.2.2 Measurement of Velocity Dispersions

After stacking the spectra we need a consistent way of measuring velocity dispersions. For simplicity we will proceed to fit the data with a single Gaussian. Studies like Petric & Rupen (2007) show that even though a single-Gaussian function does not adequately describe the line

shapes of H I spectra, the width of the H I line is well characterized by it. As the purpose of this study is to provide a global measurement of line widths, we fit each spectrum with a single Gaussian. To perform the fit we take a window centered on the peak of emission (in this case zero velocity after shifting) and of 100 km s^{-1} total width. We use the `MPFIT` function in `IDL`, which is a least-squares curve fitting procedure. The free parameters we determine by fitting are the line center velocity, the peak amplitude, and the velocity dispersion.

To ensure good S/N, we exclude (stacked) spectra with peak amplitudes lower than 5σ. The fitting procedure allows us to check whether the spectra are best fitted with a double horn profile, which is usually the case for very broad spectra and spectra with clear multiple velocity components. After the fitting is done, and to keep the analysis and determination of the velocity dispersion as simple and reliable as possible, we leave out double horn spectra which amount to 4.5% of the high S/N spectra of our data set. These double-horn profiles are found in the center-most parts of galaxies ($R \lesssim 0.2\ R_{25}$), where generally strong non-Gaussian features are observed. At larger radii H I spectra is in general smooth even beyond R_{25}. However, CO is more centrally concentrated in spiral galaxies. Schruba et al. (2011) studied the azimuthally averaged radial profiles of CO in a similar sample of galaxies and were able to detect CO out to $\sim R_{25}$. Here we restrict our analysis to the regions where we obtain high S/N emission in both tracers. In Figure 2.1 we show the resulting stacked H I and CO spectra for one SFR bin in NGC 6946 as an example.

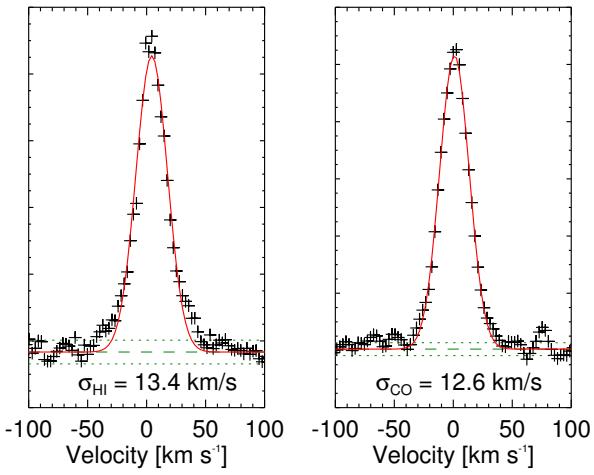

Figure 2.1 **Example of a stacked spectrum within NGC 6946.** This stacked spectra result from averaging together individual lines-of-sight which belong to a SFR bin of $(8-10)\times10^{-3}$ M$_\odot$ yr^{-1} kpc^{-2}. Left: H I spectrum, Right: CO spectrum. The black crosses are the measured values. We perform a Gaussian fit to the spectra (red solid line) in order to determine the velocity dispersion. The green dashed line represents the zero level, whereas the dotted green lines show the 1σ rms noise level.

2.2.3 Uncertainties Determination

2.2.3.1 Shifting using H I Velocity Fields

To align the H I and CO spectral lines at a common velocity, we use the H I mean velocity map or Hermite h_3 map (where available) at its native resolution. This may induce an extra broadening in the stacked CO spectra if there are significant deviations between the local CO velocity compared to the H I velocity. Schruba et al. (2011) tested for differences between H I and CO velocities for individual lines-of-sight at a 13″ resolution (see their Fig. 1). They find a median $\overline{v}_{\rm CO} - \overline{v}_{\rm HI}$ of -0.22 km s^{-1}, i.e., consistent with no shift considering our channel width of 2.6 km s^{-1}. In addition, we perform the following test on NGC 6946, one of the brightest galaxies in CO in our sample for which we can derive a reliable CO velocity field. Instead of using the H I velocity field to shift the observed spectra before stacking, we use the respective CO one. We carry out the subsequent analysis in the exact same way. The velocity dispersions of the stacked H I and CO spectra have a median difference of less than 1 km s^{-1}, again smaller than the channel width. We conclude that no significant extra broadening is introduced to the CO stacked spectra by shifting using the H I velocity fields.

2.2.3.2 Velocity Dispersions Obtained Without Stacking

We also check whether shifting and stacking spectra naturally introduces a spurious widening in the measured velocity dispersions. We use NGC 628 and NGC 2403 to address this issue. Using the original data cube, we fit a Gaussian to each line of sight independently, i.e., without stacking any spectra. We exclude spectra using the same restrictions as with the stacked spectra (leaving out low S / N spectra and spectra with clear non-Gaussian features). Then, for a given stacking region we compare the median value of velocity dispersions of individual lines of sight to the velocity dispersion of the stacked spectrum. Typically, the latter values are larger by 1.4 km s^{-1} with a 1σ dispersion of 1.2 km s^{-1}. Since this difference is again significantly smaller than our channel width of either 2.6 or 5.2 km s^{-1}, we deem this effect insignificant to our conclusions. A detailed analysis of fitting individual CO and H I spectra in nearby galaxies is presented in K. M. Mogotsi et al. (submitted).

2.2.3.3 Galaxy Inclination

Galaxy inclination may affect the measured velocity dispersions as highly inclined galaxies' lines of sight probe larger lengths through the galactic disk. Thus, one line of sight includes gas moving at different velocities, leading to a broadening of the observed line profile. To test

the importance of this effect, we show in Fig. 2.2 for each galaxy the average $\sigma_{\rm HI}$ value (black plus signs) and the average $\sigma_{\rm CO}$ value (red crosses) as functions of galaxy inclination. The blue diamonds show the ratio of $\sigma_{\rm HI}/\sigma_{\rm CO}$. We use the Spearman's rank correlation coefficients to quantify the magnitude of correlation. The coefficients we obtain are 0.58, 0.48, and 0.27 for $\sigma_{\rm HI}$, $\sigma_{\rm CO}$, and $\sigma_{\rm HI}/\sigma_{\rm CO}$, respectively. These numbers tell us that there is not a significant correlation between velocity dispersion and galaxy inclination, as is already apparent from Figure 2.2.

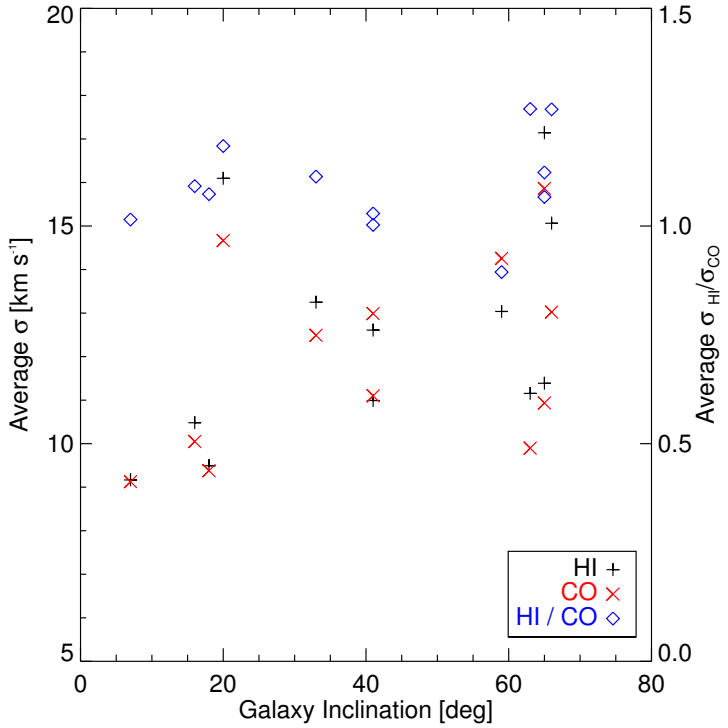

Figure 2.2 **Correlation of galaxy-averaged velocity dispersion with galaxy inclination** for: *left y–axis:* atomic gas (black plus symbols) and molecular gas (red crosses), and *right y–axis:* their ratio (blue diamonds). The measured velocity dispersions correlate at most weakly with galaxy inclination.

2.2.3.4 Beam Smearing

As the telescope beam is not infinitely small, it inevitably averages over gas moving at different velocities. This will affect determined velocity values, especially in regions of large velocity gradients, i.e., in the inner regions of galaxies, and in highly inclined galaxies. To quantify the beam smearing, we model galaxies using the task `GALMOD` in the Groningen Image Processing System (`GIPSY`[1]). This task allows us to model observations of the H I gas in a spiral galaxy.

[1] www.astro.rug.nl/~gipsy/

We generate galaxies with $\Sigma_{\rm HI} = 5 \times 10^{21}\,{\rm cm}^{-2}$, velocity dispersion of $\sigma = 10\,{\rm km\,s}^{-1}$, and *sech*^{2} vertical density profile, which are typical values for spiral galaxies. All linear sizes were calculated assuming a distance of 7.8 Mpc, the mean distance of our sample. We here present the results for a rotation curve that has a linear increase in velocity from 0 in the center of the galaxy, reaching 200 km s^{-1}in the first 2 kpc (52″). This simple model rotation curve is in a broad sense the most similar to the average rotation curves of our sample. We use four different inclinations for the galaxies: 0°, 30°, 60°, and 80°, and perform the exact same analysis as with the observed galaxies, accounting for resolution. We show the results in Fig. 2.3. The optical radius value of $R_{25} = 11.8$ kpc is the average value of our sample of galaxies. Galaxies inclined by 80° have 2.5 times larger 'observed' velocity dispersions, especially toward the galaxy center. Galaxies at intermediate inclinations (30° or 60°) are only affected in the very central parts at $R \lesssim 0.2\,R_{25}$. On the other hand, for $R \gtrsim 0.2\,R_{25}$, the beam smearing effect is comparable to or smaller than the channel width (2.6 or 5.2 km s^{-1}). Since the highest inclination of our galaxy sample is 66°, by excluding points inside $0.2\,R_{25}$ in the histogram plots (Fig. 2.5), we are left with points for which beam smearing only has a minor effect.

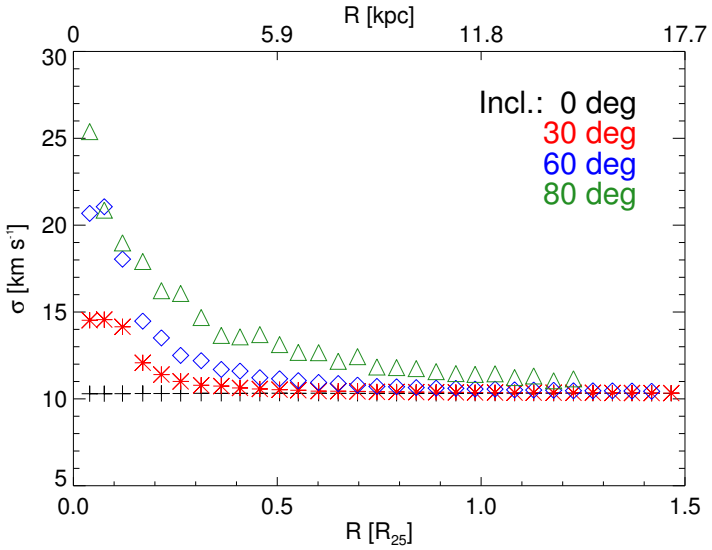

Figure 2.3 **Line broadening by beam smearing.** Measured H I velocity dispersion values obtained from model galaxies generated by the `GALMOD` task in `GIPSY`. We model a galaxy at various inclinations: black crosses for face-on, red asterisks for 30° inclination, blue diamonds for 60°, and green triangles for 80°. Beam smearing becomes more important for highly inclined galaxies and in the centermost parts of galaxies. Thus, we exclude data at $R < 0.2\,R_{25}$ from the remaining analysis.

2.2.3.5 Statistical Effects in Stacked Spectra

We want to test how the number of spectra and observational noise is affecting the resulting stacked spectra and derived velocity dispersion measurements. To test the former, we do the following: if for a certain bin the stacked spectrum consists of n different individual spectra, we randomly draw n times a spectrum from these spectra, allowing for repetition. We then stack the selected spectra and measure the velocity dispersion of the resulting bin. We repeat this procedure 1000 times for each bin and the resulting uncertainty is taken as the 1σ uncertainty of the measured velocity dispersions. To test the latter, we take the original stacked spectra and add random noise to each of the spectra before fitting. The fitting is done on the "noisy" spectrum. We perform this procedure again 1000 times, and the resulting uncertainty is taken again as the 1σ dispersion of the obtained measurements. The total uncertainty due to statistical effects is the sum in quadrature of the two uncertainties. These are the error bars plotted in Fig. 2.4 and in Figures 2.6 – 2.11.

2.3 Results and Discussion

2.3.1 Trends of Velocity Dispersion with Stacking Parameters

As a fundamental result from fitting the stacked spectra, we obtain measurements of H I and CO velocity dispersions as a function of stacking parameter. These results are shown in Figure 2.4 for NGC 6946. Equivalent plots for the remaining galaxies are shown in Figures 2.6 – 2.11.

The top panel shows the variation of $\sigma_{\rm HI}$ and $\sigma_{\rm CO}$ with galactocentric radius. Over large parts of the disks probed here ($R \lesssim R_{25}$), the velocity dispersion of both H I and CO are roughly constant (ratio of ~ 1) and have typical values within $7 - 21\,{\rm km\,s^{-1}}$. The largest ranges in velocity dispersion are present near galaxy centers ($R \lesssim 0.2\,R_{25}$) where the largest velocity dispersion values are found, likely a signature of large velocity gradients inside our $\sim 500\,{\rm pc}$ beam caused, for example, by molecular bars. However, most of these points are excluded in our analysis due to double-peaked spectral profiles (Section 2.1). The error bars represent the statistical uncertainties in the velocity dispersion determination due to the number of stacked spectra and observational noise (Section 2.2.3.5). In Table 2.5 we show the values of the H I and CO velocity dispersions as a function of galactocentric distance given for each galaxy.

The other panels in Fig. 2.4 show the variation of velocity dispersion when stacking by SFR surface density, H I surface density, H_2 surface density, and total gas surface density, respectively. To first order, we do not observe a clear general trend of the velocity dispersions with any of

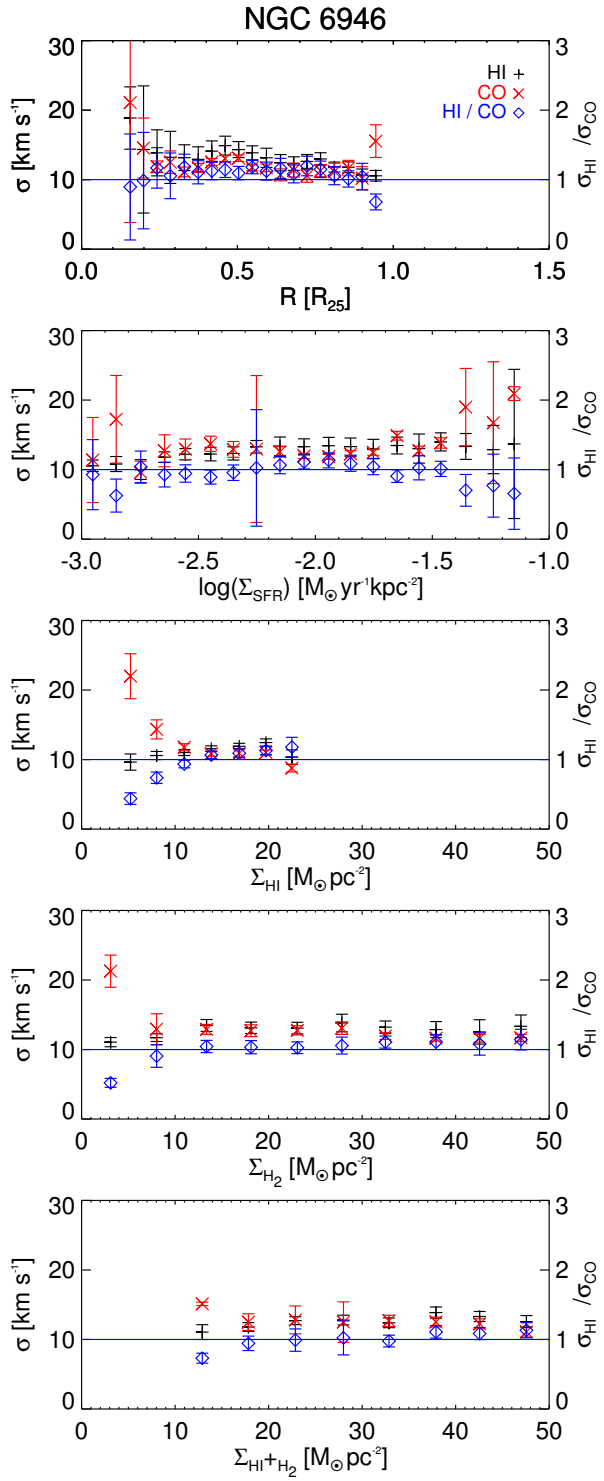

Figure 2.4 **NGC 6946: Trends of velocity dispersion with different stacking parameters.** From top to bottom we show results for stacking by galactocentric radius, and surface density of SFR, H I, H_2, and total gas (different x-axes). The left y-axis gives the velocity dispersion, the right y-axis their ratio $\sigma_{\rm HI}$ / $\sigma_{\rm CO}$. Black plus signs represent H I, red crosses CO, and blue diamonds represent the ratio of $\sigma_{\rm HI}$ / $\sigma_{\rm CO}$. Error bars represent statistical uncertainties. The blue horizontal line indicates a value of unity for the ratio (right y-axis). For the other galaxies see Figures 2.6 – 2.11 at the end of the Chapter.

Table 2.2. Spearman's Rank Correlation Coefficients for the complete sample of galaxies

	R_{25}	Σ_{SFR}	Σ_{HI}	Σ_{CO}	$\Sigma_{HI}+\Sigma_{CO}$
σ_{HI}	-0.6 ± 0.5	0.9 ± 0.3	0.6 ± 0.6	0.3 ± 0.5	0.6 ± 0.5
σ_{CO}	-0.5 ± 0.4	0.5 ± 0.6	-0.8 ± 0.4	0.2 ± 0.6	-0.2 ± 0.6
σ_{HI}/σ_{CO}	0.3 ± 0.3	0.0 ± 0.5	1.0 ± 0.3	0.0 ± 0.5	0.6 ± 0.4

Table 2.3. Median values of the velocity dispersions measured in the whole sample of galaxies

H I [km s^{-1}]	CO [km s^{-1}]	H I / CO
11.9 ± 3.1	12.0 ± 3.9	1.0 ± 0.2

these parameters. To quantify this assertion, we calculate the Spearman's rank correlation coefficients for each galaxy and for each stacking parameter. That is, for each galaxy we calculate the coefficients for σ_{HI}, σ_{CO}, and σ_{HI}/σ_{CO} for each of the five different stacking parameters: R_{25}, Σ_{SFR}, Σ_{HI}, Σ_{H2}, Σ_{HI+H2}. We present the median values of these coefficients in Table2.2, together with their 1σ range. Values of ± 1 indicate clear correlations, whereas values closer to 0 signify no correlation.

Naively, we would have expected a strong correlation between SFR surface density and velocity dispersion. This is because young massive stars are thought to be important contributors in driving turbulence and injecting energy into the ISM. The galaxies in our sample show different behaviors: while for seven galaxies the velocity dispersions are roughly constant with SFR surface density, for the remaining five (NGC 2903, NGC 3351, NGC 4736, NGC 5055, and NGC 6946) there is an increase of velocity dispersion with increasing SFR surface density. The increase in velocity dispersion goes from $\sim 30\% - \sim 60\%$. However, the true effect of SFR surface density on velocity dispersion remains inconclusive, as these two parameters vary most strongly with radius. Thus, there could be an additional radially varying effect that may explain the observed trends (e.g., shear due to differential rotation).

We find a similar result when stacking by H I, H_2, and total gas surface densities. The measured velocity dispersions do not present a strong correlation with any of these stacking parameters, except again for NGC 5055.

The trends for individual galaxies and for different stacking parameters are shown in Figures 2.4 and 2.7 – 2.11. Here, we summarize the trends for our entire sample as histograms in left panels of Figure 2.5 where we only include bins between 0.2 and 1 R_{25} (Section 2.2.3.4). We find the H I and CO velocity dispersions to have a range of $\sim 7 - 21$ km s^{-1}. The histograms for the ratio of H I to CO velocity dispersions are shown in the right panel of Figure 2.5. Regardless of the stacking parameter, we find the ratio to remain surprisingly constant at an average value of 1.0 ± 0.2. We summarize the median velocity dispersion values for our sample in Table 2.3.

2.3.2 Comparison to Previous Measurements of Velocity Dispersions

A number of studies have been done in the past to constrain the H I and CO velocity dispersions. The most straightforward comparison of our H I velocity dispersions is the work done by Tamburro et al. (2009) as they analyze the same data (from THINGS). They find that the velocity dispersion decreases with increasing radial distance from the galaxy center out to $\sim 4\,R_{25}$. Their method is to take the second moment value as a measure of the velocity dispersion regardless of the shape of the spectrum. We note that this can lead to an overestimate of the real velocity dispersions in regions were bulk motions are important, e.g., at stellar bars. Restricting their sample to the radial range covered by our analysis ($0.2 - 1\,R_{25}$), we find comparable velocity dispersions which are to first order constant (NGC 628, NGC 3184, NGC 3351, NGC 4736, NGC 5055, NGC 5194, and NGC 6946). Only for a subset of our sample (NGC 925, NGC 2903, NGC 4736, NGC 5055, and NGC 5194) we find a slight decrease of velocity dispersions with radius. It is important to note that we do not doubt that the velocity dispersions decrease at large galactocentric radii, e.g., the general conclusion of Tamburro et al. (2009). We solely state that within the optical disk where both H I and CO emission is strong we find no significant radial trends.

Only a few measurements of CO velocity dispersions in other galaxies have been published so far. We summarize these together with our measurements in Table 2.4. Wilson et al. (2011) carried out a study of the CO (3 – 2) line in 12 nearby galaxies with the JCMT single-dish telescope. They measure values for the CO velocity dispersion in the range of $4 - 20$ km s^{-1}. For the five galaxies that overlap with our sample we list the average velocity dispersion measurements also in Table 2.4. While both studies find no clear signature of a radial trend, the velocity dispersion values by Wilson et al. (2011) are in general $\sim 40\%$ smaller than our measurements. It is not immediately clear if this (apparent) discrepancy relates to a true difference in velocity dispersions for CO (2 – 1) and CO (3 – 2) gas disks or if it relates to the limited signal-to-noise in the JCMT data. Combes & Becquaert (1997) studied the two nearly face-on galaxies NGC 628 and

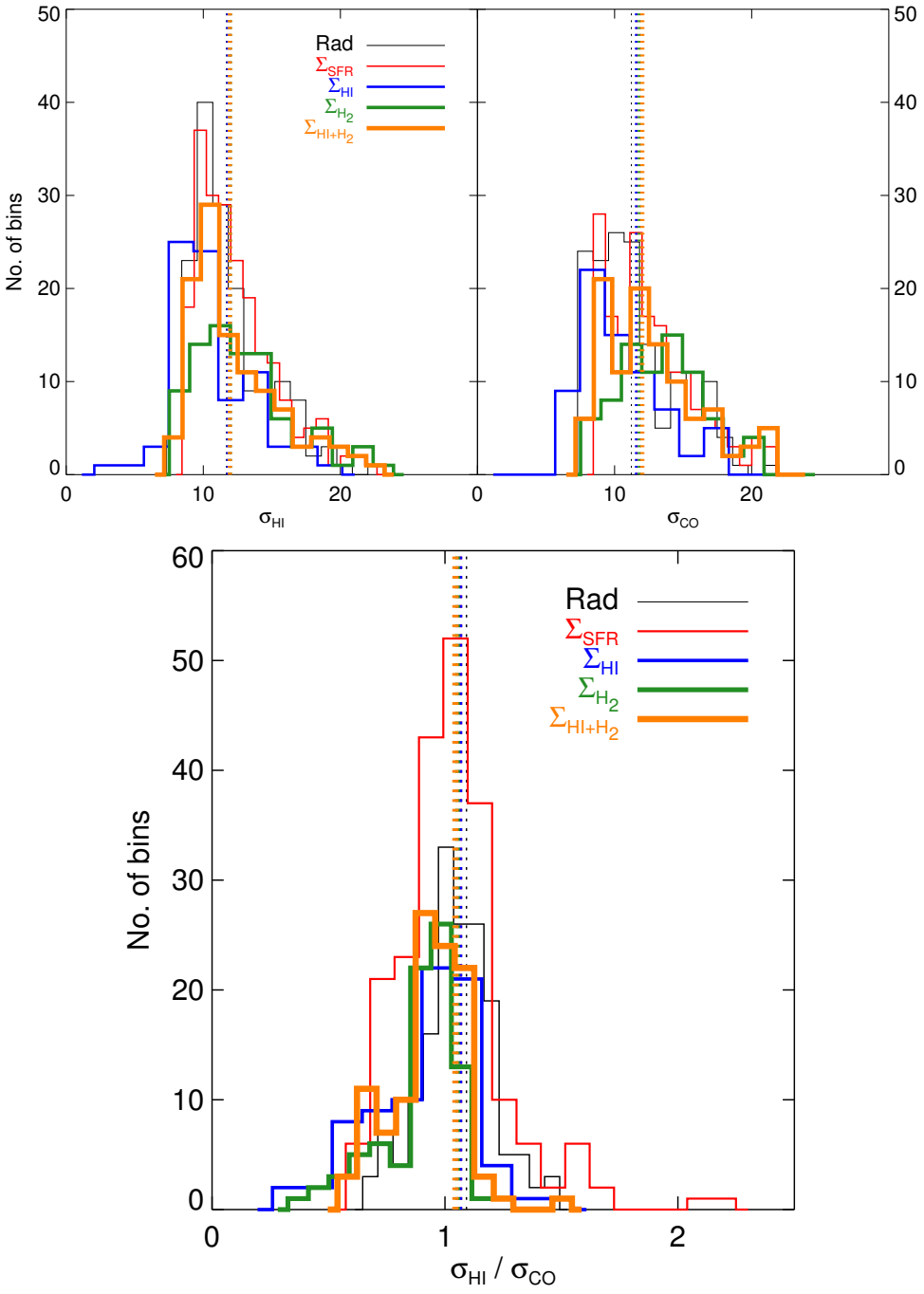

Figure 2.5 **Histograms of velocity dispersions of the whole sample of galaxies.** Histograms of the $\sigma_{\rm HI}$ and $\sigma_{\rm CO}$ (left two panels) for each stacking parameter and their ratio $\sigma_{\rm HI}$ / $\sigma_{\rm CO}$ (right panel). Shown by the black thin lines are histograms of data stacked by galactocentric radius, in the red thicker lines stacked by SFR surface density, in the blue thicker lines by H I surface density, in the green thicker lines for H_2 surface density, and in the orange and thickest lines by total neutral gas surface density. The dashed lines show the median values obtained for the different stacking parameters (same color coding as with the histograms).

Table 2.4. Comparison of CO Velocity Dispersions

Galaxy	This work [km s^{-1}]	Lit. [km s^{-1}]	Lit. transition	Beam size [arcsec]	ΔR [R_{25}]	Ref.
NGC 628	8.7 ± 0.6	6.5 ± 2.5	**2 – 1**, 1 – 0	12, 23	0 – 0.34	Combes & Becquaert (1997)
NGC 5194	16.4 ± 1.1	17.0 ± 3.3	1 – 0	22	0.2 – 0.43	Pety et al. (2013)
NGC 628	8.8 ± 0.6	4.1 ± 2.5			0 – 0.5	
NGC 2403	11.7 ± 2.9	5.2 ± 4.9			0 – 0.45	
NGC 3184	9.8 ± 1.8	6.8 ± 5.9	3 – 2	14.5	0 – 0.65	Wilson et al. (2011)
NGC 4736	17.7 ± 1.3	12.0 ± 9.0			0 – 0.3	
NGC 5055	15.2 ± 4.2	9.4 ± 6.6			0 – 0.55	

NGC 3938 and found similar H I and CO vertical velocity dispersions in selected lines-of-sight as we do in our study.

Most recently, the molecular gas of M 51 was mapped with high sensitivity by the PAWS survey (Schinnerer et al. 2013) and velocity dispersions were studied by Pety et al. (2013). They compared CO single-dish measurements from the IRAM 30 m telescope with interferometric observations taken with PdBI. The velocity dispersions they measure with interferometric-only data are ∼ 50% lower than the ones measured with the single-dish telescope. Their single-dish measurements are comparable to the results we obtain. They interpret this difference in velocity dispersions as evidence of a high-dispersion diffuse CO component, in addition to the clumpy molecular disk.

2.3.3 Multi-component Phase Structure

As stated in Chapter 1, the ISM does not have sharp boundaries between its different phases. There is a natural transition from atomic to molecular gas, where the highest densities and lowest temperatures are reached. The two-phase model for the neutral atomic gas (Wolfire et al. 2003; Field et al. 1969) differentiates between the WNM (broad component) and CNM (narrow component), both contributing to the total H I emission. However, there is also an unstable phase which may account for up to 50% of the H I mass. In a simple picture, the thermal broadening of the warm neutral H I medium at a temperature of 8000 K leads to a velocity dispersion of ∼ 8 km s^{-1}. We measure values for σ_{HI} in the range of 7 – 21 km s^{-1}, with a median value of 11.9 km s^{-1} and a mean of 12.7 km s^{-1} with a 1σ dispersion of 3.1 km s^{-1}. Within the uncertainties this is consistent with the presence of only an 'undisturbed' WNM, but there is likely additional broadening present due to non-thermal gas motions.

On the contrary, in the usually accepted picture one would expect much smaller velocity dispersions for the cold molecular gas phase. Here, the clouds are thought to be few 10 pc in size and have observed velocity dispersions of 2 – 5 km s^{-1} (McKee & Ostriker 2007; Bolatto et al. 2008). The velocity dispersions measured by us exceed this value by a wide margin: we measure values for σ_{CO} ranging within 6.7 – 23 km s^{-1}with an average mean value of 12.8 km s^{-1} with a 1σ dispersion of 3.9 km s^{-1}, very close to what we measure for the H I. These values are much larger than the values expected by purely thermal processes ($\sigma \sim 0.1$ km s^{-1} for 10 K gas) and are also larger than those expected by intra-cloud motions, which in M 31 are ~ 6 km s^{-1} (Schruba et al., in prep.). At the resolution we are working, we cannot reject the possibility that part of the dispersion we are measuring could be due to bulk motions unresolved by the velocity maps at 11 arcsec (the native natural-weighted THINGS resolution). However, this would affect both H I and CO measurements.

Our main result is a rough agreement of the velocity dispersions for both H I and CO components. This is in agreement with Combes & Becquaert (1997) that studied NGC 628 and NGC 3938. Based on their measurements they argue that: "The similarity of the CO and H I dispersions suggests that the two components are well mixed, and are only two different phases of the same kinematical gas component" – an interpretation that could also apply to our measurements.

As mentioned in the Introduction, the observed velocity dispersions of galaxies with large scale disk morphology can be related to the vertical density profile of the observed tracer. The density profile, set by hydrostatic equilibrium, results from the balance between gravitational weight and gas pressure, i.e., its velocity dispersion. For the general case of a multi-component stellar and gaseous disk the vertical density profile of each component needs to balance the combined gravitational field of stars, gas, and dark matter. Useful approximations to the full numerical solution are given by Elmegreen (1989); Narayan & Jog (2002). In general, an increase of velocity dispersion causes an increase in scale height at fixed gravitational field (i.e., surface density) while an increase in surface density decreases the scale height at fixed velocity dispersion. The hydrostatic equilibrium assumption also let us link the observables for face-on galaxies (i.e., velocity dispersion) and edge-on galaxies (i.e., scale height).

Evidence for a thick molecular gas disk in nearby galaxies has been presented in several studies. As highlighted in the Introduction, early observations of the edge-on galaxy NGC 891 revealed the presence of an extended CO component (Garcia-Burillo et al. 1992), which has in the meanwhile been confirmed by deeper and more extended maps of the galaxy (Garcia-Burillo et al., priv. comm.). A massive extraplanar reservoir of molecular gas has also been reported in the highly inclined galaxy M 82 (Walter et al. 2002), though this material has likely been expelled from the disk by the intense star formation activity and thus may not be in hydrostatic balance.

A complementary method to infer the vertical disk structure has been performed by Combes et al. (2012). They analyzed the power spectra of gas and infrared emission in M 33 and observed a break in the power spectrum pointing to the transition from 2D to 3D turbulence suggestively tracing the disk scale height. They detect a thick disk for both H I and CO of comparable height.

Nevertheless observational evidence is scarce to date, and in some cases circumstantial, as it is impossible to directly measure the vertical dispersion of the CO gas (requiring face-on orientation) and the thickness of a CO disk (edge-on orientation) in the same system.

Observationally disentangling the thickness of the atomic and molecular gas disk in our own Galaxy is difficult given our in-disk viewing position and severe distance ambiguities. Furthermore, prominent structures are known that extend far away from the galactic plane such as the Goult's Belt and the Taurus-Perseus-Auriga association. Employing large-scale CO mapping, Dame & Thaddeus (1994) found evidence for a homogeneous thick molecular disk ~ 3 times more extended than the (well known) thin disk and comprising at least 5% of the entire CO luminosity. However, as mm single-dish observations need to perform 'differential' measurements to subtract atmospheric emission, they are largely insensitive to any extended emission and leave the true mass of a diffuse gas component largly unconstrained. In addition, a number of high-latitude clouds are known in the literature (e.g., Magnani et al. 1985, 1996) though at least some of them are from extragalactic origin and thus will not be in hydrostatic balance.

Estimates for external galaxies go as far as they may contain a diffuse medium that accounts for $\sim 30\% - 50\%$ of the molecular mass as suggested by (Garcia-Burillo et al. 1992; Pety et al. 2013), however, additional observations would be required to assert a general validity.

2.3.4 Implications

With the current data it is hard to estimate how much of the observed luminosity emerges from a thin versus a thick disk component. However, it is clear that the contribution (in flux) from the thick component must be significant, of order $\sim 30\%$, in order to be detectable. We can only speculate what fraction of the molecular mass would be entrained in such a thick component: the conditions of the gas (gas temperature, radiation field, and resulting gas excitation) will likely be significantly different compared to the GMC environment in the star-forming disk. This has two very direct implications. The first one is the importance of quantifying how much the $X_{\rm CO}$ conversion factor varies between dense and diffuse molecular gas. It is not clear yet whether these different environments would necessarily lead to a difference in the conversion factor. A recent study of the high-latitude cloud MBM 40 gave a conversion factor for this cloud which is consistent with the Galactic one (Cotten & Magnani 2013). Dame et al. (2001) and Liszt et al. (2010) find something similar, as they conclude that $X_{\rm CO}$ shows little variation with latitude

from the galactic value, however, they note that further studies should be conducted to reach a more definite answer on this issue. The second is that if a significant fraction (of order 30%) of the CO line flux was indeed due to a component that is not coincident with the star-forming disk, then previous studies would have overestimated the flux that is co-spatial with ongoing star formation. This would imply that the derived molecular gas masses would have to be decreased by a similar factor. Shetty et al. (2013) investigated the SFR-CO relation in the STING sample finding indications of a sub-linearity for 8 them. One possible interpretation they give is that there might be "excited CO in the diffuse or non-star-forming ISM". Future observations using both interferometers and single-dish telescopes are needed to clearly separate the relative flux contribution of a diffuse versus a compact molecular gas phase in nearby galaxies.

It is also noteworthy that CO appears to be able to survive in environments that are significantly different than those found near the star-forming disk, i.e., at significantly lower extinction and resulting shielding. The existence of a substantial thick molecular disk also challenges various models of H_2 formation. This includes models that rely on Parker instability (i.e., colliding flows and flows along magnetic field lines), as in those models dense gas settles near the galactic mid-plane forming a thin disk. On the other hand, models assuming gravitational collapse as means of dense molecular gas formation do not face these issues (McKee & Ostriker 2007).

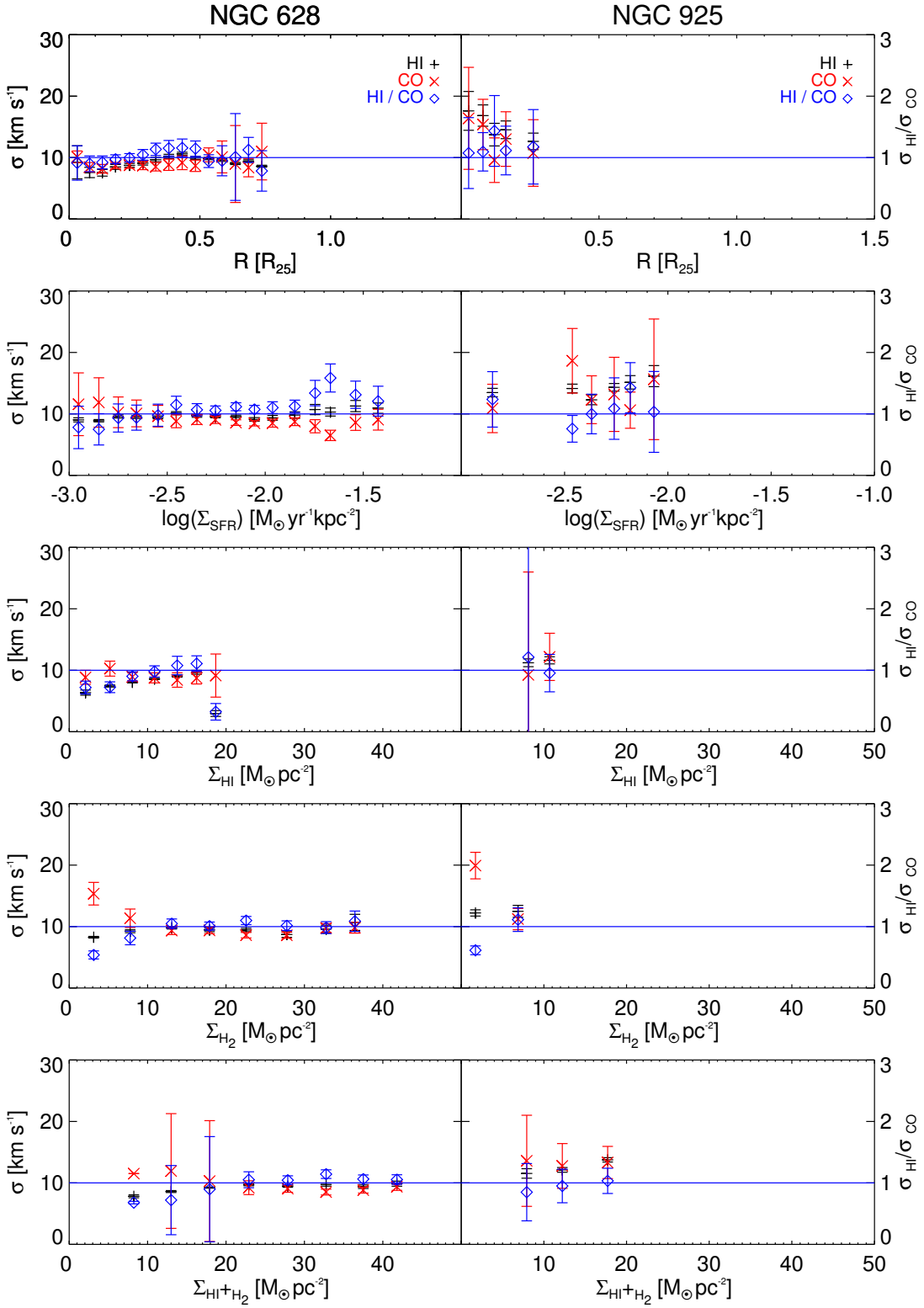

Figure 2.6 **Trends of velocity dispersion with different stacking parameters.** From top to bottom we show results for stacking by galactocentric radius, and surface density of SFR, H I, H_2, and total gas (different x-axes). The left y-axis gives the velocity dispersion, the right y-axis their ratio $\sigma_{\rm HI}$ / $\sigma_{\rm CO}$. Black plus signs represent H I, red crosses CO, and blue diamonds represent the ratio of $\sigma_{\rm HI}$ / $\sigma_{\rm CO}$. Error bars represent statistical uncertainties. The blue horizontal line indicates a value of unity for the ratio (right y-axis).

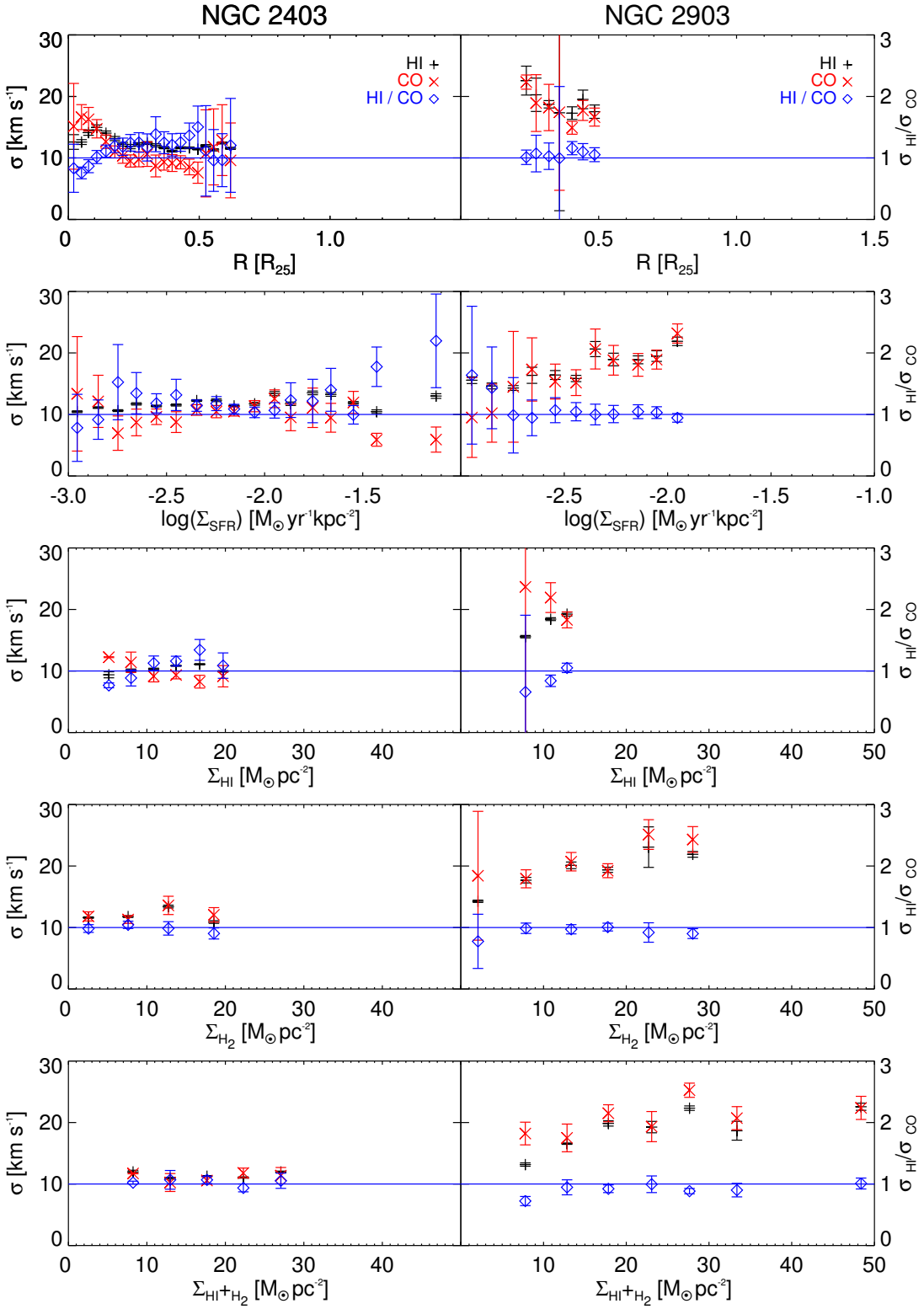

Figure 2.7 Same as in Fig. 2.7, but for NGC 2403 (left panel) and NGC 2903 (right panel).

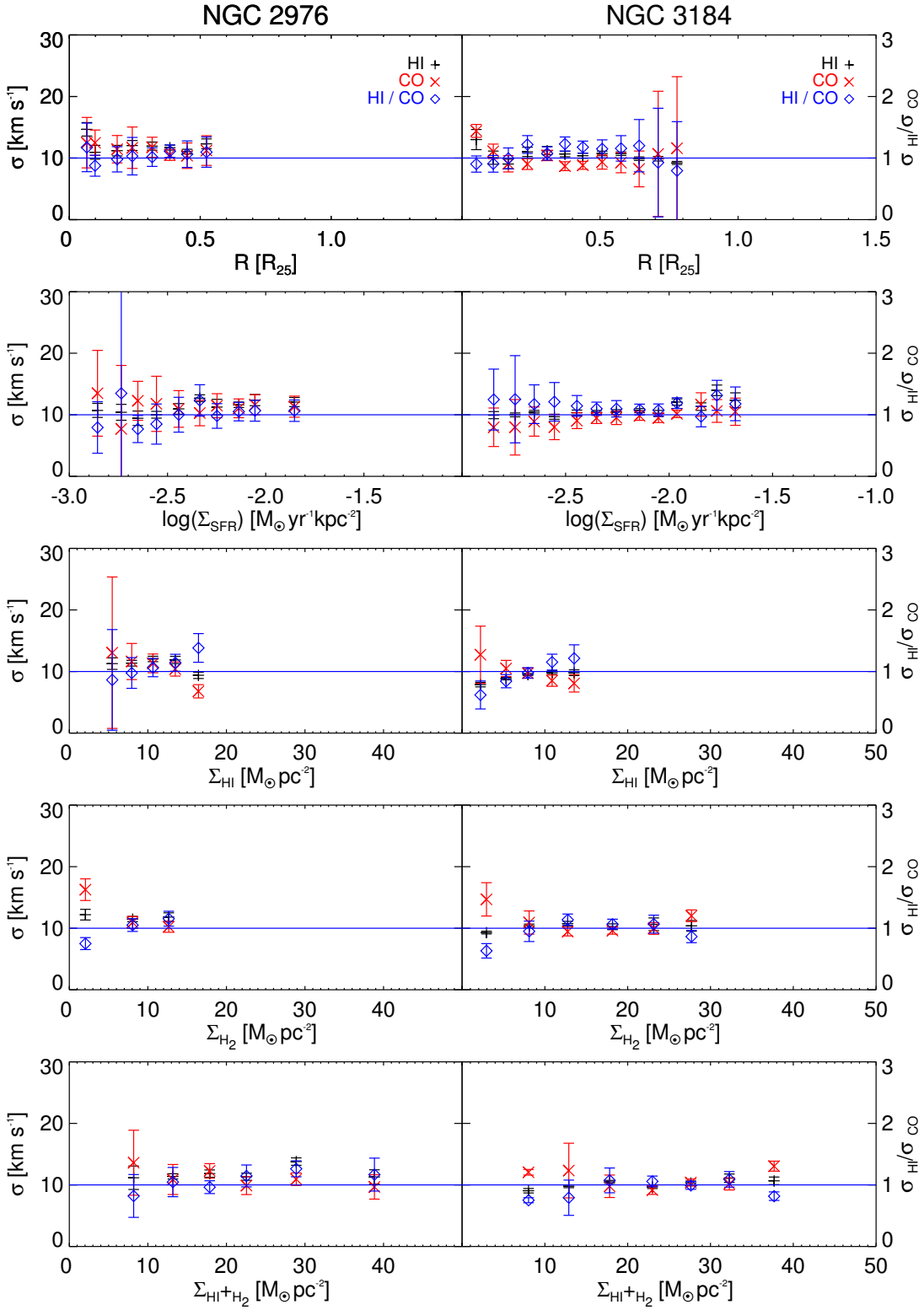

Figure 2.8 Same as in Fig. 2.7, but for NGC 2976 (left panel) and NGC 3184 (right panel).

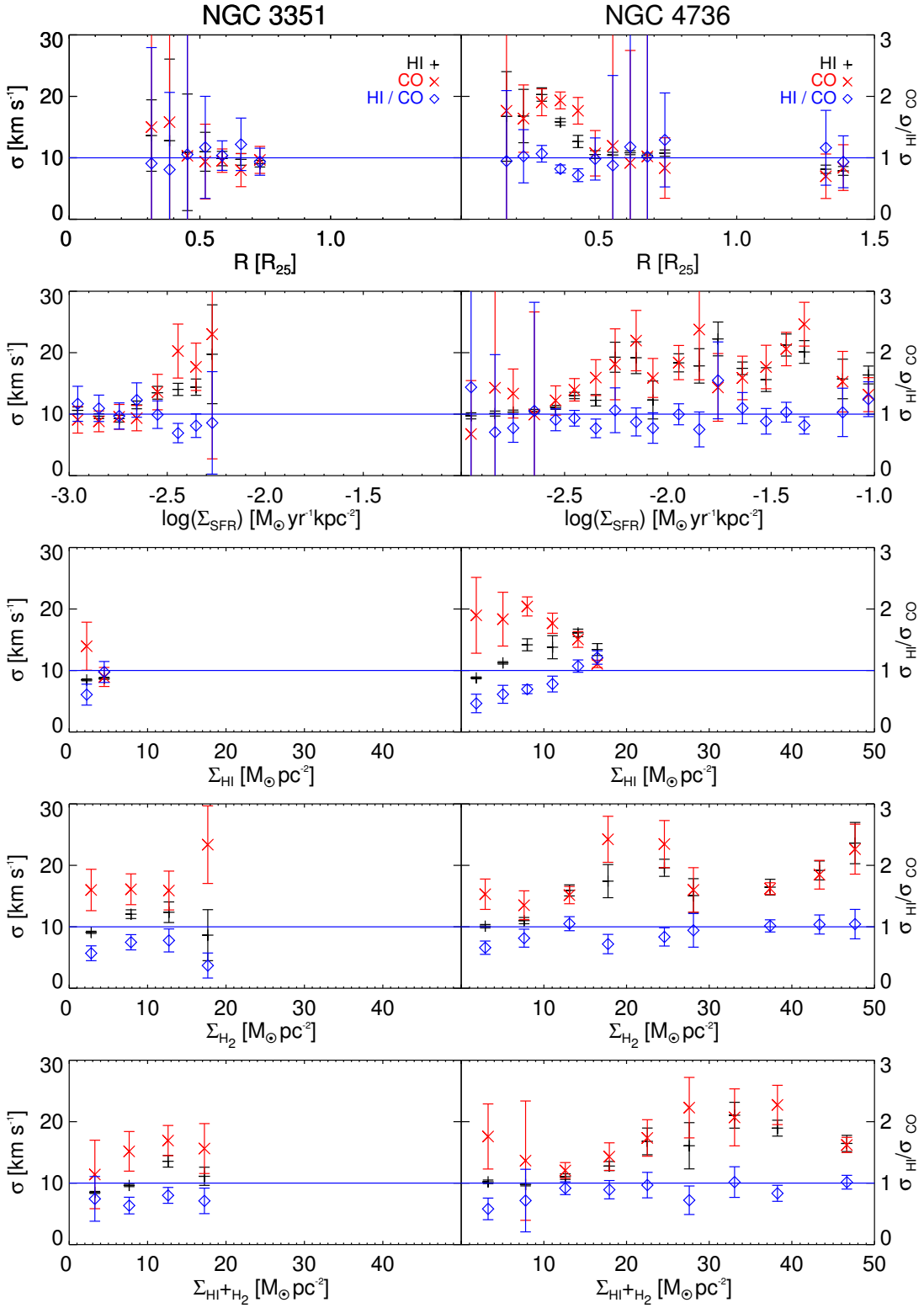

Figure 2.9 Same as in Fig. 2.7, but for NGC 3351 (left panel) and NGC 4736 (right panel).

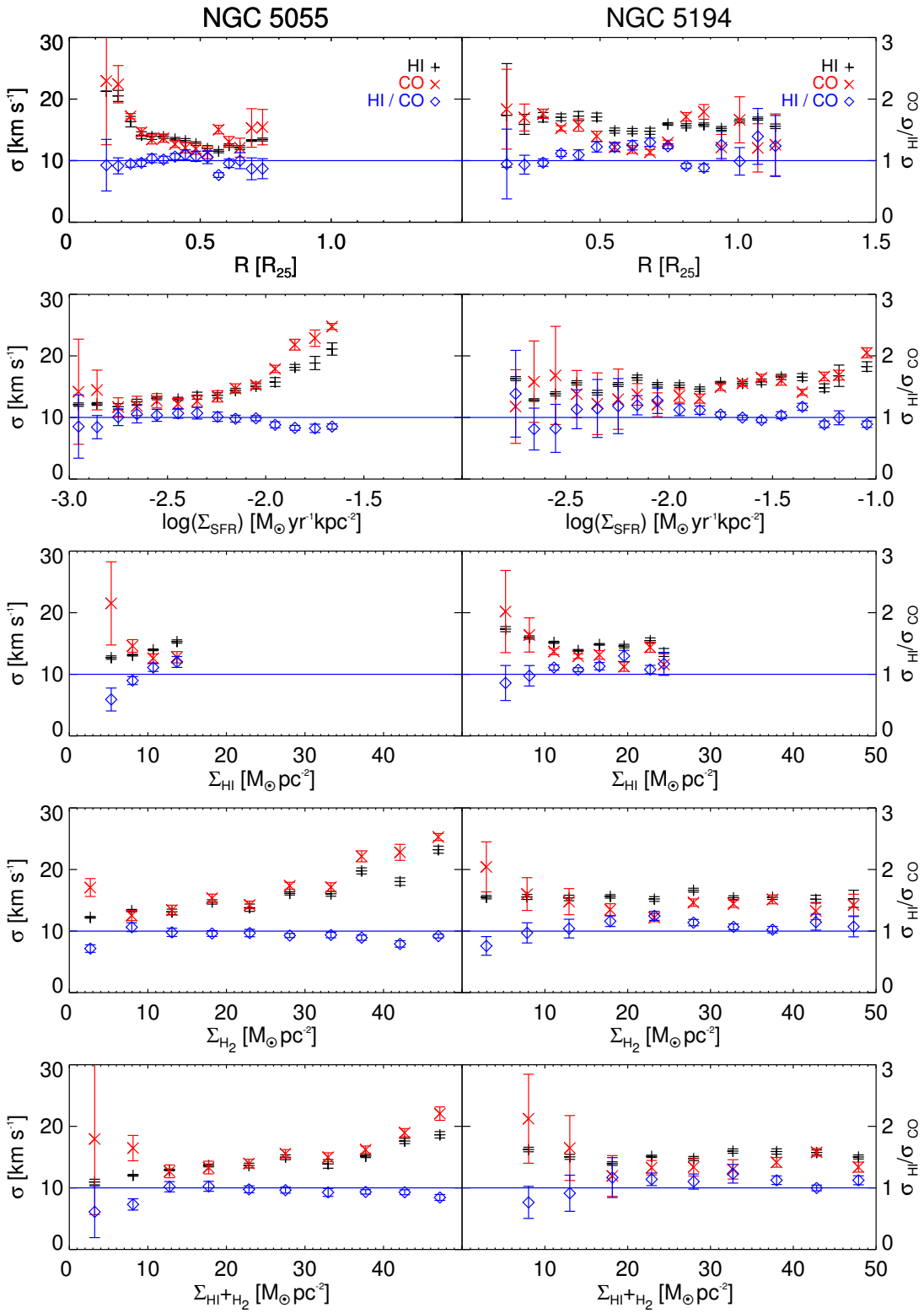

Figure 2.10 Same as in Fig. 2.7, but for NGC 5055 (left panel) and NGC 5194 (right panel).

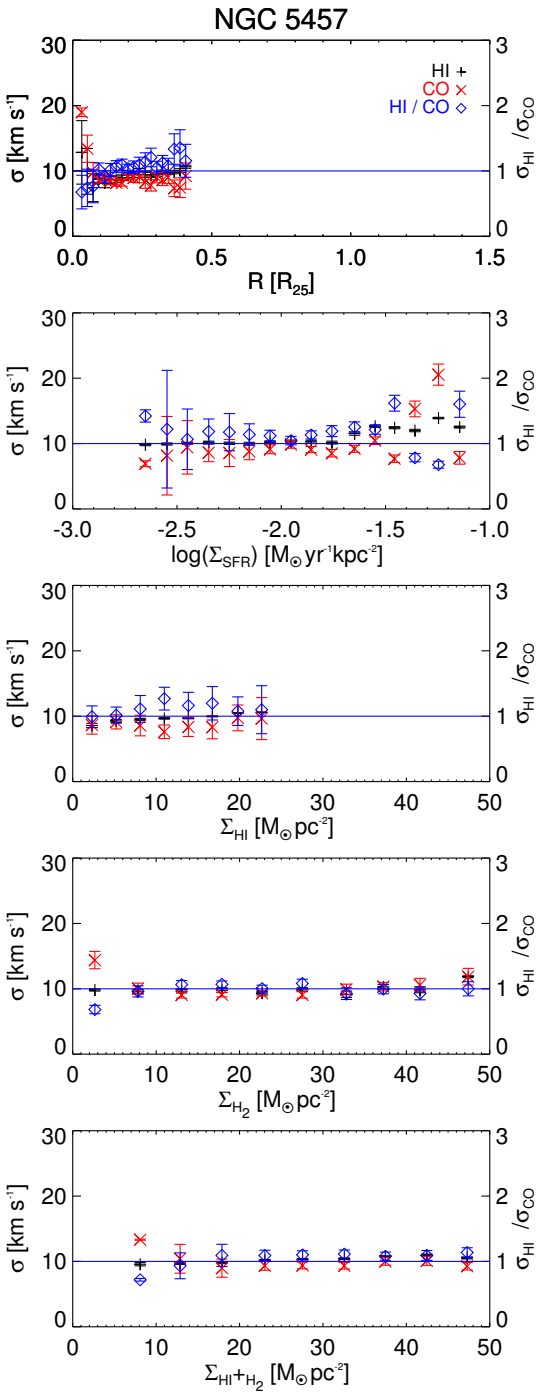

Figure 2.11 Same as in Fig. 2.7, but for NGC 5457.

Table 2.5. H I and CO velocity dispersions as a function of galactocentric distance

Galaxy	R [R_{25}]	σ_{HI} [km s^{-1}]	σ_{CO} [km s^{-1}]	σ_{HI}/σ_{CO}
NGC 628	0.03	9.2	10.1	0.9
	0.08	7.6	8.4	0.9
	0.13	7.5	8.2	0.9
	0.18	8.5	8.7	1.0
	0.23	8.7	8.8	1.0
	0.28	9.1	8.7	1.0
	0.33	9.7	8.5	1.1
	0.38	10.2	8.8	1.2
	0.43	10.6	9.2	1.2
	0.48	9.9	8.7	1.1
	0.53	9.8	10.4	0.9
	0.58	9.6	10.1	0.9
	0.64	9.0	9.0	1.0
	0.69	9.4	8.4	1.1
	0.74	8.6	11.0	0.8
NGC 925	0.03	17.6	16.4	1.1
	0.08	16.8	15.4	1.1
	0.12	13.7	9.6	1.4
	0.16	14.5	13.0	1.1
	0.26	12.6	10.8	1.2
NGC 2403	0.02	12.3	15.3	0.8
	0.05	12.0	16.4	0.7
	0.08	12.4	14.2	0.9
	0.11	12.4	11.1	1.1
	0.14	12.2	9.9	1.2
	0.18	12.2	10.3	1.2
	0.21	12.1	9.1	1.3
	0.24	11.1	8.8	1.3
	0.27	10.7	9.1	1.2
	0.30	11.2	9.4	1.2
	0.33	10.6	8.2	1.3
	0.37	10.7	7.6	1.4
	0.40	10.5	8.4	1.2
	0.43	10.8	8.7	1.2
	0.46	10.6	8.3	1.3
	0.50	10.3	6.7	1.5
	0.53	10.8	9.6	1.1
	0.56	10.2	9.8	1.0
	0.59	10.8	7.6	1.4
	0.62	10.8	7.2	1.5
	0.68	9.7	12.2	0.8
NGC 2903	0.24	20.8	18.7	1.1
	0.27	19.2	17.4	1.1
	0.32	17.3	15.7	1.1
	0.36	15.4	15.0	1.0
	0.40	15.0	12.7	1.2
	0.44	16.5	16.3	1.0
	0.49	15.8	15.3	1.0
NGC 2976	0.07	14.7	12.2	1.2
	0.10	10.5	12.3	0.9
	0.18	10.8	10.5	1.0
	0.24	11.4	9.6	1.2
	0.32	11.6	11.2	1.0
	0.38	11.2	10.3	1.1
	0.45	10.2	10.2	1.0
	0.52	10.7	11.2	1.0
NGC 3184	0.05	13.0	14.4	0.9
	0.11	10.1	11.1	0.9
	0.17	9.0	9.1	1.0
	0.24	11.0	9.0	1.2
	0.31	11.2	10.4	1.1
	0.37	10.7	8.7	1.2
	0.44	10.4	8.8	1.2
	0.51	10.7	9.4	1.1
	0.58	10.7	9.3	1.2
	0.64	9.9	8.2	1.2
	0.71	9.9	10.7	0.9
	0.78	9.2	11.6	0.8
NGC 3351	0.31	13.6	15.0	0.9
	0.38	12.8	15.8	0.8
	0.45	10.9	10.3	1.1
	0.52	11.0	9.4	1.2
	0.59	9.9	9.5	1.0
	0.66	9.7	8.0	1.2
	0.73	9.0	9.7	0.9

Table 2.5 (cont'd)

Galaxy	R [R_{25}]	σ_{HI} [km s^{-1}]	σ_{CO} [km s^{-1}]	σ_{HI}/σ_{CO}
NGC 4736	0.16	16.7	17.7	0.9
	0.23	16.8	16.4	1.0
	0.29	20.3	19.0	1.1
	0.36	15.8	19.3	0.8
	0.42	12.7	17.7	0.7
	0.49	10.5	10.7	1.0
	0.55	10.5	11.9	0.9
	0.61	10.8	9.2	1.2
	0.68	10.4	10.2	1.0
	0.74	10.8	8.3	1.3
	1.32	8.1	7.0	1.2
	1.39	7.9	8.4	0.9
NGC 5055	0.11	19.1	23.1	0.8
	0.14	17.1	18.9	0.9
	0.19	17.0	19.1	0.9
	0.23	14.6	15.5	0.9
	0.28	12.9	13.2	1.0
	0.32	13.0	12.8	1.0
	0.36	12.8	12.5	1.0
	0.40	12.4	12.2	1.0
	0.44	11.8	10.9	1.1
	0.48	11.4	11.2	1.0
	0.53	11.3	10.7	1.1
	0.57	11.0	13.6	0.8
	0.61	11.6	11.8	1.0
	0.65	11.0	12.2	0.9
	0.70	11.1	12.9	0.9
	0.74	11.5	14.5	0.8
	0.78	12.3	17.4	0.7
NGC 5194	0.16	17.4	18.4	0.9
	0.23	15.9	17.0	0.9
	0.29	17.0	17.6	1.0
	0.36	17.0	15.2	1.1
	0.42	17.2	15.8	1.1
	0.49	17.1	14.0	1.2
	0.55	14.9	12.2	1.2
	0.62	14.8	11.8	1.3
	0.68	14.8	11.4	1.3
	0.75	15.9	12.9	1.2
	0.81	15.7	17.1	0.9
	0.88	15.8	17.9	0.9
	0.94	15.2	12.1	1.3
	1.01	16.4	16.6	1.0
	1.07	16.8	12.1	1.4
	1.14	15.6	12.6	1.2
NGC 5457	0.03	12.8	19.0	0.7
	0.05	9.9	13.4	0.7
	0.07	7.4	9.7	0.8
	0.09	8.8	8.6	1.0
	0.12	8.2	9.0	0.9
	0.14	8.7	8.5	1.0
	0.16	8.7	8.2	1.1
	0.18	9.0	8.2	1.1
	0.20	9.4	9.0	1.0
	0.22	9.5	8.9	1.1
	0.24	9.9	9.0	1.1
	0.26	9.5	8.3	1.1
	0.28	9.4	7.8	1.2
	0.30	9.4	9.0	1.1
	0.32	9.7	8.6	1.1
	0.34	9.7	9.0	1.1
	0.37	9.8	7.4	1.3
	0.39	10.1	7.4	1.4
	0.41	10.6	9.2	1.2
NGC 6946	0.16	18.9	21.1	0.9
	0.20	14.3	14.5	1.0
	0.24	13.9	11.9	1.2
	0.28	13.2	12.5	1.1
	0.33	13.2	11.1	1.2
	0.37	12.9	11.7	1.1
	0.42	14.1	12.5	1.1
	0.46	14.9	13.0	1.1
	0.50	14.3	13.1	1.1
	0.55	13.9	11.7	1.2
	0.59	13.1	11.7	1.1
	0.64	12.4	10.7	1.2
	0.68	12.3	11.4	1.1
	0.72	12.6	10.6	1.2
	0.77	13.0	11.3	1.1
	0.81	11.8	11.2	1.1
	0.86	11.8	11.7	1.0
	0.90	10.7	10.2	1.0
	0.94	10.6	15.5	0.7

CHAPTER 3

Molecular Gas: Single-dish vs. Interferometric Observations[†]

The results obtained in the first project point to the existence of a CO component that is giving rise to larger velocity dispersions, as compared to what is measured within molecular clouds. Based on this result, we investigate the possibility of the existence of two phases of molecular gas. As mentioned in the Introduction, molecular gas can be observed through CO emission, which can be mapped both with single-dish telescopes and with interferometers. Single-dish telescopes, especially after the development of multi-beam heterodyne receiver arrays, provide a large instantaneous field of view and good sensitivity, although at limited spatial resolution. Interferometers, on the other hand, provide higher spatial resolution, with the drawback that not all spatial scales can be recovered (Section 1.5). The largest spatial scale to which an interferometer is sensitive is determined by the shortest baselines (i.e., the closest projected distance between two individual telescopes in the plane perpendicular to the line of sight (LOS)). Thus, any emission arising from structures larger than this spatial scale is "invisible" to the interferometer. If most of the gas inside galaxies were distributed in structures (e.g., molecular clouds) that are smaller than this largest spatial scale (and that are separated from each other by at least the synthesized beam size), then either instrument would detect the same gas component, only with different spatial resolution. However, if there a significant amount of gas is distributed in large scale structures, the interferometer and single-dish measurements would yield different results. The flux recovered by the interferometer therefore depends on the gas distribution and the molec-

[†]This chapter is adapted from Caldú-Primo et al. (2015)

ular cloud spatial scales present in the observed galaxy as compared to the specific resolution of the interferometer's configuration[1].

Pety et al. (2013) conducted a study of the molecular gas phase as traced by the CO (1 – 0) emission in M 51. They used single-dish IRAM 30 m data, Plateau de Bure Interferometer (PdBI) data, and a combination of both data sets, to compare flux recovery and velocity dispersions measured in these three data sets. They show that the interferometer recovers only (50 ± 10)% of the total flux, indicative of a molecular component that is missed by the interferometer. In addition, they found that the purely single-dish velocity dispersions are typically twice as large as the interferometric velocity dispersions. As stated before, molecular gas might be present in different cloud types, with different temperatures, densities, and spatial distributions. These different physical configurations would modify the expected velocity dispersions present in the gas. Thus, their result implies not only that ∼ 50% of the gas is missed by the interferometer, but that this gas gives rise to larger velocity dispersions compared to the velocity dispersions measured for the molecular gas (i.e., CO emission) inside the GMC sample (to which the interferometer is sensitive). This result could explain why we measure relatively large velocity dispersions in the molecular gas of the 12 nearby galaxies previously studied.

We deem it important to further investigate these two molecular components: one that is clumpy and organized as molecular clouds, and another one that is more diffuse and with higher velocity dispersion than the clumpy one. To do so, we want to compare CO line widths as measured from interferometric and single-dish observations, as well as the fluxes recovered in each case. Unfortunately, high-sensitivity interferometric maps of nearby galaxies are still very scarce, a situation that will, however, soon change with the advent of ALMA. Thus, we concentrate our current study on two galaxies: NGC 4736 and NGC 5055. We compare single-dish CO data from the HERACLES Survey (Leroy et al. 2009) and the "Nobeyama CO Atlas of Nearby Spiral Galaxies" (Kuno et al. 2007) to interferometric observations taken by La Vigne (2010) using the Combined Array for Research in Millimeterwave Astronomy (CARMA).

The chapter is organized as follows. In Section 3.1 we discuss the main characteristics of the employed data sets and the two galaxies studied. In Section 3.2 we discuss our methodology, to finally show the results in Section 3.3. A discussion is provided in Section 3.4.

[1] During the image deconvolution the flux recovery will also strongly depend on the noise properties (e.g., Helfer et al. 2002).

3.1 Data and Sample

In order to carry out the analysis, the data needs to meet three conditions: high sensitivity, a clear contrast between the scales recovered using the interferometer and using the single-dish, and available H I velocity maps. Even though there is a large survey, BIMA SONG (Helfer et al. 2003), in which the CO (1 – 0) molecular emission in nearby galaxies has been mapped with an interferometer, its sensitivity and resolution render it not suitable for this specific study. Therefore, we limit our study to the 2 galaxies for which high-sensitivity and resolution CARMA interferometric maps exist.

3.1.1 CO (1 – 0) Data

3.1.1.1 Interferometric Data

The interferometric CO data come from the CARMA interferometer. Both galaxies are mapped in the CO (1 – 0) line covering the inner $\sim 3'$ diameter of the targets via a 19 point mosaic. Observations were taken between 2007 January and 2008 July using the C, D, and E configurations, resulting in a synthesized beam size of $3.51 \times 2.97''$ for NGC 4736 and of $3.24 \times 2.81''$ for NGC 5055. The correlator was setup with two overlapping 62 MHz spectral windows to yield a spectral resolution of 1.95 MHz (or 5.08 km s^{-1} at 115 GHz)[2].

The CARMA data were calibrated using MIRIAD (Sault et al. 1995), weighted by noise variance, and robust weighting was applied. The data were cleaned down to a cutoff of 1.5 times the theoretical rms noise in each pixel using MOSSDI2, which performs a steer CLEAN on a mosaicked image (Steer et al. 1984). The images are primary-beam corrected. The flux scale was determined using observations of flux standards, including Uranus and Mars. In La Vigne (2010), a full description of the data reduction can be found. In their analysis they compare the CARMA observations with the BIMA SONG data (Helfer et al. 2003). After verifying the flux scales of both data sets they concluded that no flux rescaling was required. The rms noise sensitivity at 10 km s^{-1} resolution is 27 mJy beam^{-1} (237.5 mK)[3] for NGC 4736 and 19 mJy beam^{-1} (193.2 mK) for NGC 5055.

[2]The now publicly available data for NGC 4736 is at 10 km s^{-1} spectral resolution since the original data were unfortunately lost, and cannot be recovered.

[3]All sensitivities in K are stated using the beam size of the original data.

3.1.1.2 Single-dish Data

We also use single-dish CO (1 – 0) mapping from the "Nobeyama CO Atlas of Nearby Spiral Galaxies" (Kuno et al. 2007), which encompasses 40 nearby spiral galaxies at distances smaller than 25 Mpc. The observations were carried out with the Nobeyama 45 m telescope and typically cover most of the optical disk with a spatial resolution of 15″.

In the case of NGC 4736, the receiver used was BEARS, which consists of 25 beams (Sunada et al. 2000). In this case, digital spectrometers were used as backends. The total bandwidth and frequency resolution were 512 MHz and 605 kHz, which at 115 GHz correspond to 1331 km s^{-1} and 1.57 km s^{-1}, respectively.

In the case of NGC 5055, a four-beam SIS receiver was used, together with acousto-optical spectrometers used as backends. This configuration yields a frequency resolution and channel spacing of 250 kHz and 125 kHz, respectively, providing a total bandwidth of 250 MHz. At 115 GHz, this corresponds to a velocity resolution and velocity coverage of 0.65 km s^{-1} and 650 km s^{-1}, respectively.

In both cases, the spectra were then smoothed to 5 km s^{-1} (Nakai et al. 1994) as part of the data reduction. This is the spectral resolution of the data we use. At 10 km s^{-1} resolution, the rms noise sensitivity is 69 mJy beam^{-1} (28.3 mK) for NGC 4736 and 172 mJy beam^{-1} (70.7 mK) for NGC 5055.

3.1.2 CO (2 – 1) Single-dish Data

We use CO (2 – 1) data from the HERACLES survey (Leroy et al. 2009). This survey used the IRAM 30 m telescope to map molecular gas from 48 nearby galaxies inside the optical radius (R_{25}). This survey used HERA (a nine-beam dual-polarization heterodyne receiver array) together with the Wideband Line Multiple Autocorrelator (WILMA) backend. WILMA consists of 18 units of 2 MHz channel width each and 930 MHz bandwidth, yielding a velocity resolution of 2.6 km s^{-1} in a 1200 km s^{-1} velocity range at 230 GHz. The spatial resolution obtained at this frequency is 13″ after gridding. The rms noise sensitivity at 10 km s^{-1} is of 90 mJy beam^{-1} (11.5 mK) for NGC 4736 and 94 mJy beam^{-1} (12 mK) for NGC 5055.

3.1.3 H I Data

For our analysis we use H I intensity weighted velocity maps. These maps come from the THINGS survey (Walter et al. 2008). This survey encompasses 34 nearby galaxies at distances

of 2 – 15 Mpc. Observations of the two galaxies we analyze have high spectral (5.2 km s^{-1}) and spatial ($\sim 11''$ for natural weighting) resolutions.

3.1.4 Sample

As mentioned in the introduction, our sample is limited by the availability of sensitive, wide-field interferometric data sets. We thus focus on two galaxies only, NGC 4736 and NGC 5055. They have the following properties.

NGC 4736 is an isolated spiral galaxy of type SAab (Kennicutt et al. 2003). It is at a distance of 5.20 ± 0.43 Mpc (Tonry et al. 2001), has an inclination of 41° (de Blok et al. 2008), and an optical radius $R_{25} \approx 5$ arcmin (~ 7.5 kpc; Kennicutt et al. 2003).

NGC 5055 is a flocculent spiral galaxy classified as SAbc (Kennicutt et al. 2003). Its distance is 7.8 ± 2.3 Mpc (Masters 2005), its inclination is 59° (de Blok et al. 2008), and its optical radius is $R_{25} \approx 6$ arcmin (~ 13 kpc; Kennicutt et al. 2003).

More information on the galaxy properties can be found in Kennicutt et al. (2003), Walter et al. (2008), and Leroy et al. (2009). We show the integrated intensity CO maps of the three different surveys at a common resolution of 15″ in Figure 3.1.

3.2 Methodology

3.2.1 Data Homogenization

For our analysis, we convolve the data to match the spatial and spectral resolutions in all cases. This common resolution is defined by the poorest resolution of our data sets: the spectral resolution is set by the CARMA data, and the spatial resolution is set by the Nobeyama data. After hanning smoothing the data to a common spectral resolution (which is discussed below), we use the `REGRID` task in MIRIAD (Sault et al. 1995) to put all the data sets on a common grid. Finally, we convolve the data sets to the 15″ Nobeyama limiting spatial resolution.

The limiting spectral resolution is different for the two galaxies. NGC 4736 has a CARMA-limited 10 km s^{-1} spectral resolution, while NGC 5055 has a CARMA/Nobeyama-limited 5 km s^{-1} spectral resolution. Therefore, for NGC 5055 we first carry out the analysis at a 5km s^{-1} spectral resolution and then compare the results when using a 10 km s^{-1} spectral resolution. We find that our results do not change. Thus, for sake of uniformity, we here present the analysis using a common spectral resolution of 10 km s^{-1} for both galaxies.

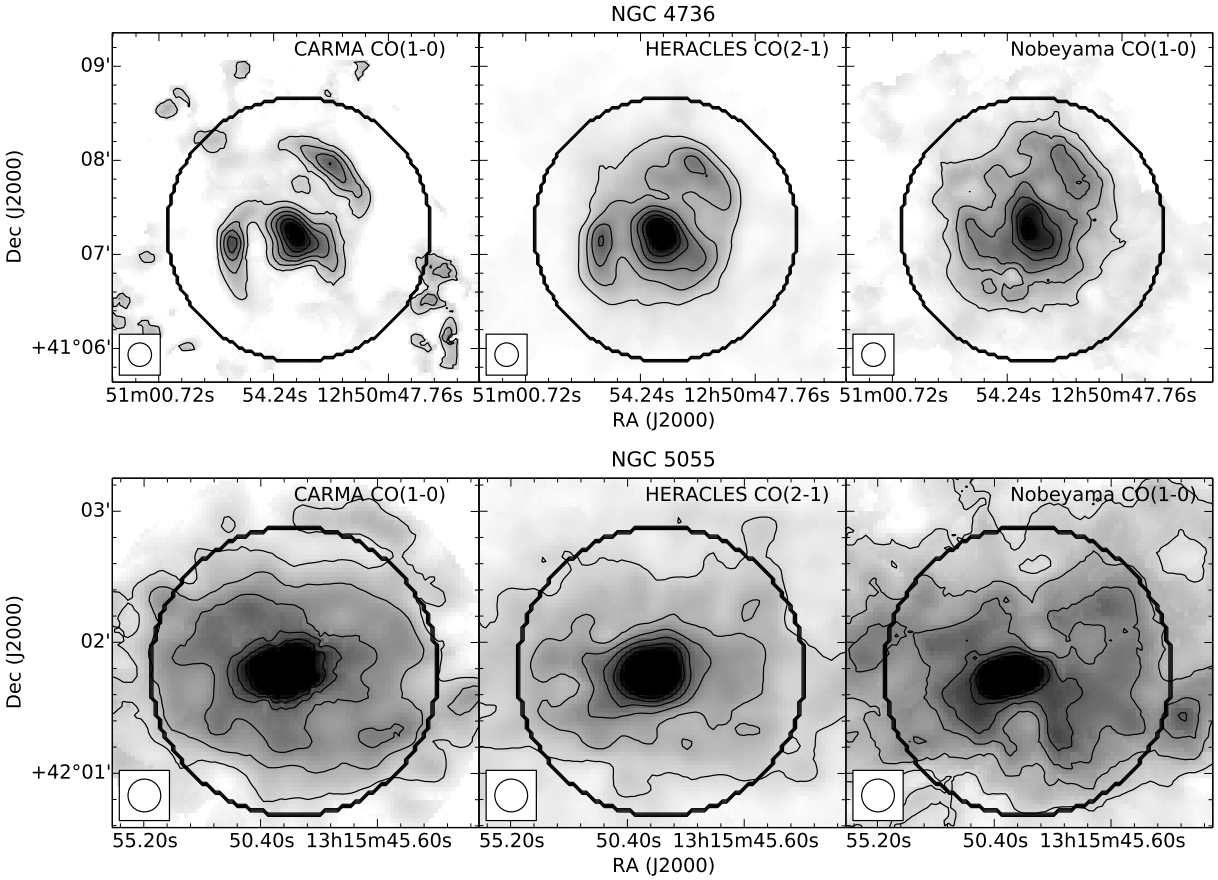

Figure 3.1 **CO integrated intensity maps of NGC 4736** (top) **and NGC 5055** (bottom). The first column shows the CARMA CO (1 – 0) interferometric data, the second column shows the HERACLES IRAM 30 m CO (2 – 1) maps, and the third column shows the Nobeyama 45 m CO (1 – 0) maps. The three maps are at 15″ resolution (the beam size is shown at the lower left corner) and were constructed using the HERACLES mask (details in Section 3.3.4). For both galaxies the intensity range goes from 0 to 38 K km s^{-1}, and the 6 contours show intensity levels separated by 6 K km s^{-1}, starting at 6 K km s^{-1}. The black circle shows the region where the CARMA cube has homogeneous noise properties, i.e., where the rms is within 30% of the value at the center of the map.

In order to correctly Nyquist sample the data, we construct a hexagonal grid with a 7.5″ spacing (half of the beam size, see Fig. 3.2).

Due to the attenuation of the primary beam in interferometric observations, the sensitivity drops toward the edges of the map. We construct a sensitivity mask (after primary-beam correction of the cube) from the interferometric noise map and apply it to all data sets. In this way we make sure (1) to use the same individual LOSs in all data sets, and (2) that we only use LOSs that have homogeneous noise properties in the interferometric data. To do so, we derive the galactocentric distance at which the noise in the CARMA observations is increased by 30%, and only use this region for further analysis. For clarification, we show this region as a solid black circle in Fig. 3.2 for each galaxy on top of the HERACLES IRAM 30 m integrated intensity map in gray shades. Inside the circle, we show our hexagonal grid points (blue x symbols). Finally, we show the 15″ radial bins used later in this paper as red ellipses.

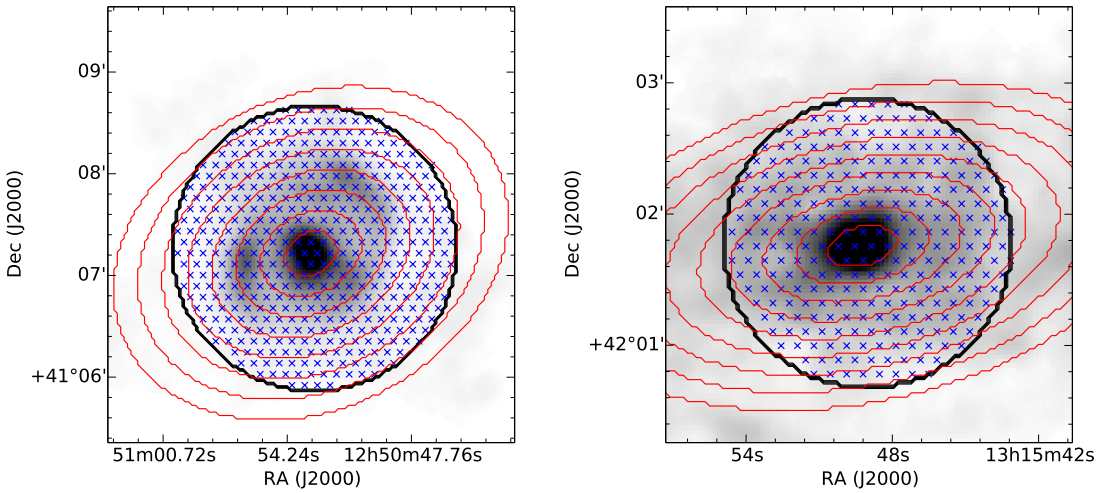

Figure 3.2 **Interferometric primary beam sensitive area.** HERACLES IRAM 30 m CO integrated intensity maps of NGC 4736 (left) and NGC 5055 (right) at 15″ resolution (grayscale). The black solid circle represents the area where the interferometric primary beam sensitivity is within 30% of the value of that at the center of the map. The blue points inside the circle show the hexagonal grid points that are used for sampling the data. The red ellipses show the 15″ radial bins used for stacking. From inside out and in units of r_{25} they are, for NGC 4736: 0.04, 0.10, 0.17, 0.23, 0.29, 0.35, 0.41, and 0.46; and for NGC 5055: 0.03, 0.07, 0.11, 0.15, 0.19, 0.23, 0.27, and 0.30.

From Fig. 3.2 we note that the sensitive region defined by the CARMA primary beam response is independent of the inclination of the galaxy. However, the radial bins are ellipses because of the inclination. This results in lower covering factors within the ellipses for the outermost radial bins. To quantify this effect, we present in Table 3.1 the number of LOSs from the hexagonal grid

Table 3.1. Filling factors within each 15″ radial bin

R_{25}	# Grid Points in Radial Bin	# Grid Points in CARMA – sens. Region (%)[a]	CARMA (%)	# of Significant Grid Points, S/N > 5 [b] HERACLES (%)	Nobeyama (%)	THINGS (%)
1	2	3	4	5	6	7
		NGC 4736				
0.04	10	10 (100)	4 (40)	9 (90)	3 (30)	6 (60)
0.10	35	35 (100)	28 (80)	32 (91)	20 (57)	32 (91)
0.17	57	57 (100)	44 (77)	57 (100)	40 (70)	57 (100)
0.23	73	73 (100)	34 (47)	73 (100)	43 (59)	73 (100)
0.29	101	101 (100)	12 (12)	72 (71)	24 (24)	101 (100)
0.35	116	99 (85)	0 (0)	43 (43)	0 (0)	99 (100)
0.41	142	64 (45)	1 (2)	25 (39)	0 (0)	61 (95)
0.46	165	10 (6)	0 (0)	3 (30)	0 (0)	8 (80)
		NGC 5055				
0.03	9	9 (100)	6 (67)	9 (100)	4 (44)	9 (100)
0.07	23	23 (100)	7 (30)	20 (87)	16 (70)	20 (87)
0.11	34	34 (100)	4 (12)	34 (100)	33 (97)	34 (100)
0.15	54	54 (100)	12 (22)	54 (100)	47 (87)	54 (100)
0.19	66	54 (82)	11 (20)	54 (100)	48 (89)	54 (100)
0.23	86	44 (51)	9 (20)	39 (89)	27 (61)	39 (89)
0.27	89	27 (30)	5 (19)	27 (100)	18 (67)	27 (100)
0.30	117	26 (22)	11 (42)	24 (92)	14 (54)	26 (100)

[a]Number of grid points within the CARMA sensitive region in a particular bin. In parentheses is the % of these grid points compared to the total number of grid points within each radial bin (i.e. compared to column 2).

[b]For each instrument and for each radial bin we show the number of LOSs with S/N > 5 and within the CARMA-sensitive region (black circle in Fig. 3.1). In parentheses is the % of these points compared to column 3.

that fall within each radial bin and within our mask (third column), as compared to the number of LOSs that would be present without taking into account the sensitivity mask (second column).

3.2.2 Measuring Line Widths for Individual LOSs

We estimate the spectral line widths using single Gaussian fits. In order to obtain reliable measurements for individual LOSs, we require that they have high significance. Therefore, we begin by computing the line widths for the LOSs that comply with the following characteristics: (a) lie within the CARMA sensitive region (black circle in Figure 3.1), (b) have peak signal-to-noise ratios[4] (S/Ns) > 5, and (c) have integrated intensities of at least 10σ, where $\sigma = \Delta v \sqrt{n}\, rms$ and Δv is the channel width, n is the number of measured points used to fit the line, and rms is the noise measured in a line-free channel. For each of these high S/N LOSs, we use the H I first

[4]This S/N is computed in the 10 km s^{-1}spectral resolution and 15″ spatial resolution cubes.

moment value, i.e., the local intensity-weighted velocity, as a proxy for the velocity where we expect to find the corresponding CO line (we take the H I data from the THINGS survey, Walter et al. 2008). This is based on our earlier findings that the H I and CO LOS velocities agree well at the resolution at which we are working (Schruba et al. 2011; Caldú-Primo et al. 2013). We attempt to fit a single Gaussian to each spectrum using `MPFIT` (IDL procedure from Markwardt 2009) inside a window of 100 km s^{-1} centered in the H I first moment value. If the fitted Gaussian is broader than 100 km s^{-1}, we proceed to refit with a double-horn profile (a Gaussian scaled by a symmetric second order polynomial; Saintonge 2007). Double-horn profiles are mostly found in the inner regions of galaxies, where bulk motions or beam smearing could be dominant. These will be discarded in our analysis (see below). The integrated intensity selection criterion (b) removes LOSs with significant negative structures ("bowls") in the interferometric data[5].

The errors are computed as discussed in detail in Chapter 2: for each LOS we add random noise to the original spectrum and redo the line width measurement. We repeat this procedure 1000 times. The adopted error in the line width measurement is the dispersion between the results of these 1000 iterations.

3.2.3 Measuring Line Widths for Stacked Spectra

The main purpose of the stacking is to increase the S/N in our data as well as to include all available LOSs in our analysis. The stacked spectra are the most meaningful measurements, as they represent the luminosity-weighted FWHM including all LOSs inside a tilted ring (and inside the CARMA sensitive region). In order to stack individual LOSs coherently, we first remove the circular motions of the four data sets using the H I first moment value. The THINGS survey has very high sensitivity, resulting in reliable velocity maps. Even in the case of NGC 4736, which has low H I content in the central parts, the peak S/N is larger than 5σ in 97.3% of the LOS inside $0.5\,R_{25}$. Once all spectra are centered in the same velocity frame (in this case zero velocity) they can be stacked coherently. The stacking procedure, together with the error determination, are described in detail in Chapter 2. After the stacking is done, we compute the line widths as discussed above. The total error in the determination of line widths has contributions both due to noise (as modeled for the individual LOSs above) as well as due to the specific selection of spectra that have been stacked (which we assess through bootstrapping).

[5]These negative bowls are expected to be present in interferometric data because of the extrapolation required to overcome the incompleteness of the *uv*-coverage.

3.3 Results

3.3.1 FWHM as function of Galactocentric Distance

We can select which LOS we want to stack. Since many galactic properties depend on the distance to the center of the galaxy, we choose to stack the individual LOSs inside tilted rings of 15″ width within each galaxy. As a first step, we stack only individual LOSs with $S/N > 5$. We then compare the measurements obtained from these (high S/N) stacked spectra to the median values measured from the individual high S/N LOSs. We do this comparison to test the validity of the stacking method. In Figure 3.3 we plot the FWHM measurements as function of galactocentric distance for each of the four different data sets (we include H I for the sake of completeness). The FWHMs measured when fitting high significance ($S/N > 5$) individual LOSs are shown as small gray symbols. The FWHMs measured when only stacking the gray points (i.e., individual LOSs with $S/N > 5$) are shown in medium-sized blue symbols, whereas the median FWHMs of the individual high S/N LOSs are shown as black small symbols (the red points are explained below). We see that at small radii ($R \lesssim 0.2\,R_{25}$) we observe a rapid increase in the measured FWHM; however, here the observed spectra are significantly broadened by beam smearing (see Chapter 2). The shaded regions highlight the radial range where beam smearing broadens the intrinsic line profile by more than 30%. For a galaxy with characteristics similar to NGC 4736, beam smearing accounts for > 30% of the measured line width at $R \lesssim 0.15\,R_{25}$ and for more than 10% out to $0.25\,R_{25}$. In NGC 5055, beam smearing accounts for > 30% of the observed line widths at $R \lesssim 0.2\,R_{25}$, and > 10% at $0.4\,R_{25}$. At large radii out to $0.5\,R_{25}$, where line profiles are only mildly or not at all affected by beam smearing, we find roughly constant CO velocity dispersions, as have been found already in earlier studies (e.g., Tamburro et al. 2009; Caldú-Primo et al. 2013). In the regions of interest (where beam-smearing is not dominant), the measurements obtained for LOS with SNR > 5 are in agreement.

In Table 3.1 (columns 4 – 7) we show the number of LOSs with S/N larger than 5 within each 15″ radial bin and within the CARMA-sensitive region for each of the data sets (in parentheses we show which percentage of the total number of LOSs within the CARMA-sensitive region these high S/N LOSs represent). It is important to note that we select the individual LOSs with high S/N independently for each data set, i.e., a high S/N LOS in the HERACLES cube does not necessarily have such a high S/N LOS counterpart in the CARMA cube[6] (see Table 3.1). It is clear that by taking only high S/N measurements we are excluding a large percentage of LOSs from the analysis.

[6]This problem does not exist when stacking all LOSs. In that case we do not perform a pre-selection, we simply stack all LOSs falling within the corresponding radial bin.

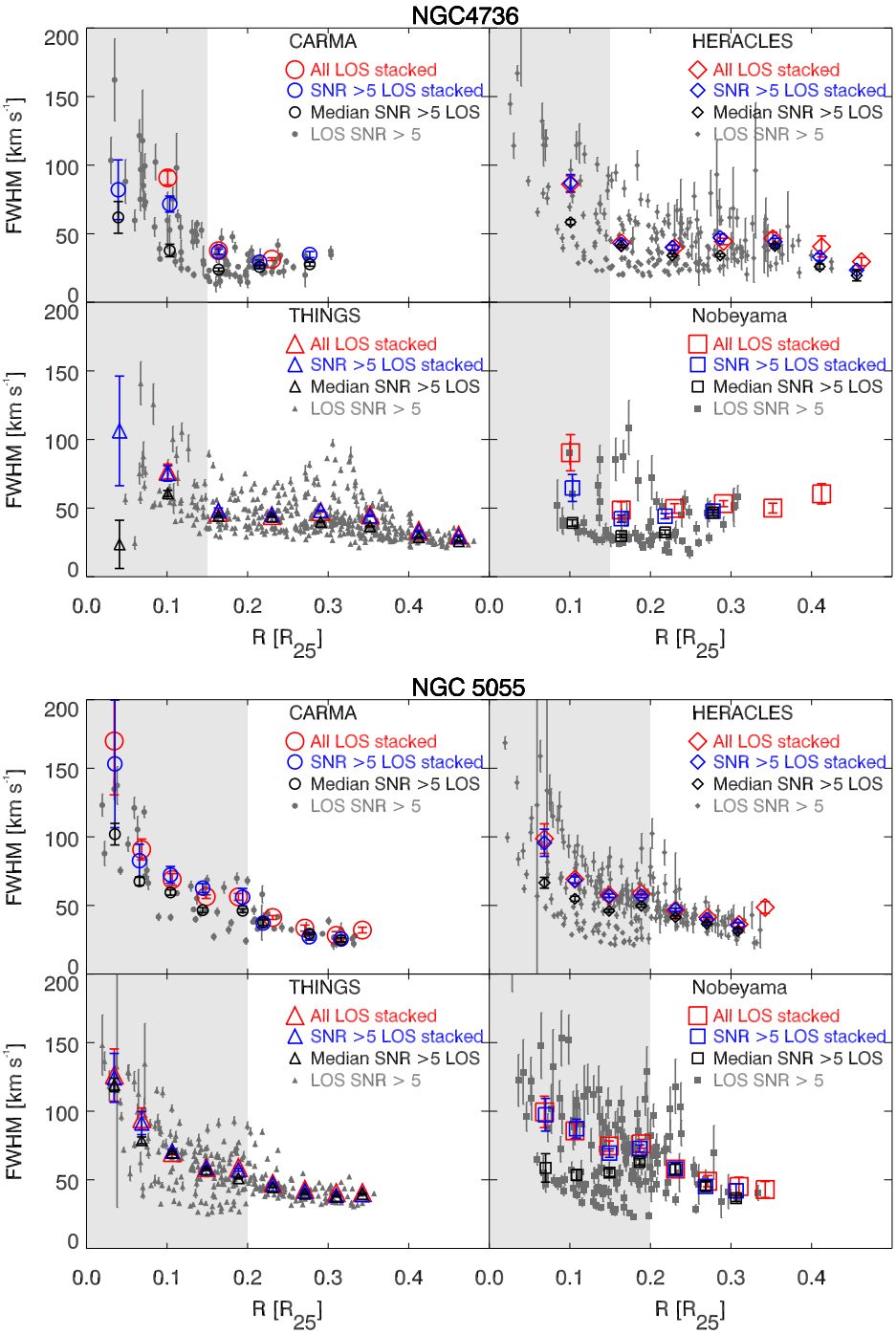

Figure 3.3 **FWHM as a function of galactocentric distance for the four different instruments:** CARMA (top left), HERACLES (top right), THINGS (bottom left), and Nobeyama (bottom right). The small grey symbols show individual LOSs with peak $S/N > 5$. The large red symbols show the values obtained when stacking all LOSs within a given tilted ring bin, the medium blue symbols show the results when stacking spectra with $S/N > 5$ only, and the black small symbols show the median values for the gray points, i.e., the median values of the individual high S/N LOS measurements. Inside the shaded area, beam smearing contributes by more than 30% to the measured line width.

Therefore, we then proceed to stack *all* LOSs inside the 15″ wide tilted rings. The resulting stacked spectra are shown in Figure 3.4 for NGC 4736 and NGC 5055, respectively. In these figures we show the normalized stacked spectra with peak S/Ns higher than 5 in all data sets. The corresponding FWHMs obtained for these stacked spectra are plotted in Figure 3.3 in large red symbols. The analysis of the stacked spectra (red symbols) gives the line widths for *all* LOSs within a radial annulus in a luminosity-weighted sense, thus also including faint LOSs.

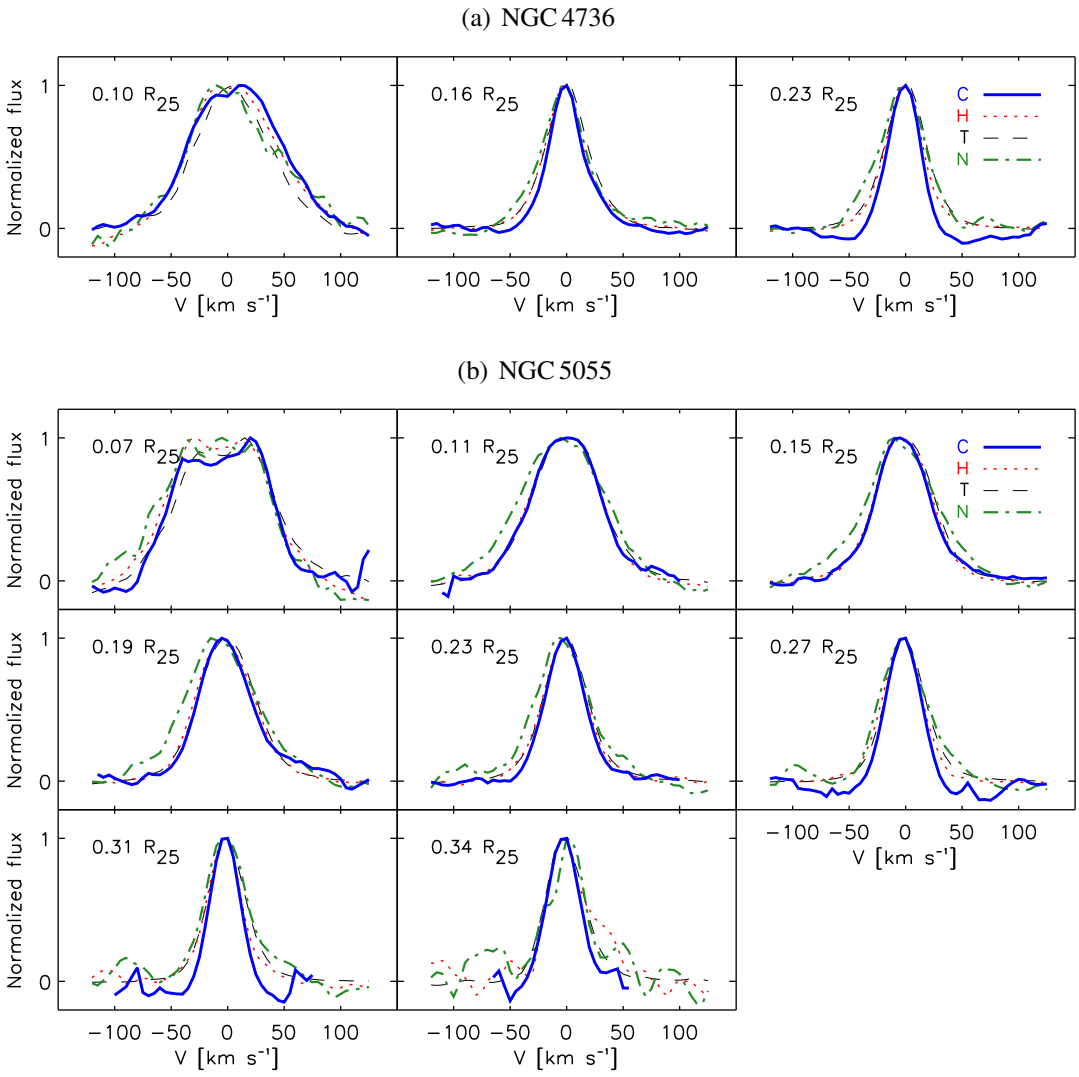

Figure 3.4 **Stacked spectra by galactocentric distance in bins of** 15″ **width.** The spectra for the 4 data sets are shown together, therefore fluxes have been rescaled to peak intensities of unity. The black line (labeled 'C') is the CARMA data, the red dashed line ('H') is the HERACLES data, and the green dash-dotted line ('N') is the Nobeyama data. For comparison we also show the THINGS H I data as the black dashed line (labeled 'T').

We find that the line widths of the stacked spectra including all LOS are typically larger (by 2% – 15%) than the values obtained when stacking only individual high S / N LOSs. A possible explanation is that the faint LOSs have systematically wider line widths than the high S / N LOSs, and when included in the stacks they widen the resulting spectral line width. Since high S / N LOSs are less than 20% of the total LOS in the CARMA data (which account for ∼ 60% of the interferometric flux), we cannot rely on these measurements as being representative of the underlying weaker emission.

3.3.2 Comparison of FWHM from Different Instruments

A visual inspection of Figures 3.3 and 3.4 already indicates that the CARMA data give the smallest line widths of all data sets (in those areas not affected by beam smearing). Figure 3.5 shows the ratio of the FWHM line widths measured using the single- dish telescopes, HERACLES (diamonds) and Nobeyama (squares), divided by the line widths measured by CARMA for our two galaxies, NGC 4736 (Figure 3.5, left column) and NGC 5055 (Figure 3.5, right column). The figure is divided in two. In Figure 3.5(a) we show the results for the stacked spectra including *all* LOSs. In Figure 3.5(b) we show the results involving *high S/N* LOSs: the stacked spectra are on top, and the median values of the individual LOSs are on the bottom. For comparison, we also show the ratio of the line widths of the THINGS H I data (triangles) with the CARMA CO (1 – 0) data. Open symbols show spectra fitted by a double-horn profile (typically at small radii where beam smearing is dominant), and solid symbols correspond to Gaussian fits (typically in the galactic disk)[7]. The shaded regions mark the galactocentric distance where beam smearing is larger than 30% for NGC 4736 and NGC 5055, respectively. Beam smearing tends to represent the large-scale gas kinematics instead of the intrinsic line profile. As this affects all data sets equally (after convolution to a common resolution), it drives any ratios of line widths toward unity, thus concealing any intrinsic differences. This is obviously the case at small radii (inside the shaded regions). At larger radii, where beam smearing is not important, the CO line widths measured from single-dish data sets (but also for the interferometric H I data) are larger than the line widths measured from the interferometric CARMA data.

In Table 3.2 we list the mean values for the ratios of the single-dish line widths from HERACLES and Nobemaya to the interferometric line widths from CARMA, for data only mildly affected by beam smearing, i.e., outside 0.15 R_{25} for NGC 4736 and outside 0.2 R_{25} for NGC 5055. The main finding of this paper is that the average ratio of single-dish to interferometer line widths is 1.4 ± 0.2 when looking at the CO (1 – 0) transition and taking into account only the high S / N LOSs. This value is in agreement with the ratio found when taking into account all LOSs

[7] In Figure 3.5(b) (bottom) we plot only filled symbols. There is no information about line profiles in this plot, since we are showing the median of individual measurements.

(a) Stacking all LOS

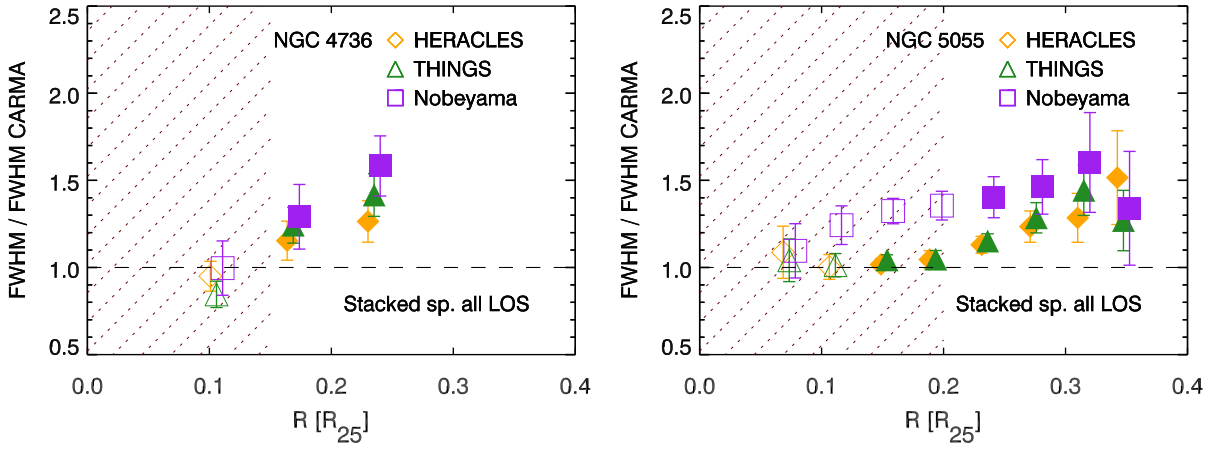

(b) Results involving individual LOS with SNR > 5

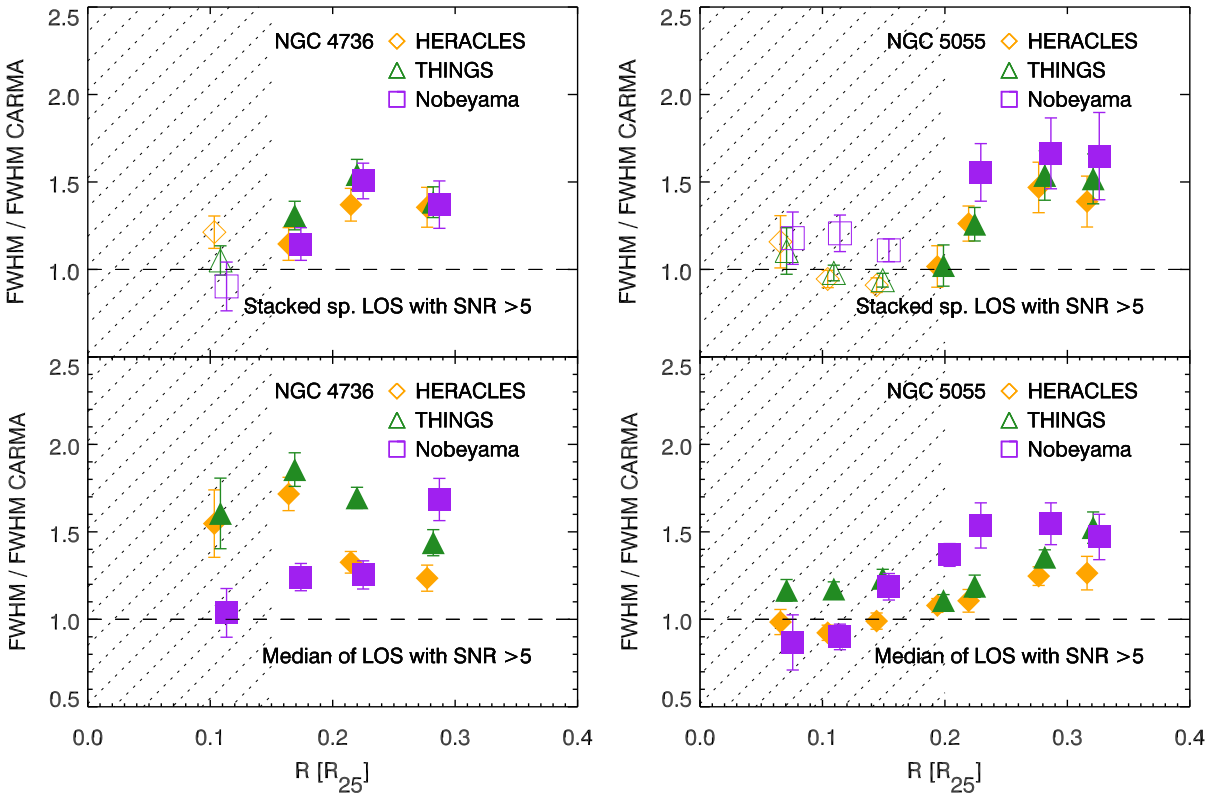

Figure 3.5 **Single-dish vs Interferometric FWHM.** Ratio of the FWHM computed for the different instruments over the FWHM computed from the CARMA data for NGC 4736 (left column) and NGC 5055 (right column). *Top:* Stacked spectra using all LOSs inside radial bins of 15″. *Center:* Stacked spectra of high S / N LOSs. *Bottom:* Median values of the high S / N individual LOSs. The different symbols correspond to the different ratios: HERACLES/CARMA as diamonds, THINGS/CARMA as triangles, and Nobeyama/CARMA as squares. The shaded areas correspond to the regions inside which beam smearing contributes more than 30% to the measured line width measurements. The dashed line represents unity. The colors correspond to the colors in Figure 3.3.

(1.5 ± 0.1). Thus, single-dish observations typically trace molecular gas with larger line widths than interferometric observations. This points to the existence of a molecular gas component that is missed by the interferometer and that has larger line widths.

3.3.3 Tests

3.3.3.1 Radial bin filling factor

As noted before, in the case of NGC 5055 we face incompleteness for the outermost radial bins in this study (see Figure 3.5(a)). We test how representative the measured values are, taking into account the incompleteness in these points. To do this we take the last complete radial bin in NGC 5055, which goes from $45'' - 60''$ (centered at $\sim 0.15\,R_{25}$). We then take a grid of filling factors going from $90 - 10\%$ (i.e., how many individual LOSs within the radial bin are taken into account). We randomly select the corresponding percentage of individual LOSs inside the radial bin and we stack them. Finally, we measure the FWHMs from the resulting stacked spectrum. We perform this same procedure 1000 times in order to see how much the measurement varies by selecting random individual LOSs. At the end we calculate a mean value of the FWHM computed 1000 times for each filling factor value and the dispersion among individual measurements.

We compare the "true" FWHM (i.e., the FWHM obtained when stacking 100% of the LOSs inside the radial bin) to the mean FWHM obtained for each filling factor. For the CARMA data the variation is at most 2% of the original value. For the HERACLES, Nobeyama, and THINGS data the variations are at most 2%, 3%, and 6%, respectively. For these three data sets, the variations rise to 5%, 12%, and 4%, respectively, in the case where the filling factor is only 10%. Looking at each data set individually, we note, as expected, that the dispersion in the measurements increases with decreasing filling factor, going from $\sim 1\,\mathrm{km\ s^{-1}}$ for the 90% filling factor up to $\sim 4\,\mathrm{km\ s^{-1}}$ for the 10% filling factor. In all cases, the dispersion is of the same order as the errors calculated for the stacked spectra ($\sim 2 - 4\,\mathrm{km\ s^{-1}}$).

3.3.3.2 FWHM dependance on azimuthal location

Since the circular velocities have a larger gradient along the minor axis (due to projection effects), we also test whether the angular distance to this axis affects our FWHM measurements. For each galaxy we mask out a wedge of X degrees around the minor axis, where X ranges from 5 to 40° in steps of 5°. We then stack the remaining LOSs and compare the FWHM to the value obtained when using no mask. For both galaxies and for all angles, the differences in FWHM

measurements are less than a channel width ($< 2.5\,\mathrm{km\,s^{-1}}$), which is 5% – 10% of typical FWHM measurements, and are therefore insignificant.

3.3.3.3 Pointing uncertainties

At this stage we test whether the single-dish pointing uncertainties could be responsible for the excess in the FWHM measurements. We convolve each single-dish cube with a Gaussian of width equal to the corresponding pointing uncertainty.[8] We compare the resulting FWHM to the FWHM measured from the original cubes. In all cases the differences between both measurements are less than 2%. The pointing uncertainties are thus insignificant in the determination of FWHM values.

3.3.3.4 Filtering of extended emission

In this subsection we simulate what the interferometer would detect using the task `simobserve` in the *Common Astronomy Software Applications* package (CASA, McMullin et al. 2007). As our galaxy template, we use the HERACLES single-dish cube, which contains all emission (clumpy and/or diffuse). We simulate what CARMA's E-configuration *uv*-coverage would recover. We here choose CARMA's most compact configuration since this configuration recovers the largest scales. After constructing the interferometric cube using `simobserve`, we analyze the simulated interferometric data in the same way as we did with the real data. Finally, we compare the FWHM measured in the simulated interferometric observations to the HERACLES observations. We find that the HERACLES values are larger by an amount ($\sim 50\%$) similar to the values measured in the simulated interferometric data. This further supports the idea that the information filtered by the interferometer results in narrower line widths, i.e., the extended emission filtered out by the interferometer also has a larger velocity dispersion.

Finally, we caution that CARMA and Nobeyama observed the CO (1 – 0) transition whereas HERACLES observed CO (2 – 1). The mean ratio of the Nobeyama to CARMA line widths is $\sim 25\%$ larger than the corresponding mean ratio of HERACLES to CARMA line widths. This difference might be due to different excitation temperatures within the clumpy or diffuse gas or due to different optical depth effects. With the available data we cannot differentiate between those two mechanisms.

[8] The IRAM 30 m telescope has a pointing accuracy of ~ 2" and the Nobeyama 45 m telescope as a pointing accuracy of $\lesssim 7$".

Table 3.2. Linewidth Ratios

	$\mathrm{HERACLES}_{\mathrm{CO}\,(2-1)}/\mathrm{CARMA}_{\mathrm{CO}\,(1-0)}$	$\mathrm{Nobeyama}_{\mathrm{CO}\,(1-0)}/\mathrm{CARMA}_{\mathrm{CO}\,(1-0)}$
Stacked, all LOS [a]	1.2 ± 0.1	1.5 ± 0.1
Stacked, SNR > 5 [b]	1.3 ± 0.1	1.4 ± 0.2
Median, SNR > 5 [c]	1.3 ± 0.2	1.3 ± 0.2

[a]Mean of values measured when stacking all LOSs.

[b]Mean of values measured when stacking individual LOSs with SNR > 5.

[c]Median of values measured for the individual LOSs with SNR > 5.

3.3.4 Flux Comparison

We compare the fluxes recovered using the single-dish and the interferometric data sets by means of integrated intensity maps (i.e., zeroth-moment maps). To construct these maps we first create 3D masks that we use to blank the noise-dominated regions in the cubes. We construct these 3D masks by finding regions with peak S/Ns larger than 5σ in at least two consecutive channels. We then expand these masks to masks constructed in the same way, but using an S/N cut of 2σ instead. Finally, we expand the mask by half a beam size and include adjacent velocity channels to capture all emission. We construct two masks for each galaxy; one for the interferometric CARMA data set and another one for the single-dish data sets. For the single-dish data sets we use the HERACLES cubes to construct the masks, as it has higher S/N as compared to the Nobeyama data sets. The final mask is applied to each cube and the integrated intensity is calculated.

We compare the fluxes in three ways. (A) We compute the integrated intensity map for each data set independently (each data set with its own 3D mask). We then measure the flux inside the region limited by the CARMA-sensitive region (indicated in Figure 3.1). (B) We compute the integrated intensity map for each data cube, but use the CARMA 3D mask in all cases. (C) We compute the integrated intensity map for each data cube, but use the HERACLES 3D mask in all cases. We then measure the flux inside the CARMA-sensitive region. The uncertainties we state in Table 3.3 only take into account the canonical 10% flux calibration uncertainty for each measurement, which is likely a lower limit to the actual uncertainties.

The percentage of flux recovered by the interferometer, compared to the flux measured by the single-dish telescope, for the three different approaches is presented in Table 3.3. Method A tells us how much flux is recovered by each instrument, even if the flux originates in not exactly the same position, but in the area where CARMA has sufficient sensitivity to pick up emission. Method B is constrained to look for emission where there is CARMA emission, whereas method C is constrained to look for emission where there is HERACLES emission. These results show that even with Method B, where we measure flux in precisely the interferometric 3D mask, the interferometer recovers $\sim 74-81\%$ (depending on the galaxy) of the flux recovered by the single-dish. Using method A, which looks for flux in the whole region where CARMA has good sensitivity, we find that in the case of NGC 4736 the flux recovery by the interferometer is only $\sim 52\%$, while for NGC 5055 it is much higher (92%). With method C, which by construction looks for emission using the single-dish 3D mask, the interferometer recovers $\sim 35\%$ of the flux in the case of NGC 4736 and $\sim 92\%$ in the case of NGC 5055. In the case of NGC 5055 the flux recovery is approximately the same, regardless of the mask used for the computation of the moment maps. In the case of NGC 4736 the flux recovery varies from $\sim 35\%-74\%$, depending on the choice of mask.

Regarding the interferometric flux measurements, we recall that during the image deconvolution process, the flux recovery will also depend on the noise properties (e.g., Helfer et al. 2002). The cleaning procedure recovers only the flux that is above a few times the noise rms. Therefore, the flux that is not being recovered by the interferometer due to the noise properties is a low amplitude component.

Finally, as a consistency check, we compare the flux from the Nobeyama 45 m cubes to the flux measured by the NRAO 12 m telescope, observed as part of BIMA SONG (Helfer et al. 2003). For NGC 4736 we find that the flux measured in both observations agrees within 8%, whereas for NGC 5055 the agreement is within 15%. In the case of NGC 4736 the interferometer is clearly not recovering all the flux measured by the single-dish. In NGC 5055 the single–dish and interferometric flux measurements agree within their uncertainties.

3.4 Discussion

We present a comparison between FWHM line widths obtained from interferometric CARMA CO (1 – 0) data to single-dish CO (2 – 1) data from the IRAM 30 m and to single-dish CO (1 – 0) Nobeyama 45 m telescopes in two nearby spiral galaxies: NGC 4736 and NGC 5055. After convolution of the data sets to a common spatial and spectral resolution, we measure single-dish line widths that are $\sim(40 \pm 20)\%$ larger than interferometric ones (when looking at the common CO (1 – 0) transition) and when taking into account the high-S / N-only LOSs. If we take into

Table 3.3. Flux Recovery by the Interferometer[a]

	Method A	Method B	Method C
NGC 4736	(52 ± 14)%	(74 ± 14)%	(35 ± 14)%
NGC 5055	(92 ± 14)%	(81 ± 14)%	(92 ± 14)%

[a]The percentages show the fraction of flux recovered by the interferometer (CARMA) as compared to the single – dish (Nobeyama).The uncertainties are computed using the typical 10% flux calibration uncertainty for each measurement.

account all LOSs for the stacking, we get single-dish FWHMs that are ∼(50 ± 10)% larger than the interferometric ones. If the interpretation of a diffuse molecular gas component is correct, we would expect the highest S / N LOS to be dominated by the emission coming from GMCs. The diffuse emission would be more prominent in lower S / N LOSs. Furthermore, the flux comparisons we perform point to a flux recovery by the interferometer as low as ∼ 52% – 74% of the flux measured by the single-dish telescope over the same region in the case of NGC 4736. This result is consistent to what Pety et al. (2013) found in the case of M 51. In the case of NGC 5055 the interferometric flux recovery is higher ∼ 81% – 92%, and taking into account the uncertainties in the flux determination, we cannot rule out a full flux recovery by the interferometer for this galaxy. In summary, we measure large line widths and larger flux recoveries from the single-dish observations as compared to the interferometric ones. The molecular gas "unseen" by the interferometer could have two possible configurations.

One possibility is that this gas is diffuse, i.e., with lower average densities as compared to the gas present inside GMCs. There is evidence for diffuse molecular gas in our Galaxy observed through absorption lines (Snow & McCall 2006; Burgh et al. 2010 and references therein). The column densities of the diffuse gas are found to be $\lesssim 30$ times smaller than those in molecular clouds and with typical temperatures determined from diffuse H_2 to be $\gtrsim 30$ K (Liszt et al. 2010). This diffuse gas would need to extend over volumes larger than the maximal scales traced by the interferometer, and thus be filtered out. The other possibility is that the gas is inside small molecular clouds that are separated among each other by less than a synthesized beam size. This configuration would appear as a large regular structure to the interferometer, and therefore would be filtered out. The physical properties of these clouds (temperature and density) may be (or not) comparable to the values measured inside GMCs. In this case larger velocity dispersion would

be the result of cloud-to-cloud motions. With the available data we cannot distinguish between these two possible scenarios. A detailed analysis of CO isotopes might help discriminate between diffuse and dense gas (Liszt et al. 2010), as would higher spatial resolution observations.

In Galactic studies, the existence of a diffuse molecular gas is well accepted (e.g., Liszt & Pety 2012; Sheffer et al. 2008). However, these studies are hampered by uncertain distances and projection effects that make it difficult to quantify the amount of gas present in this pervasive component. Studies of nearby galaxies offer an "outside view" that does not face these difficulties, though measurements are still sparse. Firmly establishing the existence of such a spatially extended and high-velocity dispersion molecular gas phase would have important implications. The velocity dispersion measured from molecular gas emission (thought to arise from GMCs only) has been broadly used for molecular gas scaling relations, or Larson's laws (Larson 1981), among other things, to study star formation. The presence of two different molecular gas configurations could imply that these scaling relations may not be constant throughout the galaxy (depending on the dominant molecular gas configuration). Specifically in the extragalactic context, where different instruments (single-dish and interferometer) yield different velocity dispersion measurements, studies of a larger sample are needed in order to quantify how the scaling relations (for example, velocity dispersion-molecular cloud size) would be affected.

As a final comment, a complementary observational approach to address the same question is to study edge-on galaxies, as was done by Garcia-Burillo et al. (1992). They detect molecular gas up to ~ 1 kpc off the plane of the galaxy. They interpret this as evidence of a thick molecular disk in NGC 891, which is also in agreement with a diffuse molecular gas component, since higher velocity dispersions in principle imply a larger scale height of the molecular gas disk. Future observations with ALMA, using both interferometric observations as well as total power measurements, will be crucial to shed more light on the nature of this "diffuse" molecular gas phase in galaxies.

CHAPTER 4

MOVING TO HIGHER SPATIAL RESOLUTION: M 31[†]

In the previous two chapters I present line width measurements performed at resolutions that exceed the typical sizes of molecular clouds (~ 50 pc). Our results obtained so far point to the existence of a molecular gas component which is more diffuse, and that has larger line widths than those typically measured within GMCs. This conclusion has been reached from results obtained by two different kind of instruments: interferometers and single-dish telescopes. This pair of instruments are sensitive to different spatial scales; interferometers can only probe compact emission, while single-dish telescopes are able to recover extended emission as well (at coarser resolution). The aim of the next project is to investigate whether molecular gas line widths obtained by single-dish telescopes are larger than those obtained by interferometers on GMC spatial resolutions. There are two ways to attain better spatial resolution at good sensitivity: using larger instruments or observing closer objects.

The closest spiral galaxy to us is the Andromeda galaxy, or M 31, lying only 785 kpc away (Ribas et al. 2005). It has an inclination of 77° and a position angle of its major axis of 38° (McConnachie et al. 2005). Due to its proximity, it has been extensively studied at many wavelengths (e.g. see Fig. 1.1), including some molecular gas tracers. Observations of molecular gas in Andromeda have been mostly carried out with single-dish telescopes (e.g., Nieten et al. 2006; Dame et al. 1993). The reason for this is that having such a large galaxy (2 deg $\times$ 0.5 deg on the sky), so close to us, has a drawback: making interferometric maps of such a large area turns

[†]Caldú-Primo, et al. in prep.

out to be observationally extremely expensive. There are a few interferometric studies on M 31, but they target small regions within the galaxy: e.g., Rosolowsky (2007) carried out CO (1 – 0) observations using the Berkeley-Illinois-Maryland Association (BIMA) interferometer to map a 7.4 kpc^2 (100″ × 100″) region along a spiral arm at ∼ 10″ spatial resolution[1]; and Sheth et al. (2008) use also BIMA to map CO (1 – 0) in a 2′ × 2′ field in its northeastern spiral arm with a beam size of 7.11″ × 5.71″. In order to get a more homogeneous coverage of a large region of M 31, Schruba et al. (in prep) conducted the CARMA Survey of Andromeda. This survey maps CO (1 – 0) emission along M 31's molecular rings at 5- and 10-kpc from the galaxy center. These large scale structures are prominent in atomic and molecular gas, and in recent star formation tracers.

We will use interferometric high spatial resolution data from the CARMA Survey of Andromeda (Schruba et al., in prep) and single-dish data obtained by Nieten et al. (2006) to investigate how line widths measured from these two instruments compare. With such high sensitivity data, we will try to constrain the properties of the molecular gas which is giving rise to the larger line widths that we have so far measured in single-dish data.

This chapter is structured as follows. In Section 4.1 we describe the data sets used in this project. In Section 4.2 we describe the methodology used to carry out the analysis. Section 4.3 contains the results and discussion, and finally Section 4.4 briefly presents our conclusions.

[1]They also perform a survey on a larger area (20 kpc^2, 1885″ × 350″), but with ∼ 40% coarser resolution.)

4.1 Data

4.1.1 Single-dish Data

Nieten et al. (2006) carried out a CO (1 – 0) line survey over a fully sampled 2 deg × 0.5 deg area of Andromeda using the IRAM 30 m telescope. The observations were taken between November 1995 and August 2001. They observed in *on-the-fly* mode, using two SIS receivers with orthogonal polarizations and two backends of 512 × 1 MHz, resulting in a velocity resolution of 2.6 km s^{-1}. The spatial resolution of these observations at 115 GHz is 23″, corresponding to 85 pc along the major axis. The data cubes have a pixel size of 8″. The noise properties of this data set are spatially inhomogeneous, varying from ∼ 33 mK rms noise per channel in the southern fields, to ∼ 25 mK in the northern ones. These noise values correspond to deprojected molecular gas surface density (Σ_{H_2}) sensitivity[2] of 3σ of 4.2 $M_\odot$ pc^{-2} and 3.2 $M_\odot$ pc^{-2}, respectively, for a CO line extending over 30 km s^{-1}.

4.1.2 Interferometric Data

The CARMA Survey of Andromeda (Schruba et al., in prep) maps CO (1 – 0) emission over an area of 365 arcmin^2 (18.6 kpc^2) in regions where at least modestly bright CO signal has already been detected (see Fig. 4.1). The observations were carried out from May 2011 to January 2014, using CARMA's compact D and E configurations. The mapped area consists of 6 mosaic fields; three of which cover part of the 10 kpc molecular ring (and in Fig. 4.1 are marked with numbers 10, 12, 14, 15, and 16), while the other three lie along the North-East major axis of the galaxy (numbers 9, 17, and 21 in the figure). Field 9 lies on the inner 5 kpc molecular ring, while the other two smaller fields (17 and 19) point to less active star-forming regions outside the 10 kpc molecular ring. The observations used a Nyquist-sampled mosaic of 1554 pointings and required 686 hours of telescope time. Except for field 21, all fields had been previously observed in CO (1 – 0) by the IRAM 30 m survey (Nieten et al. 2006). Since our aim is to compare observations of both instruments, we will not make use of field 21.

The CO (1 – 0) line at 115.271 GHz (λ = 2.6 mm) was observed using three 62 MHz spectral windows, each consisting of 255 channels of 244 kHz width (∼ 0.73 km s^{-1}). The calibration and deconvolution of the data was carried out using the data analysis software package MIRIAD (Sault et al. 1995). The resulting cubes have pixel sizes of 2″ and channel widths of 2.5 km s^{-1}, to match the single-dish spectral resolution.The final average beam size, after combining all

[2]This conversion assumes a CO line ratio of $I_{CO\,(2-1)}/I_{CO\,(1-0)} = 0.7$ and a CO (1 – 0)-to-H_2 conversion factor $X_{CO} = 2.0 \times 10^{20}$ cm^{-2}

uv-data sets and cleaning using a Briggs's robust 0.5 weighting, is of 5.5″. The corresponding average rms noise per channel (2.5 km s^{-1}) in the clean cube is ∼ 175 mK. Considering the CO line extends over 10 km s^{-1}, this rms noise translates into a 3σ deprojected mean molecular gas surface density (Σ_{H_2}) of 2.5 $M_\odot$ pc^{-2} or a 6σ point source sensitivity of M_{H_2} $\approx 10^4$ $M_\odot$. For more details on the observations and data reduction see Schruba et al. (in prep.).

4.1.3 Merged Cube

A common procedure to correct for the missing flux due to the short-spacing problem is to combine single-dish and interferometric data. The resulting merged cube contains high resolution information from the interferometric observation, without losing the extended emission which is only detected by the single-dish. Schruba et al. (in prep) perform such a combination using the Miriad task `IMMERGE` with its standard parameters. `IMMERGE` performs the combination by adding the single-dish and interferometric data cubes in Fourier space and then transforming the resulting combined visibilities back to image space. Schruba et al. (in prep) find that after masking the data cubes in order to detect genuine emission, the CARMA observations, on average, recover 57% of the flux present in the IRAM 30 m single-dish data cube.

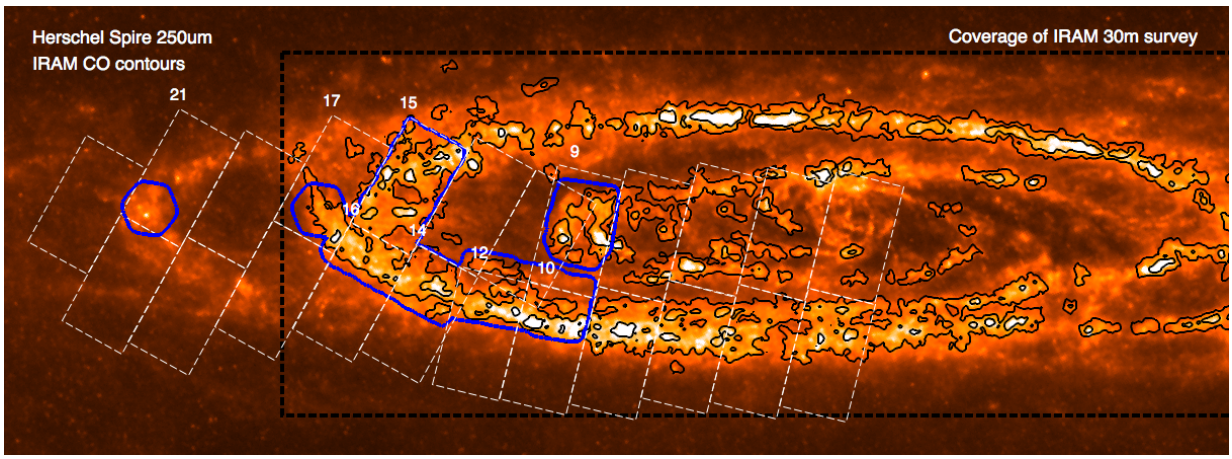

Figure 4.1 **M 31 molecular gas observations coverage.** This figure, taken from Schruba et al. (in prep) shows a Herschel 250 μm image of M 31, overlaid by IRAM 30 m black contours at 0.75 and 4 K km s^{-1}. The black dashed line shows the extent of the IRAM 30 m survey. The white rectangles show the regions targeted by the HST PHAT survey (the Panchromatic Hubble Andromeda Treasury survey mapped roughly a third of M 31's star forming disk, using 6 filters covering from the ultraviolet to the near infrared, Dalcanton et al. 2012), while the blue lines mark the area observed by the CARMA survey of Andromeda.

4.1.4 Ancilliary Data: Star Formation

In Chapter 2 we already examined the possibility that CO FWHM could be driven by star formation activity on ~ 0.5 kpc scales. We did it by comparing SFR calculated by a combination of FUV and 24 μm emission with the FWHM measurements obtained within the same regions. We found no strong correlation. We want to investigate whether we observe a correlation at the scales probed in this case for M 31. To do so we use different tracers of recent star formation:

GALEX FUV As already mentioned in Section 2.1.4, FUV radiation traces unobscured recent star formation. This radiation is emitted by O and B stars with typical ages of 20 – 30 Myr, reaching sensitivities of up to ~ 100 Myr (Salim et al. 2007). Thilker et al. (2005) observed the whole extent of M 31 in FUV and NUV as part of the GALEX NGS (Galaxy Evolution Explorer Nearby Galaxy Nearby Galaxies Survey). The FUV band spans from 1350 Å to 1750 Å . It has an angular resolution of 4.5″ and a typical 1σ sensitivity limit of 6.6 erg s^{-1} cm^{-2} Å^{-1}.

MIPS 24 μm The mid-infrared 24 μm emission traces embedded star formation, as it mainly comes from young stars' photons reprocessed by dust. M 31 photometry at 24 μm was observed by Gordon et al. (2006) using the Multiband Imager Photometer for Spitzer (MIPS). The observations cover a $1^\circ \times 3^\circ$ region along M 31's major axis. MIPS resolution at this wavelength is $\sim 6''$.

PACS 70 μm and PACS 160 μm Monochromatic infrared tracers are commonly used to model spectral energy distributions (SED), to then compute the total infrared luminosity, which is correlated with star formation (Kennicutt 1998). Stemming from this, different attempts to calibrate SFR with monochromatic infrared wavelengths (in particular using 70 μm and 160 μm) have been carried out (e.g., Calzetti et al. 2010). The photometry of these two wavelengths comes from observations carried out using the Photoconductor Array Camera and Spectrometer (PACS) on the *Herschel* space telescope (Fritz et al. 2012; Krause et al., in prep). The resolutions are $\sim 5.6''$ and $\sim 11.4''$ for 70 μm and 160 μm, respectively.

Hα This recombination line at 6564 Å (which corresponds to the first transition of the Balmer series of the hydrogen atom) is characteristic of H II regions, and is widely used as a SFR tracer indicator (Spitzer 1978). This SFR tracer is sensitive to the most recent star formation, with mean peak sensitivity at 3 Myr (Hao et al. 2011). The Hα map of M 31 was observed with the Mosaic Camera on the Mayall 4 m telescope as part of the Local Galaxies survey (Massey et al. 2006). It is sensitive to an Hα magnitude of 20 and has an average point-spread function of 1″.

4.2 Methodology

In this section, the common methodology we use to analyze the data is described. We are interested in quantifying line widths in the molecular gas of M 31. In particular, we want to compare measurements from interferometric and single-dish data. The first step is to convolve all data sets to the same limiting single-dish spatial resolution of 23″. After the convolution is done, we construct a hexagonal grid of 11.5″ separation (half of the beam size) from which we select the LOSs we keep for further analysis. This grid choice over-samples the independent data points by a factor of 4.

4.2.1 Individual LOSs

Following the work done in the previous two chapters, we are interested in quantifying line widths by means of Gaussian fits. The M 31 data sets have higher sensitivity and spatial and spectral resolutions than the data sets used before. Therefore, we can perform robust line width measurements in individual LOSs. We perform single Gaussian fits using the least squares fitting procedure `MPFIT` (IDL procedure from Markwardt 2009). To perform the fitting, it is necessary to constrain the velocity range where the spectrum lies. Since we are studying regions with sufficient CO signal, we use the intensity weighted mean velocity (or first moment of intensity) map, obtained from the merged cube, as a proxy for where to look for the emission. For each LOS, we take the corresponding mean velocity value, and define a 50 km s^{-1} window around this value. We perform the fitting using the data points inside this window. After the fitting is done for *all* LOSs, we keep for further analysis only those which meet the following conditions: a) FWHM larger than the 2.5 km s^{-1} channel width, b) peak S / N $\geq$ 5; c) integrated intensity along the line should be at least 10 times the uncertainty in the measurement[3] defined as $\sigma = \Delta v \sqrt{n}\, rms$; and d) the area under the Gaussian and the integrated intensity should not differ by more than 20%. The LOSs which fulfill these conditions account for 2% of the total number of LOSs in the data cube; however, they are responsible for $\sim$ 24% of the CO intensity. By excluding LOSs that do not comply with this criteria, we leave out spectra with important deviations from a Gaussian profile (i.e., double-horn profiles). Keeping them would complicate the subsequent analysis, as these profiles could arise from large scale motions or from a superposition of molecular clouds along the line of sight, rather than from intrinsic gas motions. The analysis of the results obtained by fitting single Gaussians to individual LOSs is discussed in Section 4.3.1.

[3]For the derivation see the Appendix of Mangum & Shirley (2015).

4.2.2 Stacking spectra

In order to characterize differences in line profiles from the two CO data sets as a function of specific physical parameters (e.g. peak intensity), we will carry out stacking of individual spectra. One thing we specifically want to investigate is whether we see a broad component in the single-dish data. Therefore, we will only stack the LOSs which fulfill the conditions imposed in the previous section (4.2.1), i.e. we will only stack high S / N LOSs. We do this to avoid identifying a broad component in the noise regime.

To stack spectra, we first need to shift the individual LOSs to remove velocity motions originating by rotation or bulk motions from the CO lines, analogously to what we did in the previous two Chapters. Since in this case we are working with the highest S / N LOSs, we use the peak velocity maps for each instrument. For each LOS, we take the corresponding peak velocity value to shift the spectrum by it. Once the large scale motions have been removed, the spectra is ready to be stacked coherently. The subsequent analysis on stacked spectra is presented in Section 4.3.3.

4.3 Results and Discussion

4.3.1 FWHM from single Gaussian fits

As explained in the previous section, we first fit single Gaussians to individual LOSs. The fitting is done for the three different data sets (single-dish, interferometer, and merged) independently. In Figure 4.2 we show three plots. For each plot, the x-axis corresponds to the FWHM values measured in each data set: interferometric data set (left, orange), single-dish data set (center, purple), and merged cube data set (right, green). The y-axis is the same for the three panels, and corresponds to the ratio between the single-dish FWHM and the interferometric FWHM ($\mathrm{FWHM_{SD}} / \mathrm{FWHM_{I}}$). On top of each plot we show a histogram with the distribution of FWHM values measured for each data set. At the right hand side of the three plots we show a histogram with the $\mathrm{FWHM_{SD}} / \mathrm{FWHM_{I}}$ values. The median of the single Gaussian FWHM values measured in individual LOSs, together with their 1σ deviations, are $7.3 \pm 2.5\,\mathrm{km\ s^{-1}}$ for the interferometer, $11.1 \pm 3.3\,\mathrm{km\ s^{-1}}$ for the single-dish, and $10.0 \pm 3.0\,\mathrm{km\ s^{-1}}$ for the merged cube. The ratio between single-dish and interferometric FWHMs has a median value of 1.5 ± 0.37.

This result is in agreement to what we measure in Chapter 3 for NGC 4736 and NGC 5055, where we find single-dish line widths that are $(40 \pm 20)\%$ larger than interferometric line widths. In the present chapter, the component that is being filtered out by the interferometer gives rise to line widths that are $\sim 50\%$ larger than the ones measured for the interferometric data. The median

of the single-dish FWHMs we measure in Andromeda has a value of $11.1 \pm 3.3\,\mathrm{km\ s^{-1}}$, which is, on average, 10% lower than the median value we previously measured for the 12 galaxies ($12.0 \pm 3.9\,\mathrm{km\ s^{-1}}$, see Chapter 2).

In Andromeda we are working at deprojected linear scales of $\sim 85\,\mathrm{pc} \times 380\,\mathrm{pc}$, while in the previous two galaxies the deprojected linear scales are $\sim 375\,\mathrm{pc} \times 497\,\mathrm{pc}$ and $\sim 540\,\mathrm{pc} \times 1048\,\mathrm{pc}$ for NGC 4736 and NGC 5055, respectively. We are not only working at different spatial resolutions; but the largest spatial scales to which the interferometer is sensitive to also vary among the three galaxies. The largest spatial scales that can be observed by the interferometer depend on the shortest baselines. The three galaxies were observed with the most compact CARMA E configuration, for which the smallest baseline length is 66 m. The interferometer is sensitive to structures that are at most ~ 10 times the synthesized beam size. Therefore, the largest structures that can be recovered by the interferometer range from 850 pc (M 31) to 10 kpc (NGC 5055). In spite of such a large difference in the spatial scales, we measure 50% difference between single-dish and interferometric line widths for the three galaxies.

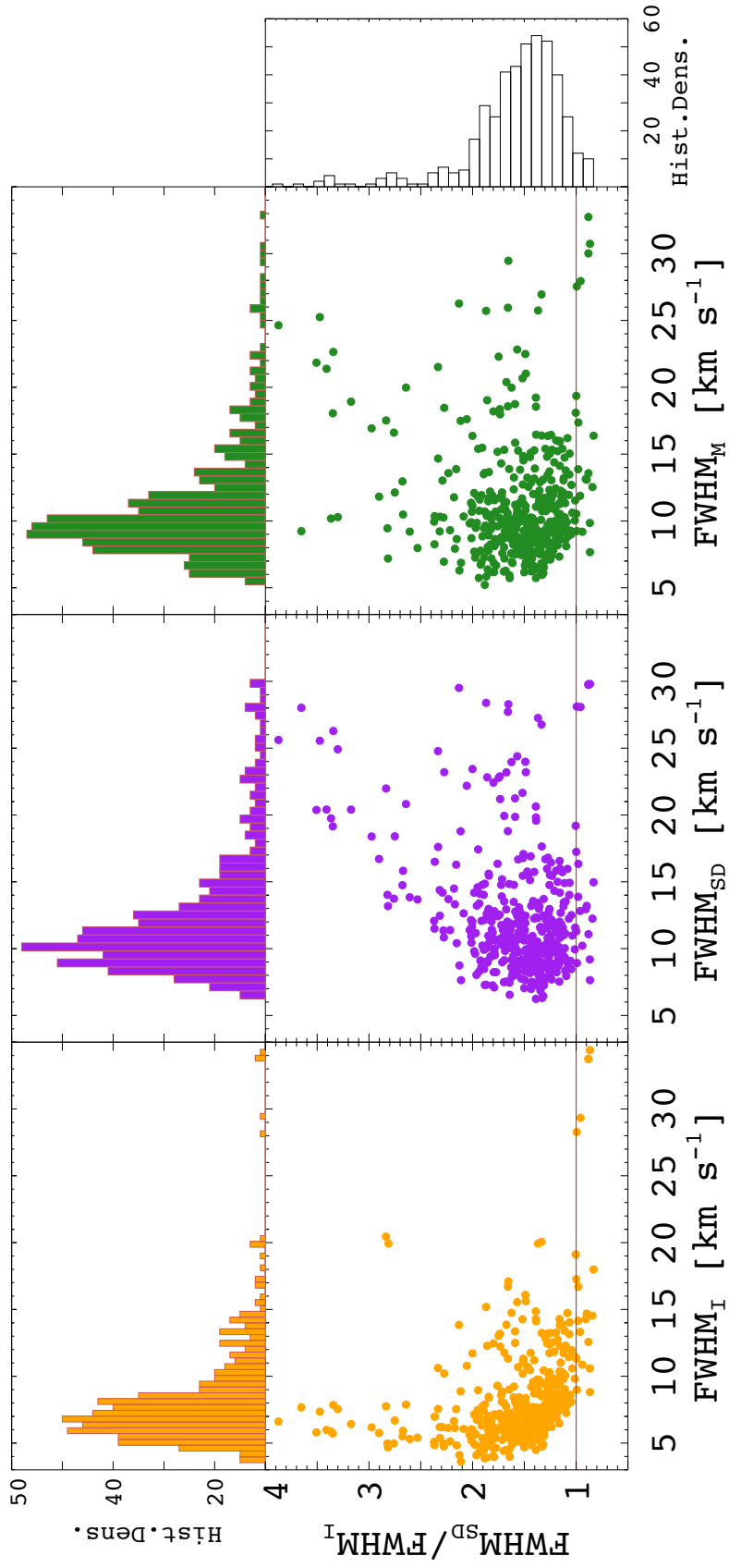

Figure 4.2 **CO FWHM in M31.** In this figure are plotted the ratio of the single-dish to interferometric FWHM ($FWHM_{SD}/FWHM_I$) as a function of FWHM measured for each of the three different CO data sets : interferometric data set (left, orange), single-dish data set (center, purple), and merged cube (right, green). The *x*-axis of each figure corresponds to the FWHM measured in each data set; while the *y*-axis is the same for the three, and corresponds to the ratio $FWHM_{SD}/FWHM_I$ values. The red line shows where the ratio is equal to one. On top of each plot we show the histograms with the distribution of FWHM measured on each data set. At the right hand side of the three plots we show a histogram of the $FWHM_{SD}/FWHM_I$ ratio values (black).

4.3.2 FWHM as function of SFR tracers

The next step is to investigate whether there is a correlation between the measured FWHM and the different SFR tracers (FUV, Hα, and 24, 70, and 160 μm). A correlation (or a lack of it) would indicate how relevant star formation is, in terms of energy injection into the molecular phase of the ISM at the spatial scales corresponding to 23″ (85 pc, projected). In Figures 4.3 – 4.5 we show images of the different SFR tracers, overlaid by black contours showing their 50^{th} and 84^{th} percentiles. A red solid line shows the area observed by the CARMA survey of Andromeda (Schruba et al., in prep). The CO integrated intensity 84^{th} percentile (from the merged cube) is shown in blue contours. These figures already suggest that molecular gas emission is not necessarily spatially correlated with the distinct SFR tracers at this spatial scales (see for example the right bottom corner of Fig. 4.3, where Hα emission appears to anti correlate with CO emission), as has already been previously stated by e.g., Schruba et al. (2010); Kruijssen & Longmore (2014). The strongest correlation appears to be between PACS 160 μm emission and CO emission.

To test for a possible correlation between the SFR tracer's intensity with CO intensity, we construct 5 bins of increasing intensity for each SFR tracer. In each case, the bins have equal number of points. We select LOSs that belong to each bin, and calculate the median value of the CO integrated intensity measurements for each instrument, together with the median value of the corresponding SFR tracer's intensity. We show the results in Fig. 4.6. Within the uncertainties, CO integrated intensities do not seem to correlate with the corresponding FUV, Hα, and 70 μm intensities. This lack of correlation is not surprising at the spatial scales probed here. Different star formation tracers are sensitive to different timescales since star formation occurred. For example, the mean stellar age of stars contributing to FUV emission is 10 Myr, whereas Hα is more sensitive to a mean stellar age of 3 Myr (Hao et al. 2011). The infrared tracers are more sensitive to stellar ages that lie between the former two, 5 Myr (Rieke et al. 2009). However, it is important to emphasize that calculations of extragalactic star formation rates using these tracers have been calibrated for averaged luminosities over whole galaxies (e.g., Calzetti et al. 2010), or over large regions (sub-kilo-parsec scales) inside galaxies (Leroy et al. 2013). This averaging over large spatial scales translates into an averaging of distinct star forming regions at different evolutionary stages, i.e., it implies an averaging over time with regard to the star formation process. When moving to smaller scales, we start facing problems regarding the evolution of individual star forming regions, or of under-sampling of the initial mass function[4] (Leroy et al. 2013).

CO integrated intensities appear to have a positive correlation with 24 μm, and more clearly with 160 μm. As noted in the Introduction, this relation originates from the reprocessing of photons

[4]The initial mass function is a key parameter in the evolutionary synthesis models used to calibrate star formation tracers.

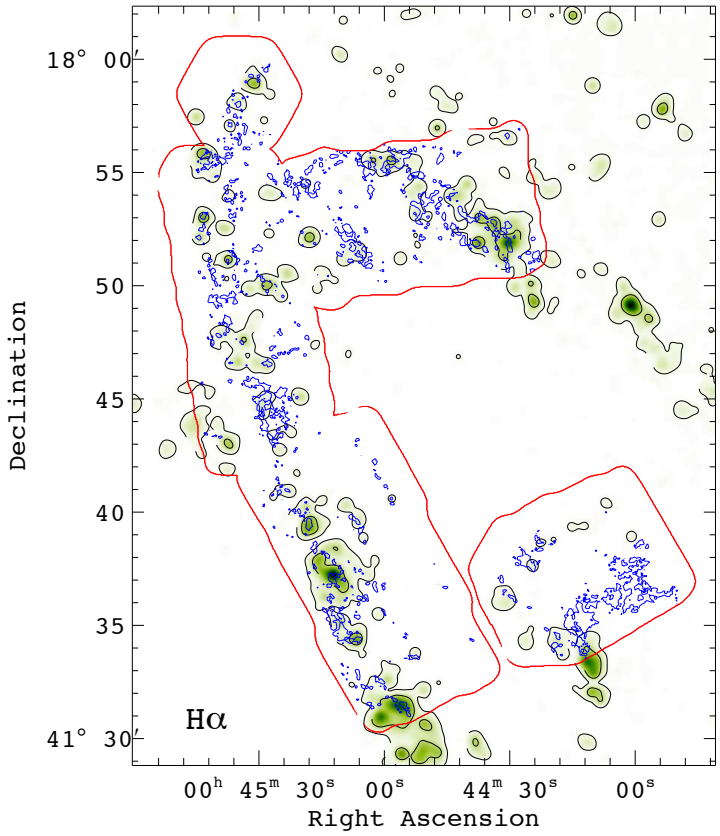

Figure 4.3 **M 31: Hα emission compared to CO emission.** Hα image at 23″ resolution overlaid by black contours showing its 50^{th} and 84^{th} percentiles. The red solid line shows the region observed by the CARMA survey of Andromeda (Schruba et al., in prep). The blue contours show the CO integrated intensity (from the merged cube) 84^{th} percentiles.

which are absorbed by dust particles, and then reemitted at longer wavelengths. The photons participating in this process may have different origins; a part is emitted by massive recently formed stars, and another fraction is emitted by an older stellar population, which does not trace recent star formation. Infrared emission at longer wavelengths has larger contributions from old stellar populations (Calzetti et al. 2010). Moving from shorter wavelengths (24 μm) to longer wavelengths (160 μm) involves moving from regions where star formation is contributing largely to the heating of dust, to regions where photons emitted by old stars become more important. Therefore, an interpretation of the relation we see between emission at 160 μm and CO integrated intensities might not be related to recent star formation at all. Nonetheless, the emission at 160 μm is tracing molecular gas. Molecular gas forms in regions where dust provides enough shielding agains energetic photons. Therefore, finding that dust spatially correlates to molecular gas complexes is expected.

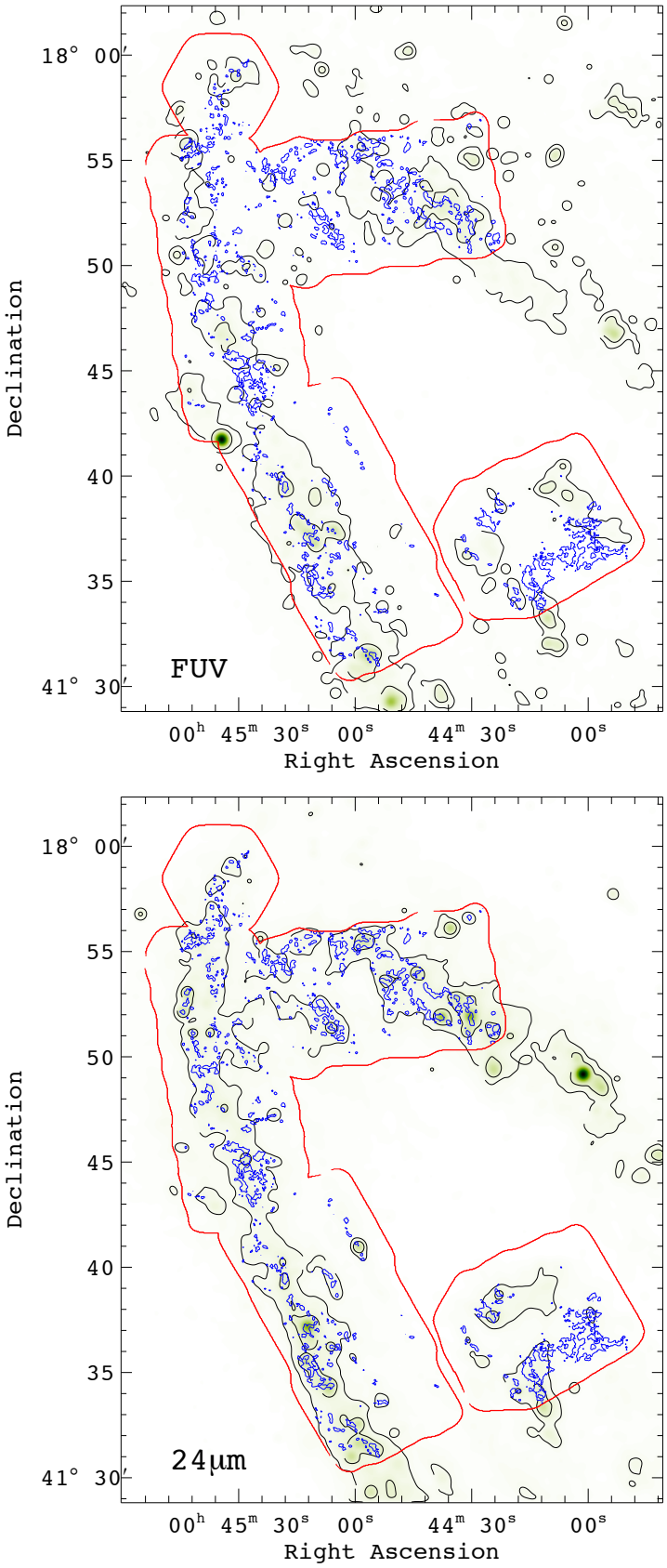

Figure 4.4 **M 31: GALEX FUV (top) and 24 μm (bottom) emission compared to** CO **emission.** Same as in Fig. 4.3.

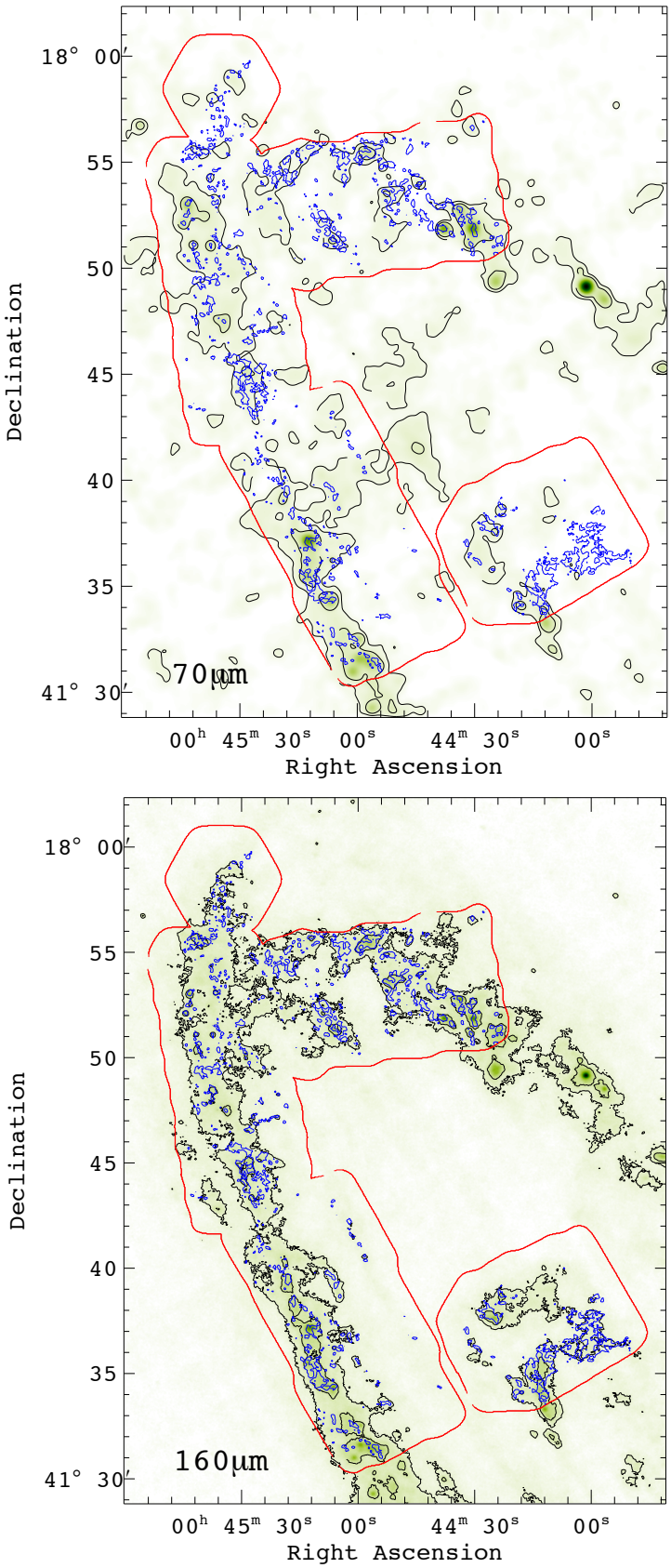

Figure 4.5 **M 31: PACS 70 μm and PACS 160 μm emission compared to** CO **emission.** Same as in Fig. 4.3.

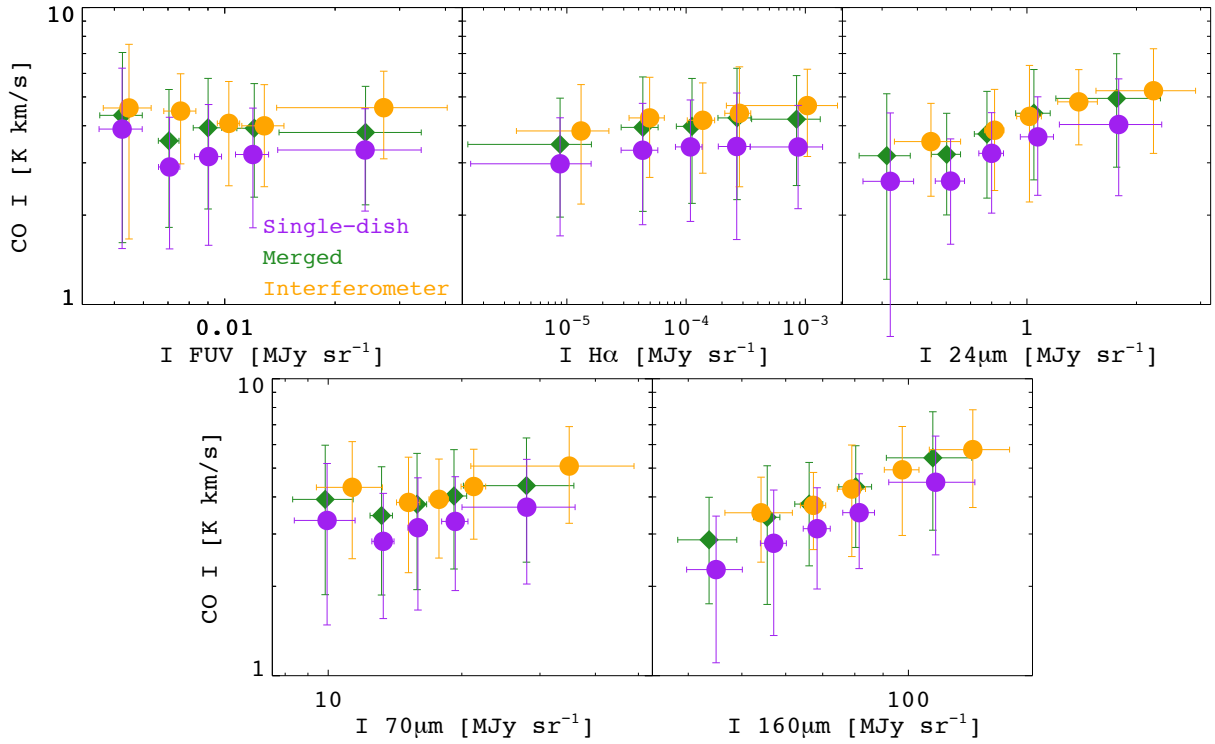

Figure 4.6 **CO integrated intensity as function of SFR tracers' intensities.** These plots show the relation between the CO integrated intensities measured for the different instruments (single-dish: purple; merged data: green; and interferometer: orange) as a function of the intensities measured for each SFR tracer (from top left to right bottom: FUV, Hα, MIPS 24 μm, PACS 70 μm, and PACS 160 μm). In each case, data is split in 5 bins of decreasing specific intensity of the corresponding SFR tracer. The bins are constructed to include equal number of points. We plot the median values of the CO integrated intensity within each bin, as a function of the median values of the specific intensity (I) of the corresponding SFR tracer within the same bin. The error bars represent the standard deviation of the individual LOSs for each bin.

In a similar way, we test for a correlation between CO line widths and SFR intensities. Using the same bins as before, we calculate the median value of the CO FWHM for each instrument, together with the median value of the corresponding SFR tracer intensity. The results are in Fig. 4.7. We do not find a significant correlation between the SFR tracers' median intensity values and CO FWHM for neither the interferometer, nor the single-dish data sets. Therefore, in a statistically robust way, we do not find evidence for star formation changing the molecular gas line widths (for single Gaussian line profile approximations) on spatial scales of ~ 85 pc. If the correlation is not present on these scales, it is likely not to be visible on larger scales either. This result is in agreement to the result we obtained in Chapter 2, where we did not find a correlation between SFR and FWHM (H I and CO) inside the optical radius of 12 galaxies at ~ 0.5 kpc resolution.

4.3.3 Molecular Gas: Two Components

In Fig. 4.7, the $\sim 50\%$ difference measured between FWHM from single-dish data and interferometric data is also clear. So far, the interpretation we have given is that this difference is due to a molecular gas component that is picked up by the single-dish but filtered out by the interferometer. This component would be characterized by larger FWHMs, as compared to those measured within GMCs. A way to test whether this is true or not, is to try to identify two components in the single-dish data. In order to quantitatively study differences between line profiles detected by the single-dish and interferometer, we proceed to stack the spectra of the LOSs analyzed individually (i.e., high S/N LOSs). To be able to stack, we first shift the spectra as described in Sec. 4.2.2. We decide to order the stacking by peak CO intensity measured in the interferometric data. In this way, even though we only have high S/N individual LOSs, the resulting stacked spectra will give us information on whether the spectral shape changes when going from lower peak intensities to higher peak intensities in the interferometric data. The dynamic range of the peak CO intensities of the individual LOSs goes from ~ 0.2 K to ~ 1 K. Following the previous section, we define 5 bins of increasing interferometric CO peak intensities, all of them with equal number of LOSs. The median values of the interferometric peak intensities resulting for each bin are: 0.24 K, 0.30 K, 0.36 K, 0.42 K, and 0.59 K. After the data is binned by the interferometric peak intensities, we proceed to stack the spectra (single-dish and interferometric spectra independently) from the individual LOSs within each bin.

The next step is to identify the different components that constitute the resulting stacked spectra. The idea is to fit two Gaussian components to the stacked spectra of the single-dish data and to the stacked spectra of the interferometric data, and quantify how significant the second component

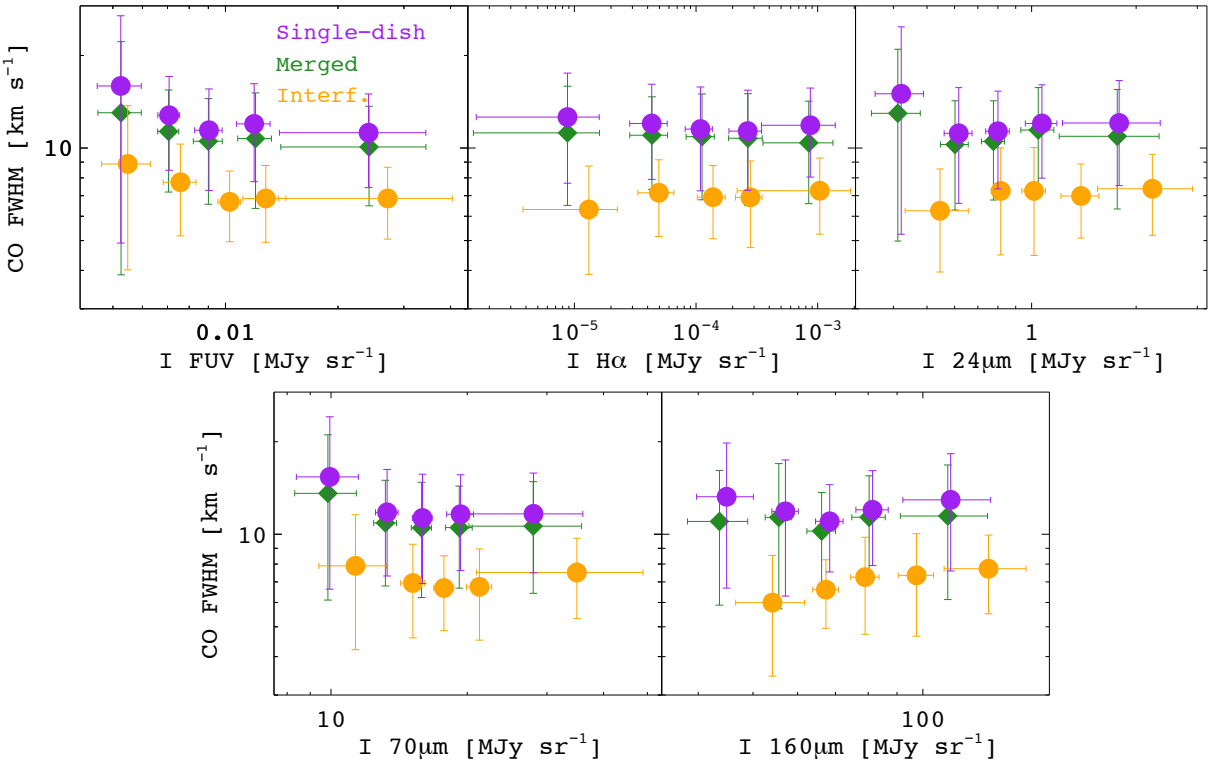

Figure 4.7 **CO FWHM as function of SFR tracers' intensity.** These plots show the relation between the CO FWHM measured for the different instruments (single-dish: purple; merged data: green; and interferometer: orange) as a function of the intensities measured for each SFR tracer (from top left to right bottom: FUV, Hα, MIPS 24 μm, PACS 70 μm, and PACS 160 μm). In each case, data is split in 5 bins of decreasing specific intensity of the corresponding SFR tracer. The bins are constructed to include equal number of points. We plot the median values of the CO FWHM within each bin, as a function of the median values of the specific intensity (I) of the corresponding SFR tracer within the same bin. The error bars represent the standard deviation of the individual LOSs for each bin.

is in each case. Even thought this has not yet been proven, for simplicity, we will refer to the two components as *narrow* (N) and *broad* (B). The two components would then be represented by:

$$I_i(v) = \frac{\mathrm{Peak_i}}{\sqrt{2\pi}\sigma_\mathrm{i}} \exp\left(-\frac{(\mathrm{v}-\mathrm{v_i})^2}{2\,\sigma_\mathrm{i}^2}\right) \tag{4.1}$$

where i stands for N (narrow component) or B (broad component), v is the velocity, and for each i component, I_i is the CO intensity, Peak_i is the Gaussian's amplitude, v_i is the velocity corresponding to the center of the Gaussian, and σ_i is the velocity dispersion (for which $\mathrm{FWHM}_i = 2\sqrt{2\ln 2}\,\sigma_i$).

There are 6 free parameters: 2 line centers ($\mathrm{v_N}$ and $\mathrm{v_B}$), 2 line widths ($\mathrm{FWHM_N}$ and $\mathrm{FWHM_B}$), and 2 peak amplitudes ($\mathrm{Peak_N}$ and $\mathrm{Peak_B}$). For simplicity, we fix the line centers of both components to 0 km s^{-1}. Since we use the peak velocity to shift the individual LOSs before stacking, the stacked spectra actually peak at zero velocity. We have four free parameters left. For the following analysis, we will assume (and later prove) that fitting a single Gaussian to the interferometric stacked spectra yields a good representation of the *narrow* component. We therefore fit, for each bin of the interferometric stacked spectra, a single Gaussian. We use the least squares fitting procedure `MPFIT` (IDL procedure from Markwardt 2009). To test whether the single Gaussian provides for a good description of the narrow component, for each bin and for both data sets (single-dish and interferometer), we fix $\mathrm{FWHM_N}$ to the value obtained from this single Gaussian fit. We then have three free parameters left: the line width of the broad component ($\mathrm{FWHM_B}$), and the two peak amplitudes, narrow ($\mathrm{Peak_N}$) and broad ($\mathrm{Peak_B}$). We construct a grid of values for $\mathrm{FWHM_B}$ going from 6 km s^{-1} to 25 km s^{-1} in steps of 0.05 km s^{-1}, and for $\mathrm{Peak_N}$ going from 0 K to 0.7 K in steps of 5×10^{-3} K. For each point on the grid, we proceed to do a least squares fitting using `MPFIT`, leaving $\mathrm{Peak_B}$ as a free parameter. For each point in this 3-D parameter space we compute the reduced chi-squared (R-χ^2) value. The best-fit parameters are selected by taking the minimum R-χ^2 value from the 3-D parameter space.

The results are presented in Figures 4.8 and 4.9, for the interferometer and single-dish, respectively. The five rows correspond to the five bins used to stack the spectra, with the lowest interferometric peak intensity on the top. On the left panel of each figure, we show the 1-, 2-, 3-, and 4-σ R-χ^2 contours (red, yellow, green, and white). The minimum R-χ^2 value is marked with a cyan star symbol. On the right panel we show the stacked spectrum of each bin. It is over plotted with the two Gaussian components (narrow in blue, and broad in red) obtained from the best-fit parameters.

Once this is done, we repeat the exercise, but now fixing $\mathrm{FWHM_B}$. In this case, we take the $\mathrm{FWHM_B}$ best-fit value for each bin (and for each instrument) obtained previously, and test whether we recover the original $\mathrm{FWHM_N}$ values. Now the three free parameters are: line width

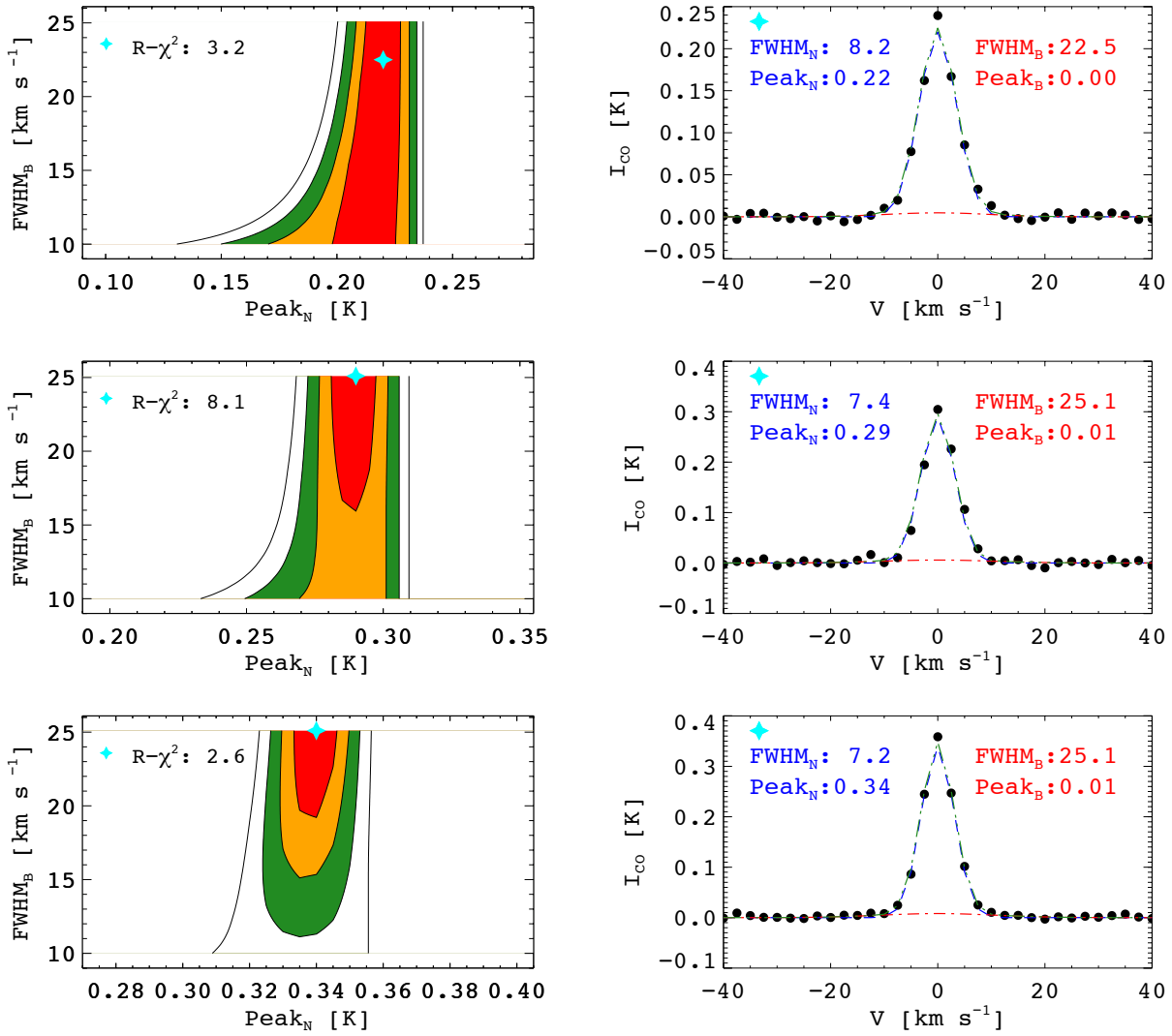

Figure 4.8 **Interferometric data: Reduced χ^2 contours when fixing FWHM$_N$ and best-fit solution.** From top to bottom we show the results corresponding to the five bins used to stack the spectra. The top row corresponds to the lowest interferometric peak intensity, with peak intensity increasing downwards. On the left column are the 1-, 2-, 3-, and 4-σ R-χ^2 contours (red, yellow, green, and white). The contours are shown as a function of Peak$_N$ on the x-axis and FWHM$_B$ on the y-axis. Peak$_B$, for which the fit has been optimized, is not shown. The cyan star shows the location of the best-fit parameters which minimize R-χ^2. On the right column, we plot the stacked spectra corresponding to each of the five bins. Over plotted are the two Gaussian components (narrow in blue, and broad in red) resulting from the best-fit parameters. The green line shows the combination of both components. We indicate the best-fit parameter values of the two components: narrow (top left, blue) and broad (top right, red).

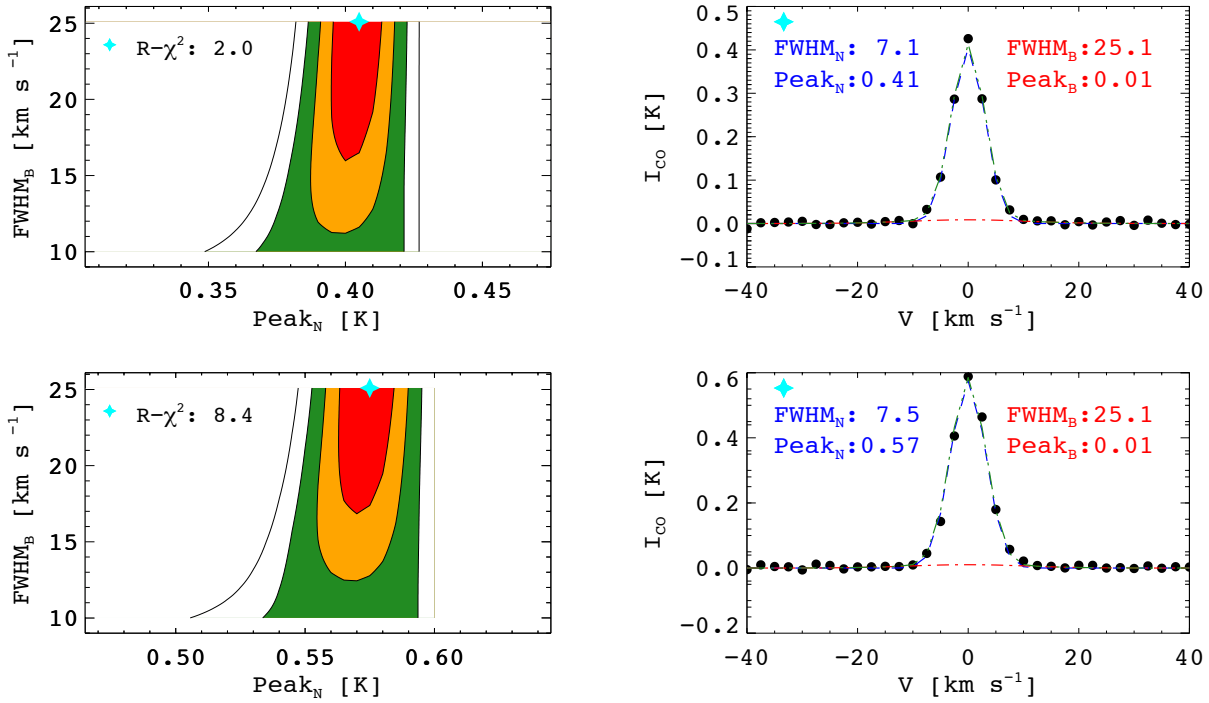

Figure 4.8 continued.

of the narrow component ($FWHM_N$), and the two peak amplitudes, narrow ($Peak_N$) and broad ($Peak_B$). We construct a grid of values for the $FWHM_N$ going from 6 km s^{-1} to 25 km s^{-1} in steps of 0.05 km s^{-1}, and for the $Peak_B$ going from 0 K to 0.7 K in steps 5×10^{-3} K. Again, we determine the best-fit for each point on the grid, now leaving $Peak_N$ as a free parameter. The results, analogous to the previous case, are shown in Figures 4.10 (interferometer) and 4.11 (single-dish). The best-fit values found for $FWHM_N$ (mean value of 7.5 ± 0.4 km s^{-1}) agree in all cases, within the uncertainties, to the values obtained by a single Gaussian fit to the interferometric data (mean value of 7.1 ± 0.4 km s^{-1}). This confirms that taking the single Gaussian fit of the interferometric data as being representative of the narrow component is a valid assumption.

As is already apparent from Figure 4.8, fitting two components to the interferometric data do not yield well constrained results on the R-χ^2 contours. To quantitatively test whether adding an extra component to the description of the data is significant or not, we perform an F-distribution test. The null hypothesis of this test is that the simpler model (model 1), which is nested in a more complicated model (model 2), is the correct one. In our case, "model 1" would be fitting a single Gaussian (2 free parameters, taking into account that the line center is fixed), and "model 2" would be fitting two Gaussians (3 free parameters, as the two line centers and one line width are fixed). By default, the model with more free parameters gives a lower χ^2 value; therefore, it

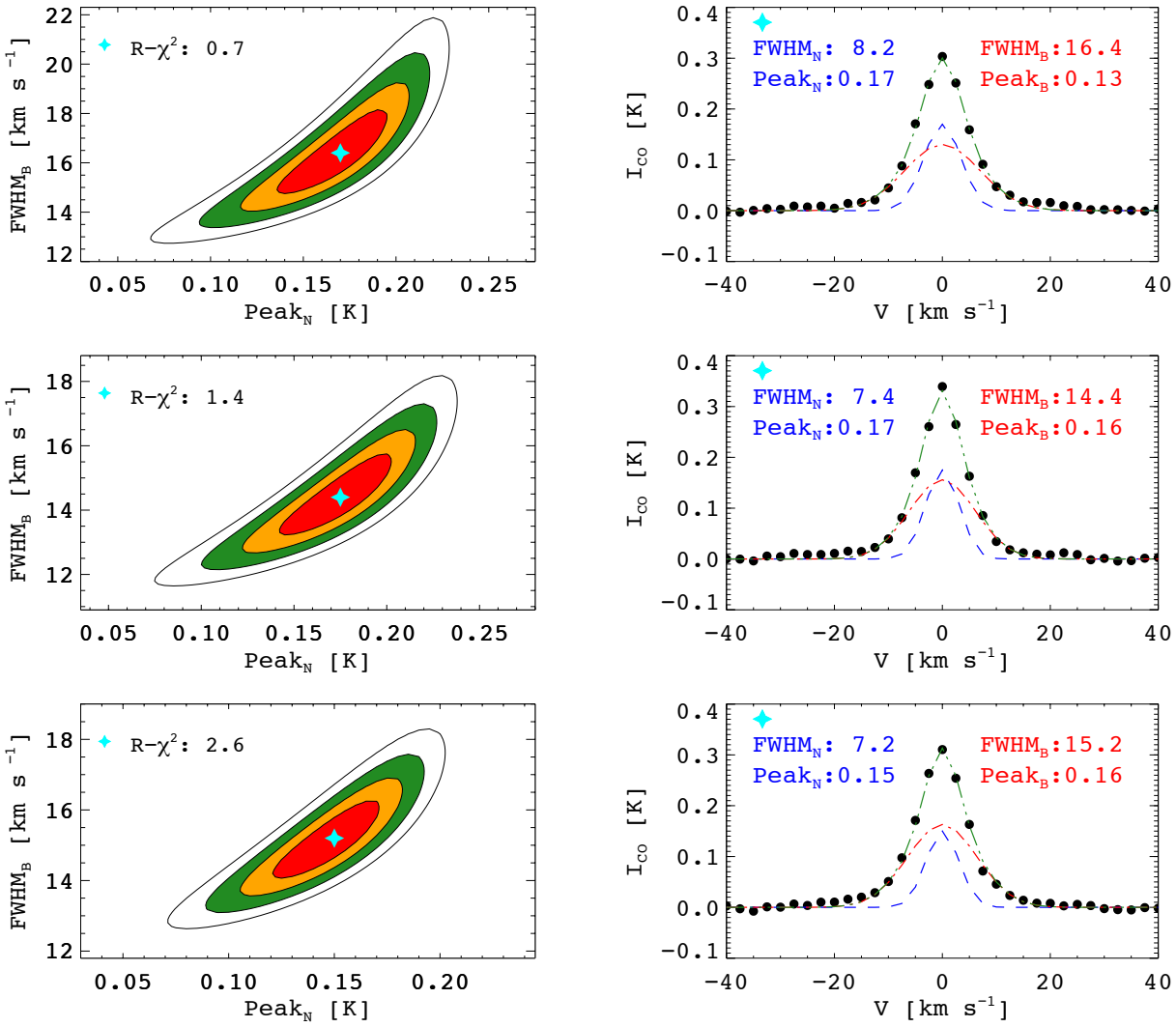

Figure 4.9 **Single-dish data: Reduced χ^2 contours when fixing FWHM$_N$ and best-fit solution.** Same as in Fig. 4.8.

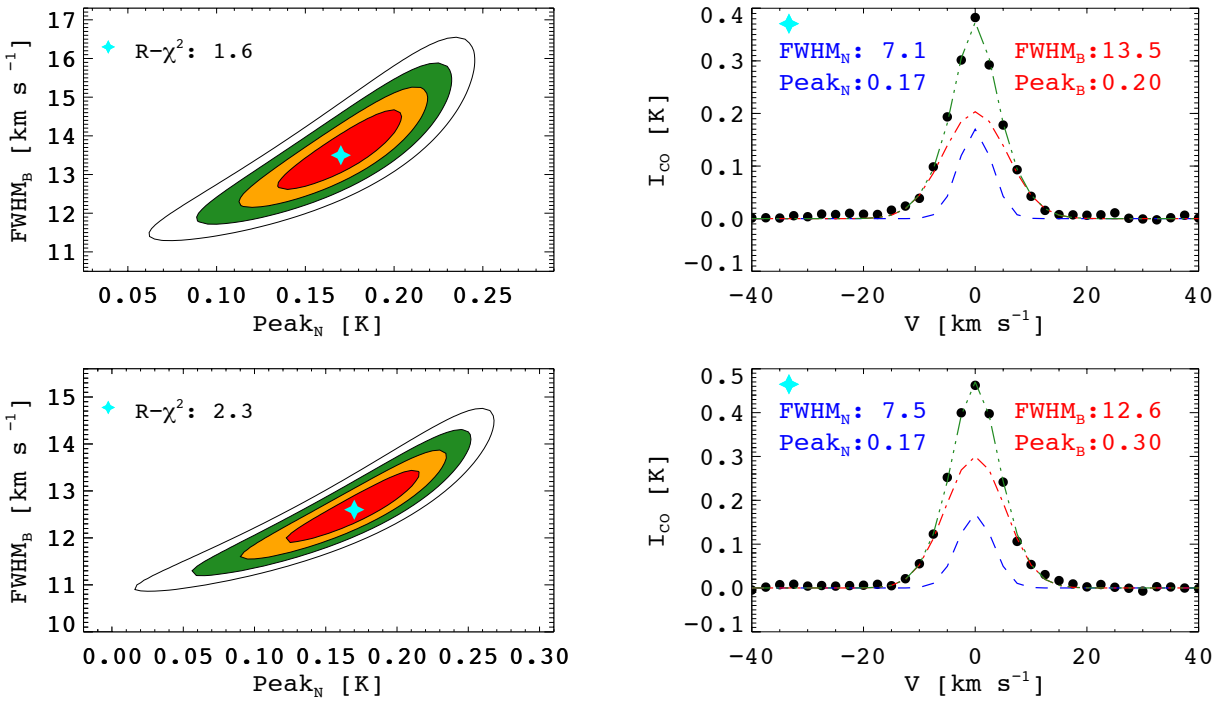

Figure 4.9 continued.

is important to test how significant this improvement is. To carry out the F-distribution test, an F-value has to be computed. The F-value is defined as:

$$F = \frac{\frac{RSS_1 - RSS_2}{dof_1 - dof_2}}{\frac{RSS_2}{dof_2}} \tag{4.2}$$

where RSS_i is the residual sum of squares of model i, and dof_i is the number of degrees of freedom of model i. If the calculated F-value results larger than the F-critical value, then there is statistical significance to reject the null hypothesis. The calculation of the F-critical value depends on the choice of a significance level α. The commonly used $\alpha = 0.05$ implies that the null hypothesis is rejected 5% of the times when it is actually true. An $\alpha = 0.05$ significance, for the combination of 2 and 3 free parameters in the two models (our case), yields a critical F-value of 9.55. Therefore, when the computed F-value is larger than 9.55, fitting two Gaussians provides a significantly better description of the data.

To understand the significance of fitting two Gaussian components to the different data sets, we compare in Figures 4.12 and 4.13 (for interferometric and single-dish data, respectively) the values obtained from the minimum R-χ^2 parameters when fixing $\mathrm{FWHM_N}$, together with the F-values obtained for each case. In each figure we show the results for the narrow component

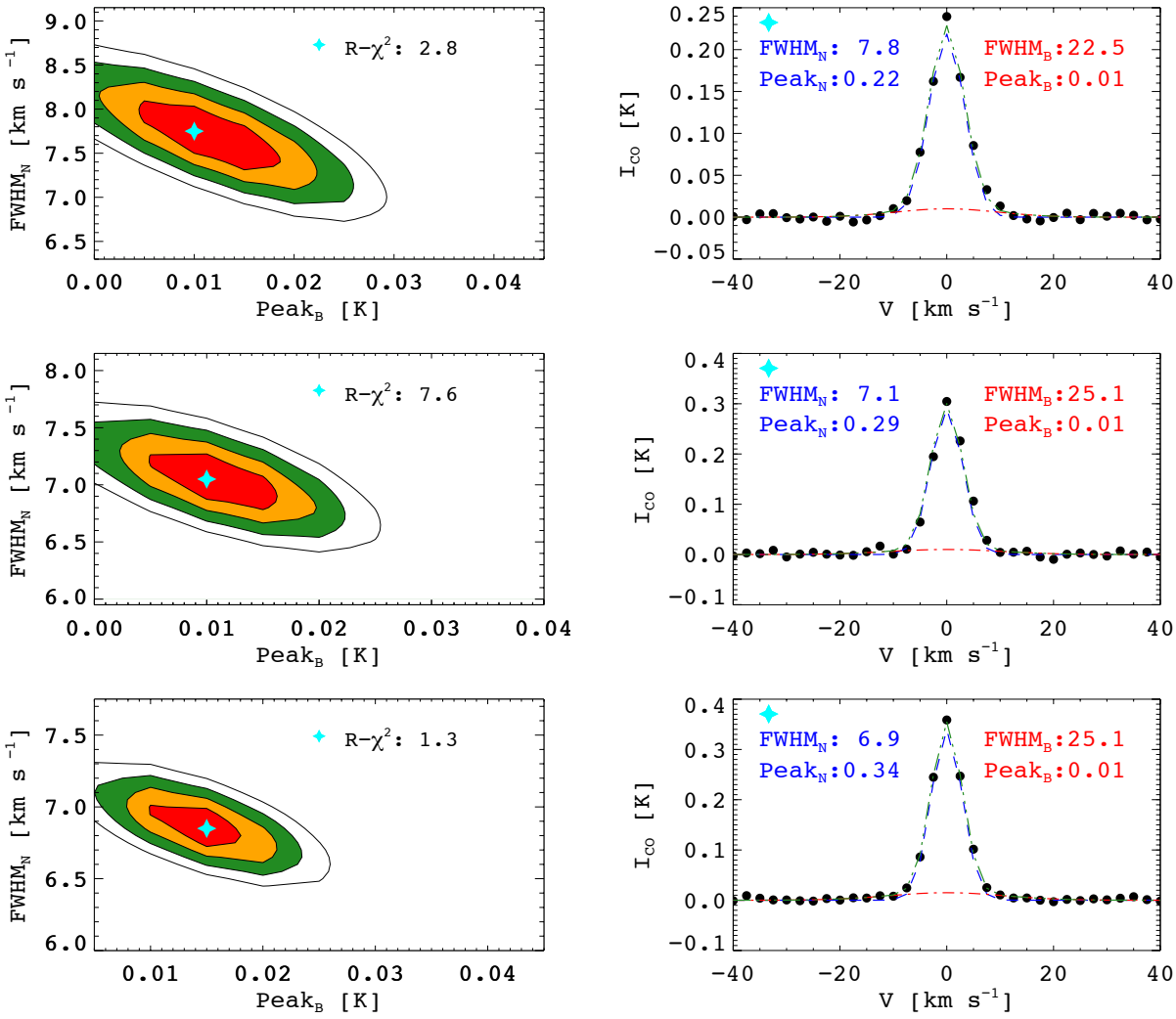

Figure 4.10 **Interferometric data: Reduced χ^2 contours when fixing FWHM$_B$ and best-fit solution.** From top to bottom we show the results corresponding to the five bins used to stack the spectra. The top row corresponds to the lowest interferometric peak intensity, with peak intensity increasing downwards. On the left column are the 1-, 2-, 3-, and 4-σ R-χ^2 contours (red, yellow, green, and white). The contours are shown as a function of Peak$_B$ on the x-axis and FWHM$_N$ on the y-axis. Peak$_N$, for which the fit has been optimized, is not shown. The cyan star shows the location of the best-fit parameters which minimize R-χ^2. On the right column, we plot the stacked spectra corresponding to each of the five bins. Over plotted are the two Gaussian components (narrow in blue, and broad in red) resulting from the best-fit parameters. The green line shows the combination of both components. We indicate the best-fit parameter values of the two components: narrow (top left, blue) and broad (top right, red).

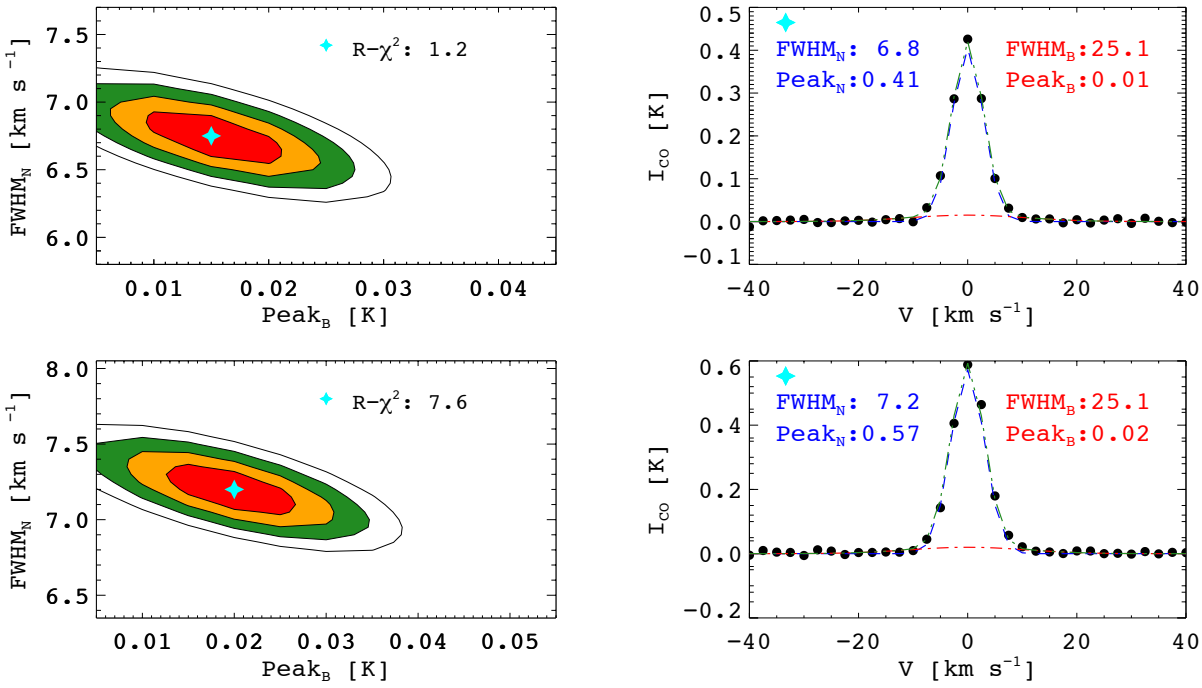

Figure 4.10 continued.

on the left panel, and the results for the broad component on the right panel. The parameters obtained from the best-fit values are from top to bottom: line width ($\mathrm{FWHM_i}$), peak amplitude (Peak_i) , ratio of peak amplitude to the peak of the spectrum (Peak_i/Peak spectrum), and ratio of the integrated flux over the fit to the integrated line flux (Flux_i/Flux Spectrum). The y-axis has a subscript i, which in the left column corresponds to i = N (narrow component), and in the right column it corresponds to i = B (broad component). The error bars are taken from the 1σ contours. On top of the figure we show, for each bin, the corresponding minimum R-χ^2 value (left column) and F-test value (right column).

Figures 4.12 and 4.13 show quantitatively different behaviors. The interferometric data (Fig. 4.12) shows a flat distribution of the FWHM values (first row) measured for both the narrow and broad components. The mean value of the FWHMs measured for the narrow component is 7.5 km s^{-1} with a standard deviation among measurements of the five bins of 0.4 km s^{-1}. The broad component has a FWHM mean value of 24.6 ± 1.1 km s^{-1}. The contribution of the broad component to the total line fit results, however, negligible. The mean value of the ratio between the broad peak intensity to the line peak intensity (row 3, right panel) is $\mathrm{Peak_B/Peak_{spec}} = 0.019 \pm 0.002$. This result is also seen for the ratio of the flux measured in the broad component compared to the flux measured in the line (fourth row, right panel), which has a mean value of $\mathrm{Flux_B/Flux_{spec}} = 0.06 \pm 0.01$. The narrow component therefore accounts for $\sim 94\%$ of the total line flux. The F-values calcu-

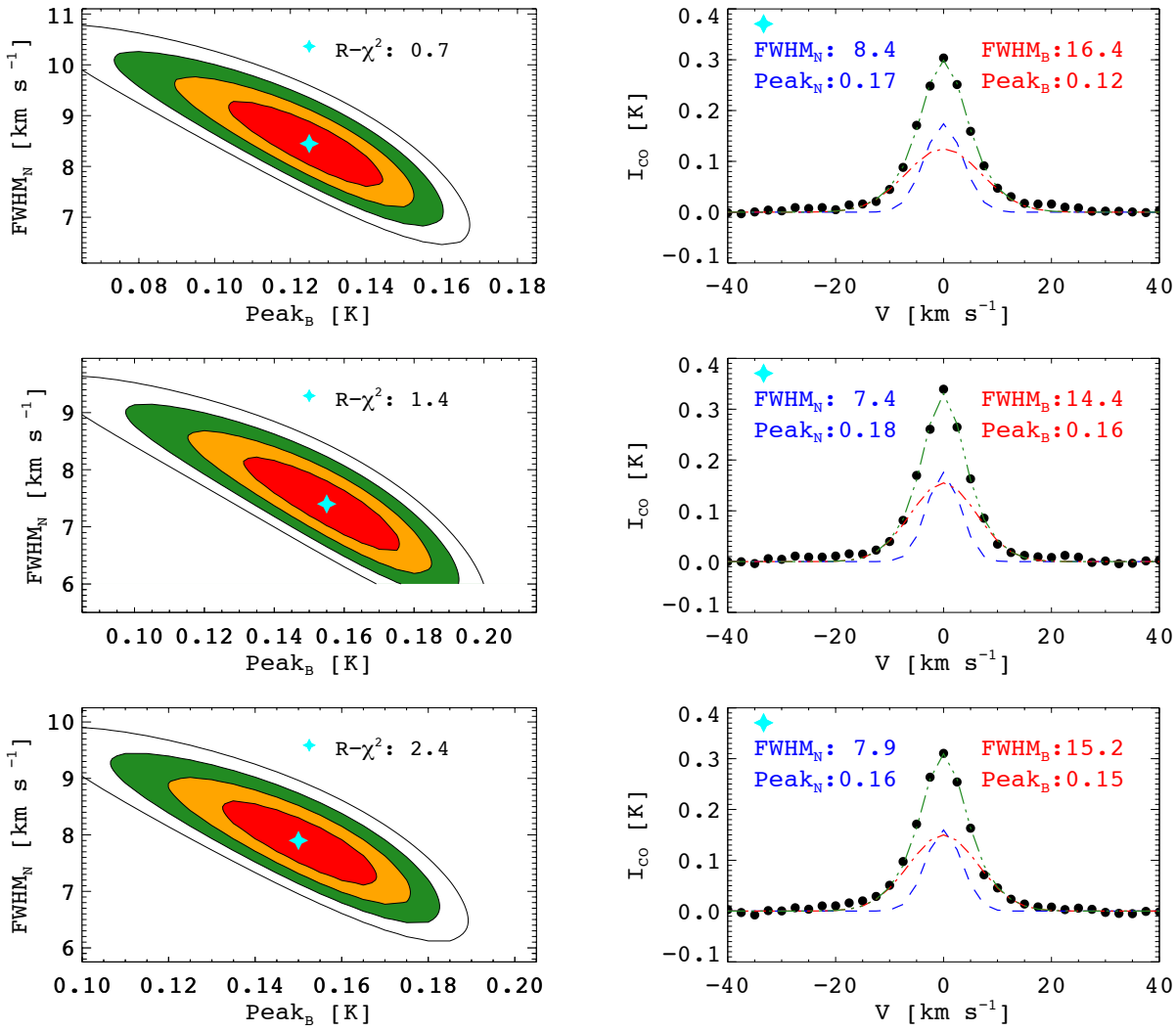

Figure 4.11 **Single-dish data: Reduced χ^2 contours when fixing $FWHM_B$ and best-fit solution.** Same as in Fig. 4.10.

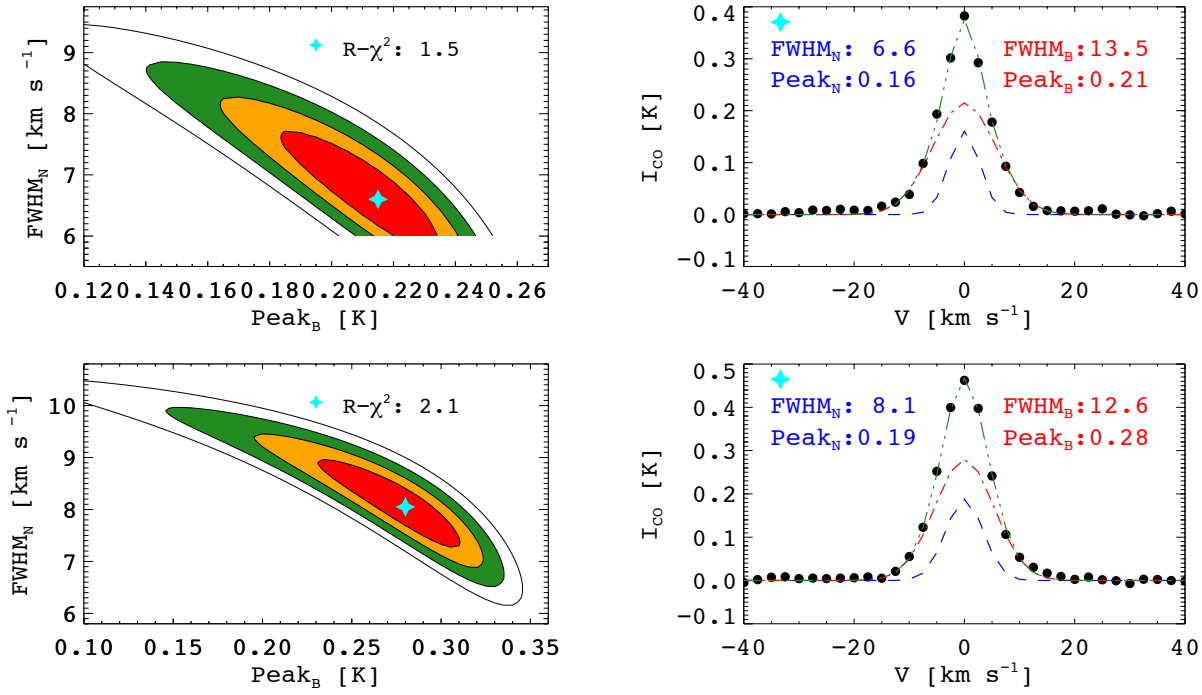

Figure 4.11 continued.

lated for the five bins range from 0.9 to 5.9; in all cases clearly below the F-critical value of 9.55. Adding a second component to describe the interferometric data is not justified. The narrow component dominates the emission.

The results from the single-dish data are contrasting (Fig. 4.13). The FWHMs of the narrow component have a mean value of 7.5 ± 0.4 km s^{-1} (first row, left panel). The FWHMs of the broad component are larger than the ones computed for the interferometric case. They have a mean value of 14.4 ± 1.5 km s^{-1}(first row, right panel). Moreover, the broad components becomes narrower by $\sim 30\%$ when going from the bin of lowest peak intensity in the interferometric data (Bin 1) to the bin of highest peak intensity in the interferometric data (Bin 5). The peak intensity of the narrow component shows a flat distribution with a mean value of 0.17 ± 0.01 K (second row, left). The broad component's peak intensity distribution, however, is not flat, as it increases from 0.13 K to 0.30 K when going from Bin 1 to Bin 5. On the third row it becomes clear what is happening. The narrow component contributes less to the line intensity when going from Bin 1 to Bin 5. The contrary happens to the broad component, which becomes more significant. The relative contribution of the narrow component's peak intensity to the total peak intensity varies from $\sim 56\%$ to $\sim 37\%$; while the broad component's peak intensity contribution varies from $\sim 43\%$ to $\sim 65\%$. The same trend is observed in the fourth row, where we see that the

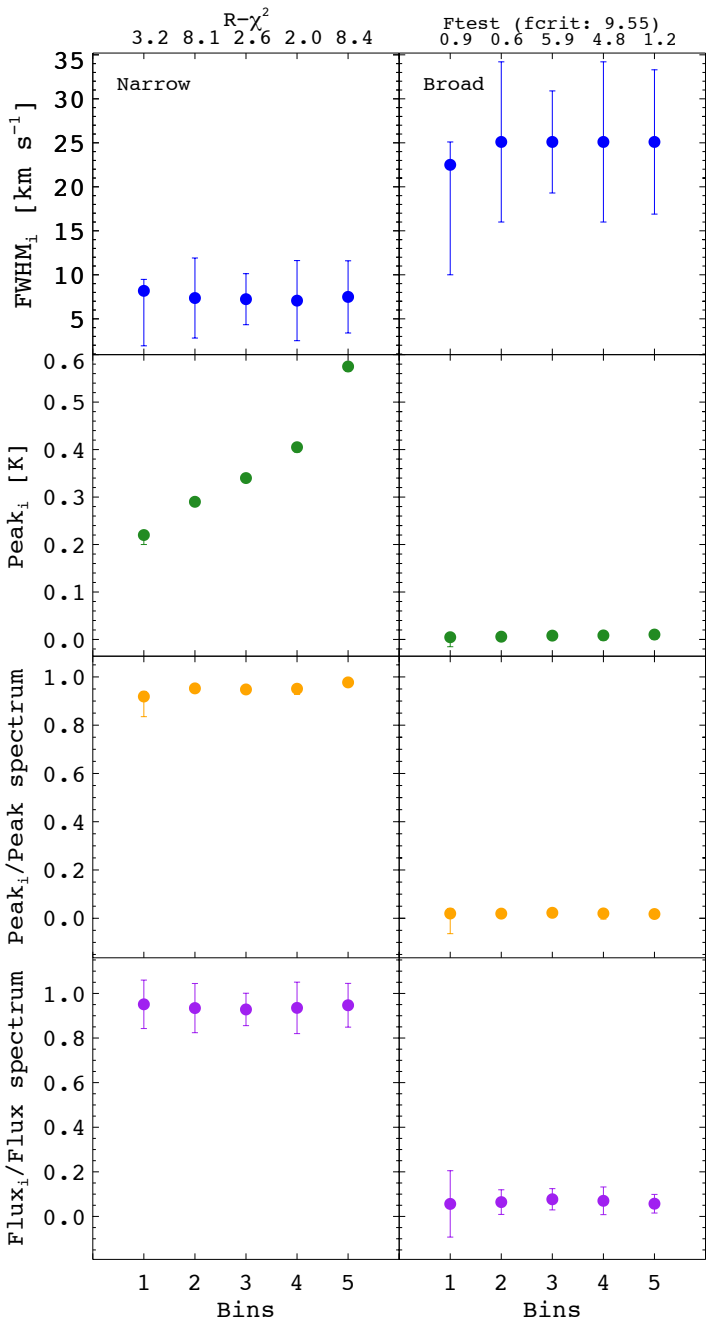

Figure 4.12 **Interferometric data: Properties of the best-fit values obtained for the double Gaussian fit.** The parameters derived by the minimum R-χ^2 from the two Gaussian fit are plotted as a function of bin. From top to bottom these parameters are: line width (FWHM$_i$), peak amplitude from the fit (Peak$_i$) , ratio of peak amplitude from the fit to the peak of the spectrum (Peak$_i$/Peak spectrum), and ratio of the integrated flux over the fit to the integrated line flux (Flux$_i$/Flux Spectrum). The y-axis has a subscript i, which on the left column corresponds to i = N (narrow component), and on the right column corresponds to i = B (broad component). The error bars are taken from the 1σ contours. On top of the figure we show for each bin the minimum R-χ^2 value (left column) and the F-test value (right column).

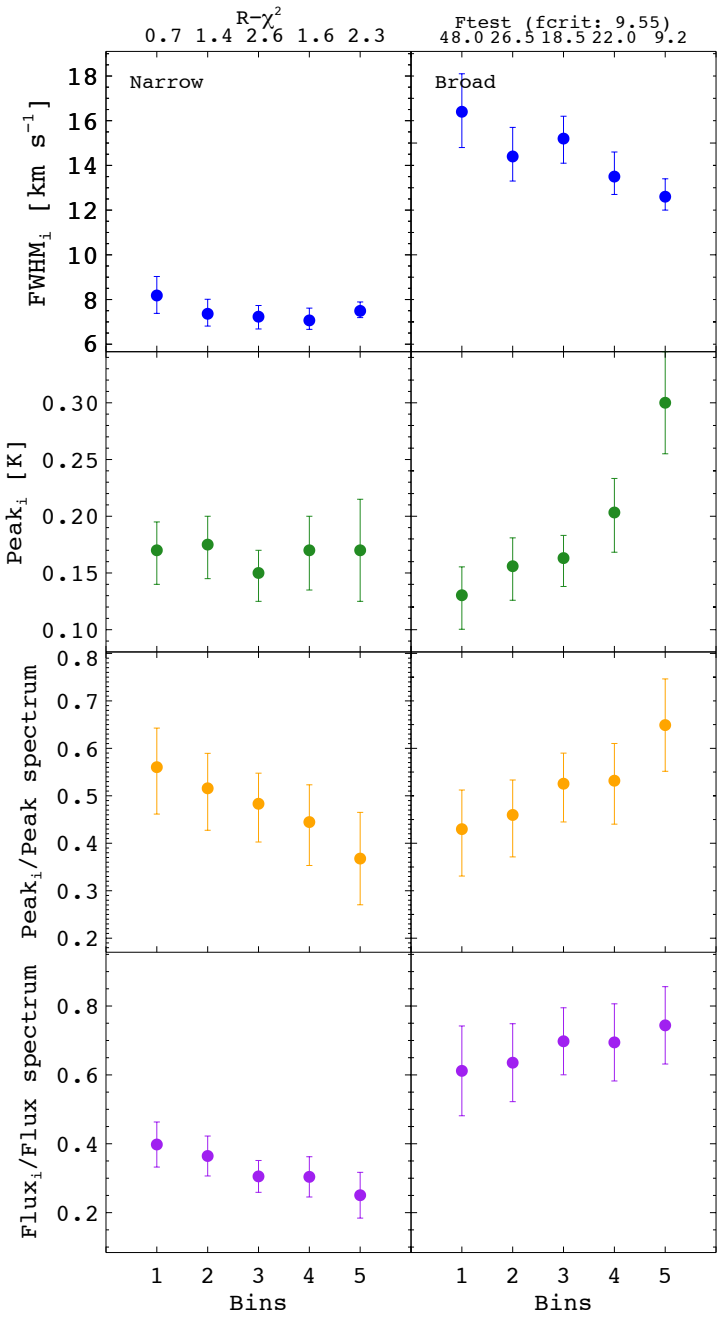

Figure 4.13 **Single-dish data: Properties of best-fit values obtained for the double Gaussian fit.** Same as in Fig. 4.12.

Table 4.1. Percentage of flux contained in each bin compared to the total flux within the five bins

Bin	1	2	3	4	5
% Flux, merged data	14	16	19	21	30
% Flux, single-dish data	19	19	19	20	24

narrow component's contribution to the line flux varies from ∼40% to ∼25%, and the broad component's flux contribution varies from ∼61% to ∼74%.

At first glance this result may seem counterintuitive. As we move from the bin with lowest peak intensity in the interferometric data to the bin with highest peak intensity in the interferometric data, it looks like the narrow component becomes less important. To understand what is happening, we need more information. If we look at the F-values computed for the single-dish data we notice that for the first 4 bins, the values are larger than the F-critical value of 9.55, however, the F-value decreases as a function of bin. This means that, even though fitting a second component provides a significantly better description of the data, it becomes less significant as we move to higher peak intensity values of the interferometric data. This trend continues to Bin 5, where the F-value becomes actually marginally smaller than the F-critical value. If we look at the left panel of Fig. 4.9, we see that the broad component changes from being a truly broader component to simply be a component that resembles the narrow one.

A possible interpretation for these results is that as we move to bins of higher peak intensities in the interferometric data, we are probing molecular gas which is sitting on top of GMCs. In Table 4.1, we show the percentage of flux contained in the LOSs belonging to each bin, as compared to the flux of the LOSs belonging to the five bins altogether. We measure the flux from the integrated intensity maps (0^{th} moment maps) obtained from the merged data set (first row in table) and from the single-dish data set (second row in table). The flux within a bin measured from the merged cube increases two times when going from Bin 1 to Bin 5. The flux measured from single-dish data remains constant on the first four bins, and increases by ∼25% on the last bin. This reinforces the idea that LOSs in the last bin are probing compact emission arising from GMCs. Therefore, even the single-dish data will be dominated by the emission arising from molecular clouds, and distinguishing the broad component becomes more challenging.

4.4 Conclusions

Analyzing molecular gas at high spatial resolution and sensitivity allow us characterize its nature in a more constrained way. As a first result, we find single-dish data line widths that are $\sim 50\%$ larger than those measured from interferometric data. This result is in agreement to what we previously measured for NGC 4736 and NGC 5055, in spite of probing different spatial scales.

Owing to the high quality of the data, in this study we are able to characterize line profiles arising from both instruments by means of stacking individual LOSs. We find strong evidence pointing to the existence of two components contributing to single-dish spectra: a narrow component of $\mathrm{FWHM_N} \sim 7.5 \pm 0.4\,\mathrm{km\,s^{-1}}$ and a broad component of $\mathrm{FWHM_B} \sim 14.4 \pm 1.5\,\mathrm{km\,s^{-1}}$. We also show that interferometric data is sufficiently well described by a single Gaussian fit with $\mathrm{FWHM} \sim 7.1 \pm 0.4\,\mathrm{km\,s^{-1}}$.

A thorough characterization of line profiles requires high S / N data. In this project we limited our study to LOSs with peak S / N larger than 5 (corresponding to ~ 0.2 K). With this sensitivity cut, we keep only $\sim 5\%$ of the total number of LOSs (which, however, make up to 25% of the total flux). The main reason why we cannot work with the rest of the lower S / N LOSs, is because we have no robust information on the intensity weighted mean velocity by which we need to shift them. The next step, to better study the presence and properties of the broad component, is to move to lower S / N regions. We expect that in these regions, where the bulk of CO emission is not stemming from the molecular cloud, the broad component will become more dominant within the overall spectrum.

CHAPTER 5

SUMMARY AND OUTLOOK

The results presented in this work reinforce a scenario in which molecular gas emission in nearby galaxies is described by two distinct components: one that is clumpy and organized as molecular clouds, and another one that is more diffuse and with larger velocity dispersions. The importance of this result resides in the fact that in order to characterize the physical conditions of the interstellar medium, it is essential to have information about the energy balance between the different phases that constitute it. This energy balance results from complex radiative, thermal, chemical, and kinematic processes which take place in large scale structures within galaxies. Since a detailed balance of all these processes is very complex, observational studies are required to place constraints on the modeling of such an elaborate system. The observational results obtained in this work call in question the classical picture of the interstellar medium, where molecular gas is thought to be organized mostly inside giant molecular clouds, typically traced by CO emission, with temperatures of $10-20$ K and internal velocity dispersions of $\sim 2-8$ km s^{-1} (e.g., Solomon et al. 1987).

Observations of diffuse molecular gas, traced by CO emission, are not new. Previous *galactic* studies have already shown, that this type of emission is pervasive within our Galaxy (Polk et al. 1988; Liszt & Lucas 1998; Goldsmith et al. 2008, and references therein). However, our disadvantageous view point within the Galaxy makes it difficult to quantify the amount of gas present in this diffuse molecular component, due to projection effects and uncertainties in distance determinations. As an alternative, nearby galaxies offer the possibility to study the presence of this

component from an 'outside' perspective. The problem with nearby galaxies is that high spatial resolution measurements of molecular gas are more difficult to achieve. Novel developments in instrumentation for radio telescopes, both single-dish and interferometers, have enabled the study of molecular gas composition in larger samples of galaxies, and in greater detail. New observations have nourished the discussion of the presence of a 'diffuse' molecular gas component within spiral galaxies.

As stated before, understanding the physical properties of the interstellar medium goes hand in hand with understanding key physical processes that govern the energy and mass balance between its phases. Our insight on the star formation process, for example, largely relies on the estimates of the amount of gas which is being converted into stars. It is typically (implicitly) assumed that the observed molecular gas is a direct reservoir for star formation, for example, in computations of depletion times (e.g., Krumholz et al. 2012; Leroy et al. 2013). The existence of a diffuse component, that is not necessarily directly involved in the current star formation process, would imply an underestimation of star formation efficiencies calculated under the aforementioned assumption. This consequently would modify the shape of the "star formation law" and feedback processes included in current models of galaxy formation (e.g., Somerville & Davé 2014). Therefore, constraining the physical properties regulating the molecular gas phase may yield fundamental information to understand the underlying physics that govern the cycle between gas and stars, and ultimately the evolution of galaxies.

5.1 Summary

In this thesis I present results starting from a more general point of view, comparing H I and CO velocity dispersions on scales of half a kilo parsec, then moving to higher resolution, reaching molecular cloud scales, and focusing on molecular gas only.

I started comparing line widths of neutral atomic and molecular gas measured inside the optical radii of a sample of 12 nearby galaxies on 0.5 kpc scales. To quantify velocity dispersions robustly, we performed stacking of individual spectra. The binning of the individual spectra prior to stacking was based on physical properties, such as galactocentric distance or SFR surface density. The velocity dispersions were measured by fitting a single Gaussian to the resulting stacked spectra. This project led to two main results:

- We do not find a clear correlation between neither of the physical parameters studied (radial distance to the galactic center, or SFR, H I,H_2, H I+H_2 surface densities) with the H I or CO line widths.

- CO line widths are, on average, indistinguishable from H I line widths. The mean ratio of H I to CO velocity dispersion we measure is $\sigma_{HI}/\sigma_{CO} = 1.0 \pm 0.2$.

The first result implies that, on scales of 0.5 kpc, we cannot easily identify the main driver of turbulent motions inside neutral gas within galaxies. The second result can be regarded as an unexpected finding, because even though typical velocity dispersions within molecular clouds are of $\sim 2-8$ km s^{-1} (e.g., Solomon et al. 1987; Bolatto et al. 2008; Heyer et al. 2009), we measure CO velocity dispersions of ~ 12 km s^{-1}. These results are in agreement to what Combes & Becquaert (1997) measure when comparing H I and CO velocity dispersions in NGC 628 and NGC 3938. They suggest that both neutral and molecular gas constitute a single kinematic component. The interpretation we give to our results is that a diffuse molecular gas component, which gives rise to large velocity dispersions, might be common within normal spiral galaxies.

A way to test whether this interpretation is plausible, is by comparing single-dish and interferometric observations of molecular gas (as traced by CO). Pety et al. (2013) examined these two types of observations for M 51. They found that, not only velocity dispersions measured by single-dish instruments are twice as large as those measured from interferometric data, but also that the interferometer is able to recover only $\sim 50\%$ of the flux.

Following up on this idea, we compare line width measurements obtained with single-dish and interferometer telescopes in two galaxies: NGC 4736 and NGC 5055. The main result of this work is:

- For both galaxies we measure single-dish line widths that are $(40 \pm 20)\%$ larger than interferometric ones on spatial scales of ~ 0.5 kpc.

This result is in agreement with what Pety et al. (2013) found. We find evidence for a diffuse molecular gas component which gives rise to velocity dispersions that are larger to those measured within GMCs.

Finally, we continued our study on higher spatial scales by looking at M 31, the closest spiral galaxy to the Milky Way. By means of high spatial and spectral resolutions and high sensitivity data (for details, see Chapter 4), we are able to compare line widths measured for individual LOSs from interferometric and single-dish data. We also explore possible correlations between SFR tracers and CO emission at 85 pc $\times$ 380 pc scales. Complimentary to this, and by means of stacking, we are able to characterize the line profiles arising from measurements by these two kinds of instruments. The main results we obtain are:

- We do not find any correlation between SFR tracers (Hα, FUV, and 24, 70, and 160 μm) and CO line widths.

- For individual LOS measurements we find single-dish data line widths that are, on average, $\sim 50\%$ larger than the ones measured from interferometric data.

- The analysis on the stacked spectra shows that single-dish data are better described by two Gaussian components: a narrow component with a mean $\mathrm{FWHM_N} \sim 7.5 \pm 0.4\,\mathrm{km\ s^{-1}}$, and broad component with a $\mathrm{FWHM_B} \sim 14.4 \pm 1.5\,\mathrm{km\ s^{-1}}$; whereas one narrow component, with mean $\mathrm{FWHM} \sim 7.1 \pm 0.4\,\mathrm{km\ s^{-1}}$, suffices for the description of interferometric data.

These results reinforce the interpretation of molecular gas being conformed by two distinct components, one of which is filtered out by interferometric observations.

To understand the processes of the interstellar medium, we tend to classify different structures based on their physical properties. The results I present on this thesis warn against the possibility of over simplifying the structure of the neutral interstellar medium in galactic disks. The different phases that constitute it do not have sharp boundaries between them. Regarding neutral atomic gas, Heiles (2001) already noted that approximately half of it could be in an unstable phase between cold and warm neutral media. The results presented here suggest that a large fraction of molecular gas (up to $\sim 50\%$) might be in a diffuse phase that is filtered out by interferometric observations. Therefore, the neutral interstellar medium should be regarded as a single kinematic system, where material cycles between the atomic and molecular gas phases continuously. To reach a definite answer on the molecular gas configuration in galaxies, more observations, as well as more modeling of diffuse gas properties are needed.

5.2 Outlook

CO observations in nearby galaxies are typically planned so that molecular clouds can be detected. If we want to probe and quantify the existence of a diffuse molecular gas component robustly, observations should be designed accordingly. Mapping the molecular gas in nearby galaxies with interferometers is still expensive time-wise, and therefore, high quality data is limited. However, deep interferometric and single-dish observations are required in order to be able to study molecular gas in regions not dominated by emission from GMCs, namely, in regions dominated by diffuse gas. Interferometric observations could be carried out with PDBI or ALMA, as both instruments include short spacing observations to recover emission from extended structures. By combining these two sets of measurements, a thorough characterization of flux recovery fractions can be carried out robustly.

By taking single-dish observations and by using different configurations of the interferometer, we could estimate the fraction of molecular gas present in the diffuse component, and moreover,

derive how the width of the CO lines changes as a function of resolution/uv-coverage. The aim should be to study face-on galaxies (like NGC 628 and NGC 3184), for which projection effects and beam smearing result negligible. These observations could also allow the comparison of velocity dispersions in different environments (nuclear region, arm, and inter-arm regions). If variations on the FWHMs measured at different scales or at different locations within a galaxy were found, we would gain information regarding the processes responsible for driving turbulent motions in the neutral interstellar medium.

As described in the Introduction, a dynamically hotter molecular gas component would give rise to a thicker molecular disk. Therefore, an alternative approach to probe the structure of molecular gas is to study edge-on galaxies. By measuring the scale height of molecular gas we could infer its physical characteristics (e.g., Garcia-Burillo et al. 1992).

ACKNOWLEDGEMENTS

It is true that these almost four years led to a completion of a PhD, but the whole experience cannot be summarized in the written work that has been presented here. These four years came together with a whirlpool of experiences, thoughts, feelings, that, even though not explicitly stated on the previous chapters, were present throughout the work I carried out.

This all started when Fabian Walter, my supervisor, offered me a position to study nearby galaxies. Thank you, Fabian, for giving me this opportunity, for supporting me in attending conferences and observing runs, for pushing for the publication of the papers that constitute this work, and for the good intentions. Thank you also for the suggestions to improve the abstract.

The second person I would sincerely like to thank is Andreas Schruba, without whom I would not have been able to succeed. Thank you for your support, patience, for following up the work I was carrying out and giving me ideas on how to improve the analysis, and for always finding time to read and comment on the paper drafts and thesis. Thank you for making me feel that California or Munich could be so close.

Along the way, I also met people that helped me put ideas together for the different projects. I would like especially thank Jérôme Pety, Adam Leroy, and Jürgen Ott.

Regarding the thesis, I would like to acknowledge my two referees, Henrik Beuther and Hans-Walter Rix. Thank you for having agreed on reading my thesis. I would like to extend the acknowledgements to Eva Grebel and Luca Amendola for having agreed on forming part of my examination committee.

I particularly want to thank the people that very kindly offered themselves to read over my Introduction: Roberto Decarli, Greg Stinson, Akin Yildrim, Arjen van der Wel. Also thanks a lot to Richard Hanson (Ricardito) for having translated my Abstract. I really appreciate it.

Last, but not least, I would like to thank the IMPRS program, and in particular Christian Fendt. He not only takes care of the administrative issues about this PhD program, but his door is also always open for students. He has a great disposition to listen to our problems and to try to find a solution together. Thank you for your good will, patience, and for caring.

On the personal side, now I would like to name the people that were there, next to me (even if they were thousands of kilometers away), along the way. Primero quiero agradecer a mi mamá y a mi papá. Yo sé que para ustedes también fue difícil, sin embargo siempre estuvieron ahí para darme su apoyo, confianza y cariño. Esta tesis va por ustedes, para los mejores papás que podría imaginar tener. También quiero agradecer a mis hermanos, Tania y José Luis. Uno de los momentos más lindos para mi en estos años, fue cuando nos reunimos los tres en Berlín. Tania y Churro, nunca imaginé que compartiríamos la experiencia de vivir en Alemania, es muy lindo tenerlos tan cerca. Finalmente, gracias a Isa, por las llamadas, con y sin mi llanto, y por tu visita. A todos los quiero mucho.

Thomas, thank you for always being there for me, and giving me support in the moments I needed it more. You were a source of strength and distraction. I cannot imagine having walked this path without you by my side.

One of the best things I take away from these years, is having met my other family, the Heidelberg family: Agnesina, Ivouschka, Marta, and Esteban (Estefani). No matter what happened, in the end we were always there for each other, I would not change that for anything. This also goes for the extended family. Fabrizio, thank you in particular for the pressure-release walks, and for listening. Regarding the last months, thank you again for sharing the half-marathon preparation, together with the thesis marathon.. we did it! Eduardo, I am glad there was somebody that could understand me (not only because of sharing the same language). Thank you for standing my (maybe repetitive) complaints. Frauita (Camilla), we started together, we finish together... thanks for the colorful hair-style ride. I cherish all the moments, mostly of happiness, but also sadness, frustration, anger, that we all shared. Los quiero.

I thank also my dear Italians, Camilla, Fabrizio, Salvo, and Daniele, which made lunch time an amazing experience. Thanks to the soccer players, another good pressure release activity. Especially thanks to Greg for being so enthusiastic and keeping on organizing it. Thank you Frank and Maria, for speaking German with me. Thanks Roberto for listening to me in the moments of pure frustration.

Thanks to la Chilanga Banda, Vero, Margara, Fryda, Nicole, Saúl, Steffen, Luisa, for the taco days and the beers at Hemingway's. I will include here also the bavarian chilango, Chucho, who inspired me with his emails about marathons and thesis writing.

I would also like to thank the IMPRS 7th generation. I am really happy for having been part of such a large generation, with people from all over the world. We had great moments together. I will especially dearly remember our retreats. Thanks in particular to Jan, I think we did a great team!

Gracias también a Henri y Clara, que desde el principio me abrieron las puertas de su casa y me brindaron su amistad. Poder compartir con ustedes el trayecto en el autobús, hizo que subir a trabajar se sintiera más liviano. Henri, vielen Dank auch für den Deutsch Unterricht.

Last, but not least, I want to thank all my friends that are far from Germany, but always made me feel we were close. In particular the moderns and associates: Adri, Marina, Luzma, Lucy, Cacho, Flippy, Danny, Baxter, Weri, Kurt, Jero, Chelius, Marifer, who made me laugh so much, even if they woke me up in the middle of the night with whatsapp messages. My dear ex-physicist friends Rebe, Xoch, Lizardo, Emiliana. The internationals: Marcelina, Mam, Caro, Jiri, Gusi, Daniel. Thanks to Lorenzo, for having visited me and invited me to visit him in Bonn.

Unfortunately, I cannot mention all the people that made of these four years an unforgettable experience. However, I will always remember all the magic moments I spent with all the amazing people that crossed my way in this adventure, and hope that life makes our ways come across again in the future.

Bibliography

André, P., et al. 2010, A&A, 518, L102

Avila-Reese, V., & Vázquez-Semadeni, E. 2001, ApJ, 553, 645

Ballesteros-Paredes, J., Hartmann, L., & Vázquez-Semadeni, E. 1999, ApJ, 527, 285

Bally, J., Langer, W. D., Stark, A. A., & Wilson, R. W. 1987, ApJ, 312, L45

Banerjee, A., Jog, C. J., Brinks, E., & Bagetakos, I. 2011, MNRAS, 415, 687

Bergin, E. A., & Tafalla, M. 2007, ARA&A, 45, 339

Bigiel, F., Leroy, A., Walter, F., Brinks, E., de Blok, W. J. G., Madore, B., & Thornley, M. D. 2008, AJ, 136, 2846

Blitz, L. 1993, in Protostars and Planets III, ed. E. H. Levy & J. I. Lunine, 125–161

Blitz, L., & Shu, F. H. 1980, ApJ, 238, 148

Blitz, L., & Williams, J. P. 1999, in NATO Advanced Science Institutes (ASI) Series C, Vol. 540, NATO Advanced Science Institutes (ASI) Series C, ed. C. J. Lada & N. D. Kylafis, 3

Bolatto, A. D., Leroy, A. K., Rosolowsky, E., Walter, F., & Blitz, L. 2008, ApJ, 686, 948

Bolatto, A. D., Wolfire, M., & Leroy, A. K. 2013, ARA&A, 51, 207

Braun, R., Thilker, D. A., Walterbos, R. A. M., & Corbelli, E. 2009, ApJ, 695, 937

Brunt, C. M., & Mac Low, M.-M. 2004, ApJ, 604, 196

Burgh, E. B., France, K., & Jenkins, E. B. 2010, ApJ, 708, 334

Burke, B. F., & Graham-Smith, F. 2014, An Introduction to Radio Astronomy

Caldú-Primo, A., Schruba, A., Walter, F., Leroy, A., Bolatto, A. D., & Vogel, S. 2015, AJ, 149, 76

Caldú-Primo, A., Schruba, A., Walter, F., Leroy, A., Sandstrom, K., de Blok, W. J. G., Ianja-

masimanana, R., & Mogotsi, K. M. 2013, AJ, 146, 150
Calzetti, D., et al. 2005, ApJ, 633, 871
—. 2007, ApJ, 666, 870
—. 2010, ApJ, 714, 1256
Colombo, D., et al. 2014, ApJ, 784, 3
Combes, F., & Becquaert, J.-F. 1997, A&A, 326, 554
Combes, F., et al. 2012, A&A, 539, A67
Cotten, D. L., & Magnani, L. 2013, arXiv: 1306.3972
Crosthwaite, L. P., & Turner, J. L. 2007, AJ, 134, 1827
Daddi, E., et al. 2010, ApJ, 714, L118
Dalcanton, J. J., et al. 2012, ApJS, 200, 18
Dame, T. M., Hartmann, D., & Thaddeus, P. 2001, ApJ, 547, 792
Dame, T. M., Koper, E., Israel, F. P., & Thaddeus, P. 1993, ApJ, 418, 730
Dame, T. M., & Thaddeus, P. 1994, ApJ, 436, L173
de Blok, W. J. G., Walter, F., Brinks, E., Trachternach, C., Oh, S.-H., & Kennicutt, Jr., R. C. 2008, AJ, 136, 2648
Downes, D., & Solomon, P. M. 1998, ApJ, 507, 615
Draine, B. T. 2003, ARA&A, 41, 241
—. 2011, Physics of the Interstellar and Intergalactic Medium
Elmegreen, B. G. 1989, ApJ, 338, 178
Elmegreen, B. G., & Scalo, J. 2004, ARA&A, 42, 211
Field, G. B., Goldsmith, D. W., & Habing, H. J. 1969, ApJ, 155, L149
Fritz, J., et al. 2012, A&A, 546, A34
Fukui, Y., et al. 2008, ApJS, 178, 56
Gao, Y., & Solomon, P. M. 2004, ApJ, 606, 271
Garcia-Burillo, S., Guelin, M., Cernicharo, J., & Dahlem, M. 1992, A&A, 266, 21
Genzel, R., et al. 2010, MNRAS, 407, 2091
Gil de Paz, A., et al. 2007, ApJS, 173, 185
Goldsmith, P. F., Heyer, M., Narayanan, G., Snell, R., Li, D., & Brunt, C. 2008, ApJ, 680, 428
Gordon, K. D., et al. 2006, ApJ, 638, L87
Hao, C.-N., Kennicutt, R. C., Johnson, B. D., Calzetti, D., Dale, D. A., & Moustakas, J. 2011, ApJ, 741, 124
Hartmann, L. 2003, ApJ, 585, 398
Heiles, C. 2001, ApJ, 551, L105
Heiles, C., & Troland, T. H. 2003, ApJ, 586, 1067

Helfer, T. T., Thornley, M. D., Regan, M. W., Wong, T., Sheth, K., Vogel, S. N., Blitz, L., & Bock, D. C.-J. 2003, ApJS, 145, 259

Helfer, T. T., Vogel, S. N., Lugten, J. B., & Teuben, P. J. 2002, PASP, 114, 350

Heyer, M., Krawczyk, C., Duval, J., & Jackson, J. M. 2009, ApJ, 699, 1092

Heyer, M. H., & Brunt, C. M. 2004, ApJ, 615, L45

Hughes, A., et al. 2013, ApJ, 779, 46

Juneau, S., Narayanan, D. T., Moustakas, J., Shirley, Y. L., Bussmann, R. S., Kennicutt, Jr., R. C., & Vanden Bout, P. A. 2009, ApJ, 707, 1217

Kalberla, P. M. W., & Kerp, J. 2009, ARA&A, 47, 27

Kennicutt, R. C., & Evans, N. J. 2012, ARA&A, 50, 531

Kennicutt, Jr., R. C. 1989, ApJ, 344, 685

—. 1998, ARA&A, 36, 189

Kennicutt, Jr., R. C., et al. 2003, PASP, 115, 928

—. 2007, ApJ, 671, 333

Kruegel, E. 2003, The physics of interstellar dust

Kruijssen, J. M. D., & Longmore, S. N. 2014, MNRAS, 439, 3239

Krumholz, M. R., Dekel, A., & McKee, C. F. 2012, ApJ, 745, 69

Kuno, N., Nakai, N., Handa, T., & Sofue, Y. 1995, PASJ, 47, 745

Kuno, N., et al. 2007, PASJ, 59, 117

La Vigne, M. A. 2010, PhD thesis, University of Maryland, http://hdl.handle.net/1903/10350

Lada, C. J., Forbrich, J., Lombardi, M., & Alves, J. F. 2012, ApJ, 745, 190

Lada, C. J., Lombardi, M., & Alves, J. F. 2010, ApJ, 724, 687

Larson, R. B. 1981, MNRAS, 194, 809

Leroy, A. K., Walter, F., Brinks, E., Bigiel, F., de Blok, W. J. G., Madore, B., & Thornley, M. D. 2008, AJ, 136, 2782

Leroy, A. K., et al. 2009, AJ, 137, 4670

—. 2011, ApJ, 737, 12

—. 2012, AJ, 144, 3

—. 2013, AJ, 146, 19

Liszt, H. S., & Lucas, R. 1998, A&A, 339, 561

Liszt, H. S., & Pety, J. 2012, A&A, 541, A58

Liszt, H. S., Pety, J., & Lucas, R. 2010, A&A, 518, A45

Low, F. J., et al. 1984, ApJ, 278, L19

Mac Low, M.-M., Klessen, R. S., Burkert, A., & Smith, M. D. 1998, Physical Review Letters, 80, 2754

Magnani, L., Blitz, L., & Mundy, L. 1985, ApJ, 295, 402

Magnani, L., Hartmann, D., & Speck, B. G. 1996, ApJS, 106, 447

Mangum, J. G., & Shirley, Y. L. 2015, ArXiv e-prints

Markwardt, C. B. 2009, in Astronomical Data Analysis Software and Systems XVIII, ed. E. D. Bohlender, P. Dowler, & D. Durand, Vol. 411, 251–254

Martin, C. L., & Kennicutt, Jr., R. C. 2001, ApJ, 555, 301

Massey, P., Olsen, K. A. G., Hodge, P. W., Strong, S. B., Jacoby, G. H., Schlingman, W., & Smith, R. C. 2006, AJ, 131, 2478

Masters, K. L. 2005, PhD thesis, Cornell University, New York, USA

McConnachie, A. W., Irwin, M. J., Ferguson, A. M. N., Ibata, R. A., Lewis, G. F., & Tanvir, N. 2005, MNRAS, 356, 979

McKee, C. F., & Ostriker, E. C. 2007, ARA&A, 45, 565

McMullin, J. P., Waters, B., Schiebel, D., Young, W., & Golap, K. 2007, in Astronomical Society of the Pacific Conference Series, Vol. 376, Astronomical Data Analysis Software and Systems XVI, ed. R. A. Shaw, F. Hill, & D. J. Bell, 127

Mihalas, D., & Binney, J. 1981, Galactic astronomy: Structure and kinematics /2nd edition/

Mizuno, N., Rubio, M., Mizuno, A., Yamaguchi, R., Onishi, T., & Fukui, Y. 2001, PASJ, 53, L45

Nakai, N., Kuno, N., Handa, T., & Sofue, Y. 1994, PASJ, 46, 527

Narayan, C. A., & Jog, C. J. 2002, A&A, 394, 89

Nieten, C., Neininger, N., Guélin, M., Ungerechts, H., Lucas, R., Berkhuijsen, E. M., Beck, R., & Wielebinski, R. 2006, A&A, 453, 459

O'Brien, J. C., Freeman, K. C., & van der Kruit, P. C. 2010, A&A, 515, A62

Olling, R. P. 1996, AJ, 112, 457

Petric, A. O., & Rupen, M. P. 2007, AJ, 134, 1952

Pety, J., et al. 2013, ApJ, 779, 43

Polk, K. S., Knapp, G. R., Stark, A. A., & Wilson, R. W. 1988, ApJ, 332, 432

Rachford, B. L., et al. 2002, ApJ, 577, 221

Reynolds, R. J. 1984, ApJ, 282, 191

Ribas, I., Jordi, C., Vilardell, F., Fitzpatrick, E. L., Hilditch, R. W., & Guinan, E. F. 2005, ApJ, 635, L37

Rieke, G. H., Alonso-Herrero, A., Weiner, B. J., Pérez-González, P. G., Blaylock, M., Donley, J. L., & Marcillac, D. 2009, ApJ, 692, 556

Rohlfs, K., ed. 1977, Lecture Notes in Physics, Berlin Springer Verlag, Vol. 69, Lectures on density wave theory

Rosolowsky, E. 2007, ApJ, 654, 240

Saintonge, A. 2007, AJ, 133, 2087

Salim, S., et al. 2007, ApJS, 173, 267

Sanders, D. B., Solomon, P. M., & Scoville, N. Z. 1984, ApJ, 276, 182

Sandstrom, K. M., et al. 2013, ApJ, 777, 5

Sault, R. J., Teuben, P. J., & Wright, M. C. H. 1995, in Astronomical Society of the Pacific Conference Series, Vol. 77, Astronomical Data Analysis Software and Systems IV, ed. R. A. Shaw, H. E. Payne, & J. J. E. Hayes, 433

Sawada, T., Hasegawa, T., Sugimoto, M., Koda, J., & Handa, T. 2012, ApJ, 752, 118

Schinnerer, E., et al. 2013, arXiv: 1304.1801

Schmidt, M. 1959, ApJ, 129, 243

Schruba, A., Leroy, A. K., Walter, F., Sandstrom, K., & Rosolowsky, E. 2010, ApJ, 722, 1699

Schruba, A., et al. 2011, AJ, 142, 37

Schuster, K. F., Kramer, C., Hitschfeld, M., Garcia-Burillo, S., & Mookerjea, B. 2007, A&A, 461, 143

Seab, C. G. 1987, in Astrophysics and Space Science Library, Vol. 134, Interstellar Processes, ed. D. J. Hollenbach & H. A. Thronson, Jr., 491–512

Sheffer, Y., Rogers, M., Federman, S. R., Abel, N. P., Gredel, R., Lambert, D. L., & Shaw, G. 2008, ApJ, 687, 1075

Sheth, K., Vogel, S. N., Wilson, C. D., & Dame, T. M. 2008, ApJ, 675, 330

Shetty, R., Kelly, B. C., Rahman, N., Bigiel, F., Bolatto, A. D., Clark, P. C., Klessen, R. S., & Konstandin, L. K. 2013, arXiv: 1306.2951

Shull, J. M., & Beckwith, S. 1982, ARA&A, 20, 163

Snow, T. P., & McCall, B. J. 2006, ARA&A, 44, 367

Solomon, P. M., Rivolo, A. R., Barrett, J., & Yahil, A. 1987, ApJ, 319, 730

Somerville, R. S., & Davé, R. 2014, ArXiv e-prints

Spitzer, L. 1978, Physical processes in the interstellar medium

Spitzer, Jr., L., Cochran, W. D., & Hirshfeld, A. 1974, ApJS, 28, 373

Steer, D. G., Dewdney, P. E., & Ito, M. R. 1984, A&A, 137, 159

Strong, A. W., & Mattox, J. R. 1996, A&A, 308, L21

Sunada, K., Yamaguchi, C., Nakai, N., Sorai, K., Okumura, S. K., & Ukita, N. 2000, in Society of Photo-Optical Instrumentation Engineers (SPIE) Conference Series, Vol. 4015, Radio Telescopes, ed. H. R. Butcher, 237–246

Tamburro, D., Rix, H.-W., Leroy, A. K., Mac Low, M.-M., Walter, F., Kennicutt, R. C., Brinks, E., & de Blok, W. J. G. 2009, AJ, 137, 4424

Thilker, D. A., et al. 2005, ApJ, 619, L67

Tielens, A. G. G. M. 2005, The Physics and Chemistry of the Interstellar Medium

Tielens, A. G. G. M., McKee, C. F., Seab, C. G., & Hollenbach, D. J. 1994, ApJ, 431, 321

Tonry, J. L., Dressler, A., Blakeslee, J. P., Ajhar, E. A., Fletcher, A. B., Luppino, G. A., Metzger, M. R., & Moore, C. B. 2001, ApJ, 546, 681

van Dishoeck, E. F., & Black, J. H. 1988, ApJ, 334, 771

von Weizsäcker, C. F. 1951, ApJ, 114, 165

Walter, F., Brinks, E., de Blok, W. J. G., Bigiel, F., Kennicutt, Jr., R. C., Thornley, M. D., & Leroy, A. 2008, AJ, 136, 2563

Walter, F., Weiss, A., & Scoville, N. 2002, ApJ, 580, L21

Warren, S. R., et al. 2012, ApJ, 757, 84

Watson, W. D. 1972, ApJ, 176, 103

Wilson, C. D., et al. 2011, MNRAS, 410, 1409

Wolfire, M. G., Hollenbach, D., McKee, C. F., Tielens, A. G. G. M., & Bakes, E. L. O. 1995, ApJ, 443, 152

Wolfire, M. G., McKee, C. F., Hollenbach, D., & Tielens, A. G. G. M. 2003, ApJ, 587, 278

Wong, T., & Blitz, L. 2002, ApJ, 569, 157

Wyder, T. K., et al. 2009, ApJ, 696, 1834

Young, J. S., & Scoville, N. Z. 1991, ARA&A, 29, 581

Zhang, Q., Fall, S. M., & Whitmore, B. C. 2001, ApJ, 561, 727

List of Figures

List of Tables